Low-column density gas clumps in the inner and outer halo of the Milky Way

Dissertation

zur

Erlangung des Doktorgrades (Dr. rer. nat.)

der

Mathematisch-Naturwissenschaftlichen Fakultät

der

Rheinischen Friedrich-Wilhelms-Universität Bonn

vorgelegt von

Nadya Ben Bekhti

aus

Neuss

March 23, 2009

"Two roads diverged in a forest,
and I – I took the one less traveled,
and that has made all the difference."

(Robert Lee Frost, "The Road Not Taken")

Contents

List of Figures

9

List of Tables

Abstract

More than 40 years ago the occurrence of several narrow absorption lines in QSO (quasi-stellar object) spectra was recognized for the first time (Bahcall 1966). Soon after their detection it became clear that the absorption lines are related to intervening gaseous structures in the intergalactic medium (IGM). In recent years, substantial instrumental progress has been made to measure circumgalactic gas structures around the Milky Way and other galaxies. Now it is obvious that the gas structures play a fundamental role in the formation and evolution of the Milky Way and other spiral galaxies.

The most promising local counterparts of intervening circumgalactic metal-absorbers seen in QSO absorption line data are the so-called low-, intermediate-, and high-velocity clouds (LVCs, IVCs, HVCs, Muller et al. 1963) in the halo of the Milky Way. They represent clouds of neutral atomic hydrogen seen in 21 cm emission at radial velocities inconsistent with a simple model of Galactic disk rotation.

While there are a large number of recent absorption studies on the nature of LVCs, IVCs, and HVCs and their role for the evolution of the Milky Way, relatively little effort has been made to investigate their connection to the distribution and nature of intervening metal-absorption systems seen in QSO spectra around other galaxies. In fact, almost all recent absorption studies of IVCs and HVCs were carried out in the FUV to study in detail metal abundances and ionisation conditions of halo clouds using the many available transitions of low and high ions in the ultraviolet regime (e.g., Richter et al. 2001). These studies were designed as follow-up absorption observations of known IVCs and HVCs, thus providing an 21 cm *emission-selected* data set. However, to statistically compare the absorption characteristics of the extraplanar Galactic halo structures with the properties of intervening metal-absorption systems towards QSOs we use an *absorption-selected* data set of IVCs and HVCs. Since in the UV band there is currently only a very limited number (< 50) of high-quality spectra available such a statistical comparison can be done best in the optical regime, where a large number of high-quality spectra of low- and high-redshift QSOs are available.

This work discusses low-column density extraplanar gaseous structures detected in optical Ca II and Na I absorption towards quasars. In total 177 lines of sight were observed, providing one of the largest samples today for analyses of IVC and HVC gas which is most likely located in the inner and outer halo of the Milky Way. The study allows us to directly compare the observed absorption column-density distribution of gas in the Milky Way halo with the overall column-density distribution of intervening absorbers towards

QSOs. Moreover, the analysis enables us to identify the neutral and ionised absorption structures at low gas column densities and small angular extent that remain unseen in the large 21 cm IVC and HVC all-sky surveys, but that possibly have a considerable absorption cross section (see Richter et al. 2005). We supplement our absorption-line data with new H I 21 cm observations to investigate the relation between intermediate- and high-velocity Ca II absorption features and halo 21 cm emission. We discuss the first results of our analysis of the physical and statistical properties of the detected absorption and emission features. Additionally, follow-up H I high-resolution synthesis observations of four of the absorbers are presented, unveiling low-column density small-scale structures embedded in the absorbers environment.

The large sample of detected clouds enables for the first time a systematic statistical analysis of the properties of the low-column density cloud population in the Galactic halo. With these observations we demonstrate that the Milky Way halo contains a large number of low-column density neutral gas structures that give rise to intermediate- and high-velocity Ca II and Na I absorption. In some cases, the Ca II and Na I absorption lines are associated with known intermediate- and high-velocity clouds, but in other cases the observed absorption has no 21 cm counterpart. The observed Ca II column density distribution is similar to the distribution found for intervening Mg II systems that trace the gaseous environment of other galaxies at low and high redshift. The follow-up observations with radio synthesis telescopes uncovers several cold and compact (sub-pc scale) clumps.

For the future, we want to answer the question whether these low-column density small-scale structures are common in the extraplanar environment of the Milky Way and how they influence the evolution of our Galaxy. Therefore, we are planing to obtain and analyse new H I 21 cm data with high sensitivity and high spectral resolution as well as optical and UV absorption line data. This will allow us to enlarge our current absorption-selected sample and to improve the statistical analysis of the distribution and physical parameters of the absorbers to place the gaseous environment of the Milky Way into a cosmological context.

Introduction

1.1 The intergalactic medium and its connection to galaxies

The regions between stars and galaxies are far from empty. About 90% of the baryonic matter in the universe at $z \gtrsim 3$ resides in form of a diffuse gas in the the intergalactic medium (IGM, baryonic matter between galaxies; see Prause et al. 2007, and references therein). In the local universe ($z \sim 0$) this fraction has decreased to about 30%. Because the difference could not be explained by gas used for star formation, this issue was initially called *the missing baryon problem*. Today, a widely accepted theory is, that the gas has been shock-heated by gravitational collapse to temperatures of $T \sim 10^5 \ldots 10^7$ K, forming the Warm-Hot Intergalactic Medium (WHIM, Valageas et al. 2002, see Section 1.1.1). Gas that is gravitationally bound between stars in single galaxies (Interstellar Medium, ISM) and between galaxies in clusters of galaxies (Intracluster Medium, ICM) only contains $\sim 10\%$ of the baryons each (Davé 2003; Bell et al. 2003).

The gas in the ISM, IGM, and ICM consists of a mixture of atoms (mostly ions), free electrons, dust grains, and molecules. It exists in different gas phases with different physical properties. Although the interstellar, intracluster, and intergalactic regions are more devoid of matter than any vacuum created on Earth they can be detected and studied as there is lot of it filling a large volume.

1.1.1 The diffuse intergalactic medium

According to the standard model of cosmology, structure formation proceeded hierarchically in a way that smaller structures formed first and merged into larger ones. The most accepted theory indicates that the structures observed today are consequences of small deviations (quantum fluctuations) from a perfect homogeneous universe. Dark matter (DM) accumulated in these density inhomogeneities which grew up to macroscopic scales during the phase of inflation. The potential wells of the DM clusters gravitationally attracted baryonic matter out of which galaxies were formed.

The IGM, which is structured but not uniformly distributed, follows the underlying dark matter distribution. Simulations of structure formation show that the IGM fragments into an interconnected network of filaments (Cen et al. 1994; Wadsley & Bond 1997; Zhang et al. 1995), the so-called cosmic web (Bond et al. 1996).

The gas in the IGM is mostly highly ionised by the UV background radiation of galaxies and quasi-stellar objects (QSOs). Only about 0.01% of the gas is in the neutral gas phase but this small fraction gives rise to the so-called Lyman-α forest, which is believed to be a finger print of the cosmic web.

The Lyman-α forest

Bahcall & Salpeter (1965) and Bahcall (1966) observed for the first time several narrow absorption lines at optical and ultraviolet wavelengths in the spectrum of a QSO. It soon became clear that the broad spectrum of ultraviolet light of QSOs would be mostly absorbed by neutral hydrogen gas in the Lyα line ($\lambda = 1215.67$ Å) along the line of sight between the QSO and the observer. This conglomeration of absorption lines is known as the Lyman-α forest (Weymann et al. 1981).

The absorption lines are redshifted to higher wavelengths (compared to their rest-wavelength) by $1 + z$, where z is the redshift of the absorbing system. Since all intervening system have smaller redshifts than the background QSO, the Lyman-α forest is always at wavelengths shorter (bluewards) than that of the QSO; see Figure 1.1. The number of absorption lines increases with higher redshift. In the spectra of QSOs at high redshifts additionally the Gunn-Peterson effect is observed. It is caused by diffuse neutral hydrogen which absorbs the continuum radiation from the quasar completely (bluewards of the QSO). This so-called Gunn-Peterson trough is only detected at redshifts of $z \geq 5 \ldots 6$ tracing the epoch of re-ionisation. Only in the early universe the diffuse intergalactic hydrogen was in its neutral state, while it became re-ionised by the first stars and galaxies. Hence, today this gas can not be observed in Lyα absorption. Interestingly, the results from the Wilkinson Microwave Anisotropy Probe (WMAP, Hinshaw et al. 2008) indicate that the epoch of re-ionisation took place much earlier at $z \sim 11$ (Dunkley et al. 2008).

The neutral H I column densities of the absorbers range from about $10^{12} \ldots 10^{22}$ cm^{-2} (Meiksin 2007). The higher H I column densities $> 10^{15}$ cm^{-2} are believed to trace Galactic discs, the neutral fraction of extended ionised galaxy halos, and protogalaxies. The bulk of the absorbing systems have H I column densities of $< 10^{15}$ cm^{-2} tracing the highly ionised intergalactic medium. This gas has very low particle densities of $n_H < 10^{-4}$ cm^{-3} and is, as mentioned before, mostly ionised by photons of the metagalactic UV background.

The Warm-Hot Intergalactic Medium (WHIM)

Part of the IGM at $z = 0$ is believed to be shock-heated and collisionally ionised. When gas of the IGM falls into the potential wells of cosmic filaments, the atoms heat up to temperatures of 10^5 to 10^7 K. These temperatures are high enough for the ionisation of hydrogen via collisions. The gas at these high temperatures is called the warm-hot intergalactic medium (WHIM). The fraction of the WHIM of the baryonic matter content at $z = 0$ is about 30% (Cen & Ostriker 1999; Davé et al. 2001). Observations of the WHIM are difficult due to the low particle densities of $n_H \sim 10^{-8} \ldots 10^{-4}$ cm^{-3}. To observe and study the WHIM, absorption features in the FUV and X-ray regime can be used. The best
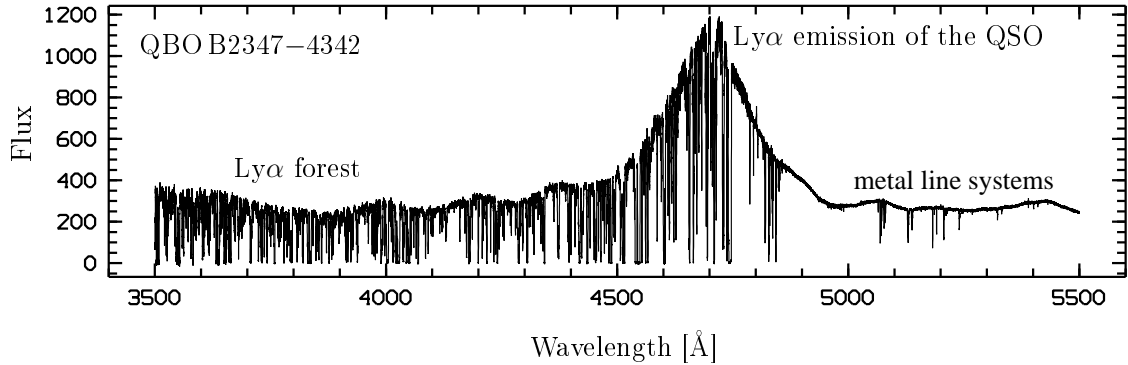
Fig. 1.1: Spectrum of QSO B2347−4342 (z_{em} = 2.9) observed with VLT/UVES. The Lyman α emission line of the QSO is clearly seen at about $\lambda_{Ly\alpha}(1 + z_{em}) \approx 4700$ Å. The conglomeration of absorption lines blueward of the emission line is the so-called Lyman α forest. Most of the metal lines are located in the redward part of the spectrum.

known tracer for the WHIM at $T \sim 3 \cdot 10^5$ K in the FUV regime is O VI (e.g., Richter et al. 2004; Sembach et al. 2004; Savage et al. 2005). X-ray observations are limited because of the low spectral resolution of current instruments. Using the O VI doublet ($\lambda = 1031.9$ and $\lambda = 1037.6$ Å), Sembach et al. (2003) studied the highly ionised high-velocity gas in the Milky Way halo in great detail. Their results indicate that about 60% of the sky is covered with ionised high-velocity gas.

1.1.2 The gaseous halos of galaxies

Spiral galaxies like our own are surrounded by large gaseous halos that represent the interface between the condensed galaxy discs and the surrounding intergalactic medium (e.g., Spitzer 1956; Savage & de Boer 1979; Savage & Massa 1987; Majewski 2004; Fraternali et al. 2007, and references therein). The properties of this extraplanar medium around a galaxy presumably are determined by both the accretion of metal-poor gaseous matter from intergalactic space and satellite galaxies onto the Galactic disc, as well as the outflow of metal-enriched gas caused by star formation activity within the galaxy (e.g., Shapiro & Field 1976; Bregman 1980; Savage & de Boer 1981; Sembach et al. 2003; Fraternali & Binney 2006, and references therein), e.g., by supernovae explosions.

Symbiosis of galaxies and their halos

There are many processes that influence the exchange of gaseous matter and energy between galaxies and the IGM. Galaxies and the surrounding IGM are in a permanent circular flow of matter exchange. In the hierarchical scenario, large galaxies like our own Milky Way are thought to form through merging with smaller galaxies and through the accretion of lower mass clouds and dark objects that lack stars. Metal-poor gas, remaining from the early formation phase, is falling into the potential of galaxies. In addition, interactions (tidal or ram-pressure) and merging with other galaxies accumulate the halo of

a galaxy with interstellar material. Gas from galaxies is re-injected into the surrounding IGM via supernova explosions, jets, and outflows of AGN. These matter injections enrich the IGM with heavy elements produced during nuclear fusion in stars. Supernovae as well as outflows produce density waves in their surrounding which can trigger fragmentation processes leading to star formation. All these feedback processes must have a significant impact on the evolution of the host galaxies.

Since the baryonic matter in the universe is dominated by gas which is the material out of which galaxies are formed and which is still in a feedback process with the galaxies, the IGM is a perfect laboratory for the analysis of galaxy formation and evolution from the early epochs of the universe until the present day.

1.2 Galactic intermediate- and high-velocity clouds

Our own Galaxy is surrounded by a population of neutral gas clouds with H I column densities of $N_{\rm HI} \geq 10^{19}\,{\rm cm}^{-2}$, as seen in 21 cm radio emission. These so-called intermediate- and high-velocity clouds (IVCs and HVCs) are clouds of neutral atomic hydrogen with radial velocities in the local standard of rest (LSR) frame, inconsistent with a simple model of Galactic rotation. They are believed to be extraplanar objects located in the halo (e.g., Complex A; van Woerden et al. 1999) and circumgalactic environment of the Milky Way (e.g. the Magellanic Stream, Mathewson et al. 1974).

1.2.1 Intermediate-velocity clouds (IVCs)

There is a lot of gas in the Galactic halo at intermediate velocities. First of all, there is no strict definition of what IVCs are. IVCs have velocities which are outside the range of what is in agreement with Galactic rotation. Different authors used different velocity ranges ($|v_{\rm LSR}|$ between 20 and $100\,{\rm km\,s}^{-2}$) to define intermediate velocity gas with respect to the LSR frame. This simple definition is not adequate, because in some directions (l and b), velocities of $|v_{\rm LSR}| \geq 20\,{\rm km\,s}^{-2}$ are expected from Galactic rotation. A solution for this problem was provided by Wakker (1991). He introduced the so-called deviation velocity, $v_{\rm DEV}$, that is the difference between the velocity of the clouds in the LSR frame and the extreme velocity ($v_{\rm min}$, $v_{\rm max}$) consistent with the Milky Way gas distributed along a specific line of sight:

$$v_{\rm DEV} = \left\{ \begin{array}{ll} v_{\rm LSR} - v_{\rm min} & \text{if } v_{\rm LSR} < 0 \\ v_{\rm LSR} - v_{\rm max} & \text{if } v_{\rm LSR} > 0 \end{array} \right. . \tag{1.1}$$

A cloud is defined as IVC, if $|v_{\rm DEV}| \leq 50\,{\rm km\,s}^{-1}$. If $|v_{\rm DEV}| > 50\,{\rm km\,s}^{-1}$, one speaks of high-velocity clouds.

Most IVCs are relatively nearby objects with typical distances of $< 2\,{\rm kpc}$ (Wakker 2001). The majority of these clouds show negative values of $v_{\rm LSR}$ indicating that most of them are falling towards the Galactic plane. Figure 1.2 shows a column density map of the IVC sky composed by Wakker (2004) based on the Leiden-Dwingeloo Survey (Hartmann & Burton 1997). The map shows that a large fraction of the intermediate velocity gas is arranged in large complexes (like IV-Spur and IV-Arch, etc.).

The origin of the IVCs is still unclear. There are some models trying to describe the physical properties and the origin of the gas clouds. Regarding the distribution and the
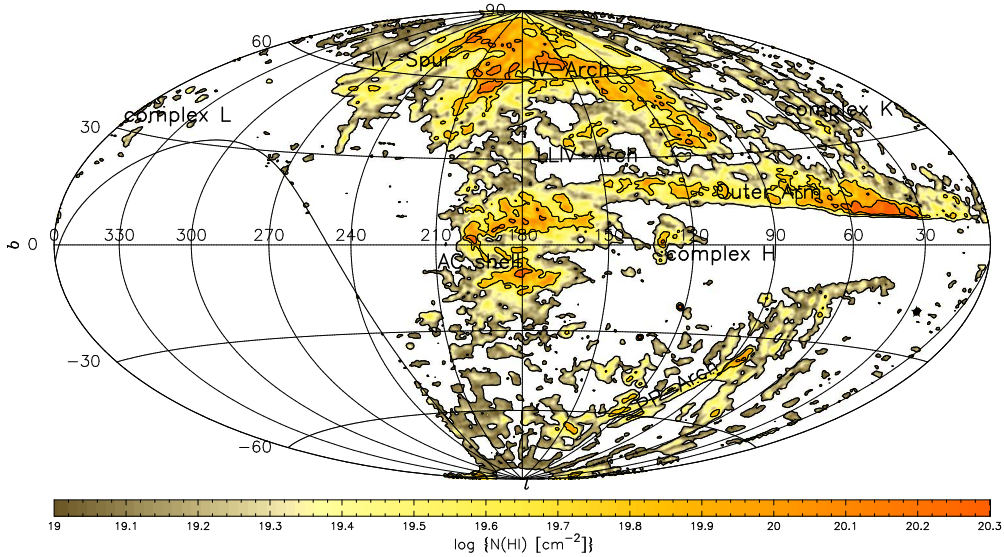
Fig. 1.2: Map of intermediate-velocity gas with v_{DEV} between -90 and $-35\,\mathrm{km\,s}^{-1}$ (Wakker 2004). The map is based on data from the Leiden-Dwingeloo Survey (Hartmann & Burton 1997). The contour levels show H I column densities of 10, 50, and $120 \cdot 10^{18}\,\mathrm{cm}^{-2}$.

velocities the most promising approach is that IVCs represent the outflows of supernovae explosions (Galactic Fountain model; Shapiro & Field 1976). In this scenario supernovae inject hot gas into the Galactic halo, where the gas is able to cool down and condense. It would then fall back onto the Galactic plane due to gravity.

Metallicity measurements of some IVCs, with the help of absorption line studies (e.g., Wakker 2001; Richter et al. 2001a), confirm the Galactic Fountain model. These IVCs have nearly solar abundances $(0.7 \ldots 1.0)$. This is an indication that the gas has already been processed in the nucleosynthesis cycle of Galactic stars.

1.2.2 High-velocity clouds (HVCs)

HVCs can be detected all over the sky, but they are not homogeneously distributed. Figure 1.3 shows an all-sky HVC map which was created by Westmeier (2007) based on the data of the LAB-survey (Kalberla et al. 2005a). Several extended, coherent HVC complexes cover the sky (e.g. complexes A, C, and M), some of which are spanning tens of degrees (like the Magellanic Stream). The numerous isolated and compact HVCs (angular sizes of $\phi \leq 2°$), the so-called compact high-velocity clouds (CHVCs), which are kinematically and spatially separated from the gas distribution in their environment (Braun & Burton 1999), are not visible due to the low-resolution of the plot.

The most critical problem of IVC and HVC research are the unknown distances to the clouds. There is no direct method to determine the distance from absorption and emission spectroscopy. Several indirect approaches exist, the most prominent of which uses suitable stars in front of and behind the cloud. Depending on its position the IVC and HVC gas would produce additional absorption lines in the stellar spectra providing a
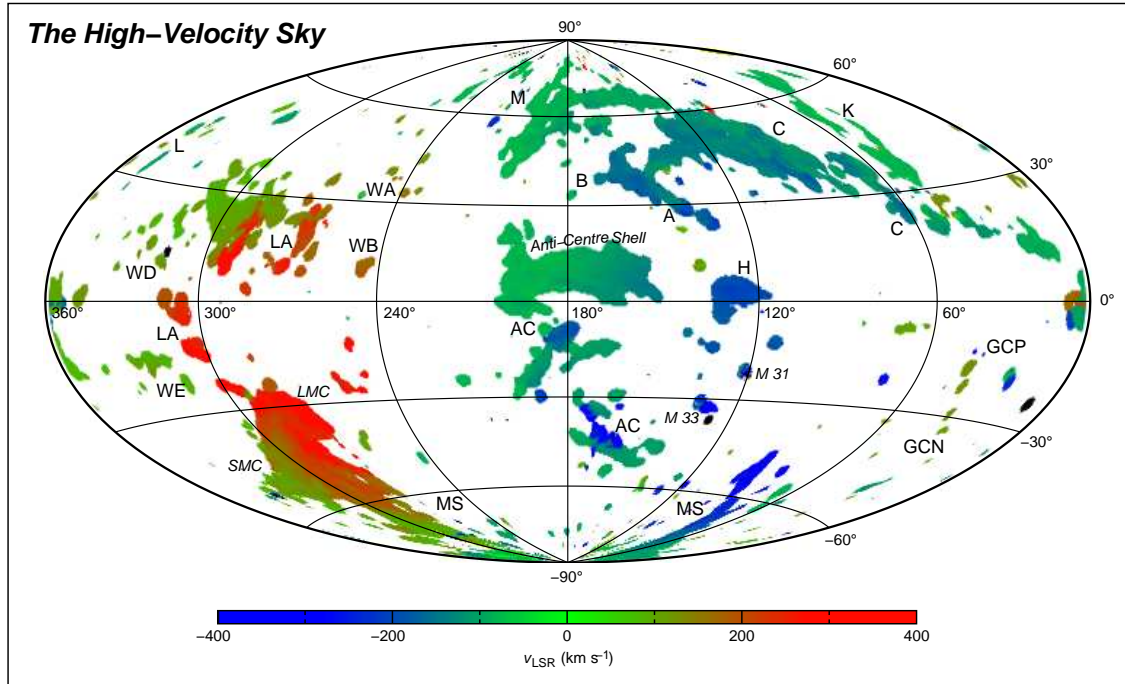
Fig. 1.3: HVC-all-sky map created by Westmeier (2007) derived from the data of the
Leiden-Argentine-Bonn (LAB) Survey (Kalberla et al. 2005a). Shown are the color-
coded velocities in the local standard of rest frame.

distance bracket (assuming that the distances to the stars are known). The problem is the
limited number of suitable background stars. The distance estimates of IVCs and HVCs
around the Milky Way (e.g., Sembach et al. 1991; van Woerden et al. 1999; Wakker 2001;
Thom et al. 2006; Wakker et al. 2007, 2008) indicate that most IVCs are relatively nearby
objects with distances of $d < 2\,$kpc while HVCs are more distant, located in the halo of
the Milky Way with distances of $5 < d < 50\,$kpc.

Due to the distance uncertainties, the spatial distribution of HVCs is largely unknown,
and important physical parameters, like mass ($M \sim d^2$), radius ($R \sim d$), and particle
density ($n \sim d^{-1}$) are poorly constrained.

Another important physical property of the IVCs and HVCs is their metallicity which
provides information about the origin of these clouds. The metal abundances of some IVCs
and HVCs have been determined by absorption line measurements along several lines of
sight (see Wakker 2001; Richter 2006). The results show that the metallicities are varying
between ~ 0.1 and ~ 1.0 solar (Figure 1.4). This wide range of metallicities suggests that
IVCs and HVCs do not have a common origin. The chemical composition of some IVCs
and HVCs with nearly solar metallicities can be explained by the Galactic fountain model.
There are, however, IVCs and HVCs with metal abundances below solar, but larger than
one would expect for primordial gas. The Magellanic Stream, for example, has abundances
similar to that of the Small Magellanic Cloud (~ 0.3 solar). There are also HVCs with
abundances less than ~ 0.3 solar (e.g., Complex C, Wakker et al. 1999) but still larger
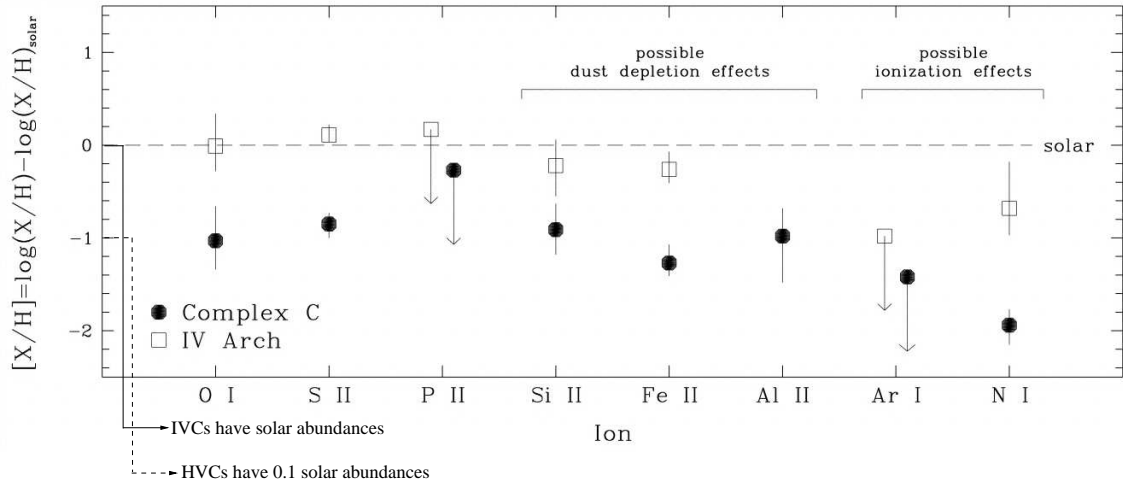
Fig. 1.4: Normalised interstellar gas-phase abundances in HVC complex C and the Intermediate-velocity Arch determined from absorption line studies (Richter et al. 2001b). The results show that the metallicities of IVCs and HVCs are varying between ~ 0.01 and ~ 1.0 solar.

than one would expect for primordial gas. The conclusion is that the high-velocity gas has already been processed, but at different levels and at different origins.

There are three main hypotheses for the origin of HVCs. The first is the formation from gas flowing out of the Galactic disc (Galactic Fountain model, Shapiro & Field 1976; Bregman 1980), the second is the origin from the interaction of dwarf galaxies with the Milky Way (Gardiner & Noguchi 1996; Bland-Hawthorn et al. 1998; Bregman 2004), and the third hypotheses is the primordial gas model, where HVCs are thought to be intergalactic gas which has not yet been accreted and metal enriched by one of the galaxies in the Local Group (Oort 1966; Blitz et al. 1999b).

Due to the possibility that HVCs do not have a single common origin, it is important to investigate the properties and physical parameters of HVCs. The best way to do this is to combine optical/UV absorption- and high-resolution H I 21 cm emission-line spectroscopy, which is an accurate method to analyse the gas-phase abundances and physical parameters of these clouds (see Chapter 1.4).

Obviously, IVCs and HVCs represent an important aspect in the hierarchical galaxy evolution model tracing on-going formation/evolution of the Milky Way.

1.3 Extraplanar gas around other galaxies

Early the question emerged, whether IVCs and HVCs are common phenomena around spiral galaxies. Nowadays the progress in instrumentation makes it possible to detect extraplanar gas in other nearby galaxies. There are various studies of extraplanar and circumgalactic H I structures around M31. Thilker et al. (2004) found several H I clouds in the halo of M31, all located within $\sim 200 \, \mathrm{km \, s^{-1}}$ of the systemic velocity of the host galaxy. Follow-up observations by Westmeier et al. (2005, 2007) with the WSRT and the 100-m telescope at Effelsberg confirmed the observations of the HVCs around M31. Their

M31 survey was optimised to trace the missing link between low-mass dwarf galaxies and gas clouds without star formation activity. Cosmological cold dark matter simulations (Klypin et al. 1999; Moore et al. 1999) predict hundreds of low-mass dark matter satellites around galaxies like the Milky Way as a consequence of the hierarchical structure formation scenario but only about 20 have been detected so far. Blitz et al. (1999a) suggested that some HVCs (e.g., the CHVCs) could be the gaseous counterparts of the missing dark matter halos.

Fig.1.5 shows the observed HVC population around M31 (Westmeier et al. 2005). The results of the data analysis reveal that neutral gas clouds could be detected only within 50 kpc from the stellar body of M31 (Westmeier et al. 2008). This result is in conflict with two major predictions. First, the prediction was made, that an extended population of CHVCs is located around M31 (Braun & Burton 1999; de Heij et al. 2002). Second, Klypin et al. (1999) predicted many more dark-matter halos at distances beyond 50 kpc from M31. As a consequence, HVCs can not account for all missing dark matter satellites.

The column densities of the HVCs detected around M31 ($N_{\mathrm{HI}} \sim 10^{19} \ldots 10^{20} \, \mathrm{cm}^{-2}$) are in agreement with the values derived for Galactic HVCs. Since M31, like the Milky Way, is surrounded by several satellite galaxies it might be that part of the observed HVCs are the results of tidal interactions.

Besides M31 there are observations of H I clouds in the halo of other galaxies like M51, M101 and NGC 891 (Oosterloo 2004; Peek et al. 2008). Recently, Chynoweth et al. (2008) detected several H I clouds and filaments around M81 and M82 with the Green Bank Telescope (GBT). So, it seems that HVCs are a common phenomenon around galaxies.

1.4   Absorption line studies of quasars and QSOs

One method to study the circumgalactic gas of galaxies is to trace the gas in absorption against extragalactic background sources. These can be quasi-stellar radio sources (quasars) and quasi-stellar objects (QSOs). Quasars were discovered with radio radiation, while QSOs have an optical emission-line spectrum. Both objects turned out, after original discovery and further study, to be galaxies with an active central region. They are thought to be powered by supermassive black holes at their centers. As the light of these objects travels a long distance to Earth the intervening matter will leave its imprint on the spectra (Schmidt 1963) in the form of hydrogen-, helium- or metal-line absorption; see sketch in Fig. 1.6.

1.4.1   QSO spectra

The spectra of QSOs show among strong emission lines a large number of absorption features. On the one hand these absorption lines could be caused by the QSO itself or by the host galaxy. On the other hand they could be produced by material along the line of sight between the QSO and us. The intervening intergalactic medium is full of diffuse hydrogen causing a uniform absorption of the QSO continuum over a broad range of wavelengths (Gunn & Peterson 1965) or discrete clouds producing separate absorption lines (for a recent review see Richter 2006).

QSO absorption spectroscopy has become a powerful method to study the physical properties, the kinematics, and the spatial distribution of gas in the halos of galaxies over
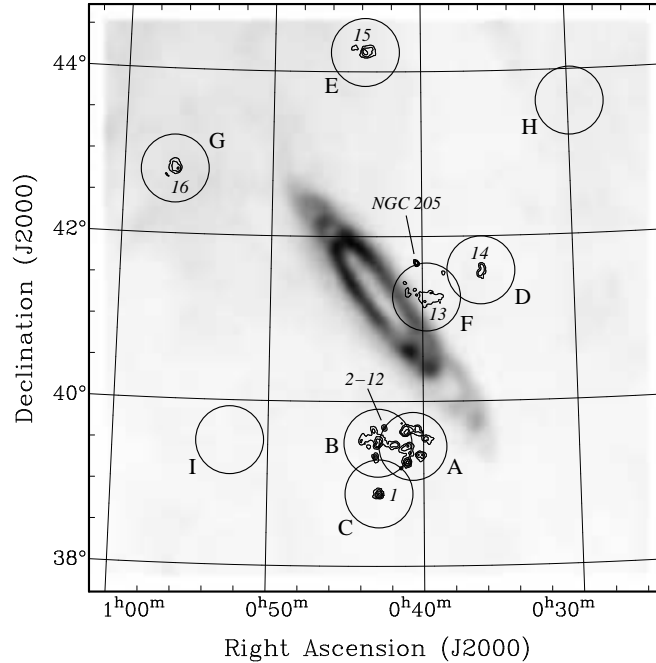
Fig. 1.5: HVCs observed around M 31 with the WSRT (Westmeier et al. 2005). The grayscale image shows the H I emission of M 31 observed by Thilker et al. (2004) with the GBT. The circles mark the nine fields observed with the WSRT centered on the brightest clouds. The contours show the H I data of 16 high-velocity clouds and of NGC 205. In fields H and I no reliable signal of high-velocity H I emission was found at the resolution and sensitivity of the WSRT data.

a large range of column densities at low and high redshifts. Absorption spectroscopy has the advantages that it is very sensitive to low column densities (which are undetectable in emission) and that it is independent of the distance to the absorbing objects as long as the background continuum source is bright enough. Note, that in this work, where we compare optical absorption spectra with H I emission spectra obtained with radio telescopes, the angular resolution of the absorption data is much better due to the intrinsically smaller beam size of optical telescopes. The analysis of the element composition of the gas gives us insight into the chemical evolution of galaxies. The study of intervening Mg II and C IV absorption line systems (e.g., Charlton et al. 2000; Ding et al. 2003a; Masiero et al. 2005; Bouché et al. 2006) and their relation to Galactic structures suggest rather complex absorption characteristics of these ions indicating the multi-phase nature of gas in the outskirts of galaxies with density and temperature ranges spanning several orders of magnitude. Stronger intervening low-ion absorbers (e.g., strong Mg II systems) preferentially arise at low impact parameters ($< 35\,h^{-1}\,$kpc, with the Hubble constant $H_0 = h \cdot 100\,\mathrm{km\,s^{-1}\,Mpc^{-1}}$) of intervening galaxies, while weaker Mg II systems and high-ion absorbers (e.g., C IV systems) apparently are often located at larger distances from up to $\sim 100h^{-1}\,$kpc (Churchill et al. 1999; Milutinović et al. 2006). Due to the lack of additional information the exact nature and origin of the various circumgalactic absorber
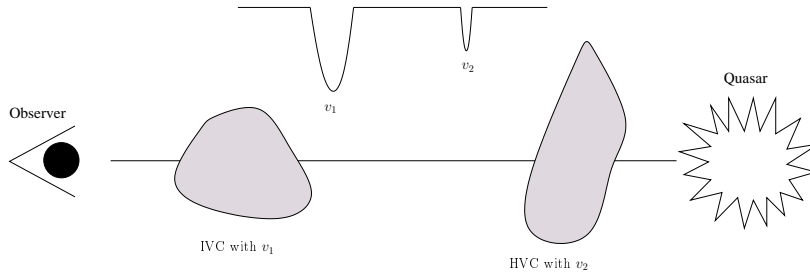
Fig. 1.6: Intervening intergalactic and interstellar matter (like IVCs or HVCs) will leave its imprint on the spectra of distant QSOs in the form of hydrogen- and metal-line absorption.

populations is not yet fully understood. Most likely, gas outflow and infall processes both contribute to the complex absorption pattern observed.

Because of the large number of absorption lines it is difficult to assign an absorption line in the spectra to a specific transition of a certain element at any redshift. For that reason, doublet lines like Ca II ($\lambda_0 \approx 3935\,\text{Å}$ and $\lambda_0 \approx 3970\,\text{Å}$), Na I ($\lambda_0 \approx 5892\,\text{Å}$ and $\lambda_0 \approx 5898\,\text{Å}$), Mg II ($\lambda_0 \approx 2795\,\text{Å}$ and $\lambda_0 \approx 2802\,\text{Å}$), and C IV ($\lambda_0 \approx 1549\,\text{Å}$ and $\lambda_0 \approx 1551\,\text{Å}$), which exist in a part of the spectrum with only a few absorption lines, are very useful.

Since parts of incoming radiation are absorbed by the Earth's atmosphere, the ground-based QSO absorption line analysis is limited to the optical, near infrared (IR), and radio regime. The VLT/UVES instrument (Dekker et al. 2000) used for our study, for example, covers a spectral range from $3000 - 11000\,\text{Å}$. If one wants to study QSO absorption lines in other wavelength regimes the only way is to utilise space-based observations with spectrographs like the Space Telescope Imaging Spectrograph (STIS, Woodgate et al. 1998) on the Hubble Space Telescope or the Far Ultraviolet Spectroscopic Explorer (FUSE, Moos et al. 1998).

1.4.2 Classification of QSO absorption line systems

The absorption lines observed in QSO spectra result from the fact that before reaching the Earth the light of the QSO passes through vast stretches of the intergalactic space containing gaseous structures. The individual spectral lines are caused by bound-bound transitions of the atoms by emitting or absorbing photons with discrete energies.

Since the universe is expanding and the hydrogen clumps are located at different positions between the Earth and the QSO each individual gas cloud leaves its fingerprint in form of an absorption line at a different position in the spectra of QSOs depending on the distance/redshift and the peculiar (radial) velocity of the source.

One classifies the different QSO absorption line systems according to their wavelengths, line widths, shapes and strengths.

Name	H I column density [cm^{-2}]
Lyman-α forest	$< 10^{15}$
Metal-line systems	$> 10^{15}$
Lyman-limit systems	$10^{17} - 10^{19}$
Damped Lyman-α systems	$> 10^{19}$

Table 1.1: Summary of QSO absorption line systems and their characteristic H I column densities.

Properties of the Lyman-α forest

In the spectra of distant QSOs one observes the bulk of weak absorption lines at wavelengths shorter (blueward) than that of the QSOs Lyman-α peak; these lines constitute the so-called Lyman-α forest (Section 1.1.1).

The analysis of the Lyman-α forest provides information about the frequency of occurrence and the physical parameters of the hydrogen clouds. In particular, the strengths of the individual absorption lines of the forest is an indicator for the density of the neutral hydrogen structures along the sight line. The analysis of the Lyman-α forest shows that the hydrogen in the universe is not homogeneously distributed but organized into a complex filamentary structure with hydrogen densities varying by factor of 1000 to 1000000.

QSO absorption line systems are subdivided into four subclasses depending on H I column densities, redshift, strength and metal content. There are several narrow and weak lines (small line width) produced by gas with H I column densities of $N_{\mathrm{HI}} \leq 10^{15}\,\mathrm{cm}^{-2}$, the Lyman α forest. Hydrogen gas clouds with $10^{17}\mathrm{cm}^{-2} < N_{\mathrm{HI}} < 10^{19}\,\mathrm{cm}^{-2}$ produce the so-called Lyman limit systems (LLS). These systems absorb the entire radiation of the QSO below a wavelength of $\lambda \leq 912\,\text{Å}$ (restframe of the absorber). If the column density of the absorbing gas is $N_{\mathrm{HI}} \geq 10^{19}\,\mathrm{cm}^{-2}$ the absorption lines will show typical damping wings around the lines and one speaks of damped Lyman-α systems (DLA).

Metal systems

QSO absorption-line systems with typical H I column densities of $\geq 10^{15}\,\mathrm{cm}^{-2}$ that have associated metal lines are called metal absorption line systems (MLS). They are produced by metals along the lines of sight between the observer and a QSO. Generally, weakly ionised metals show rather narrow absorption lines. These small line widths make the metal absorption systems perfect candidates for a precise measurement of physical properties of the absorbing gas like column densities and temperatures. Most of the prominent metal lines (Mg II, Ca II, C IV, etc.) appear in the ultraviolet, optical and near-infrared regime.

If the observed absorption systems and the QSO have similar redshifts one speaks of associated metal absorption lines. These systems are associated with the QSO itself, and the absorption could possibly be caused by the host-galaxy.

For a better overview, a summary of the absorption line systems and their characteristic H I column densities is given in Table 1.1. Figure 1.7 displays a H I column density
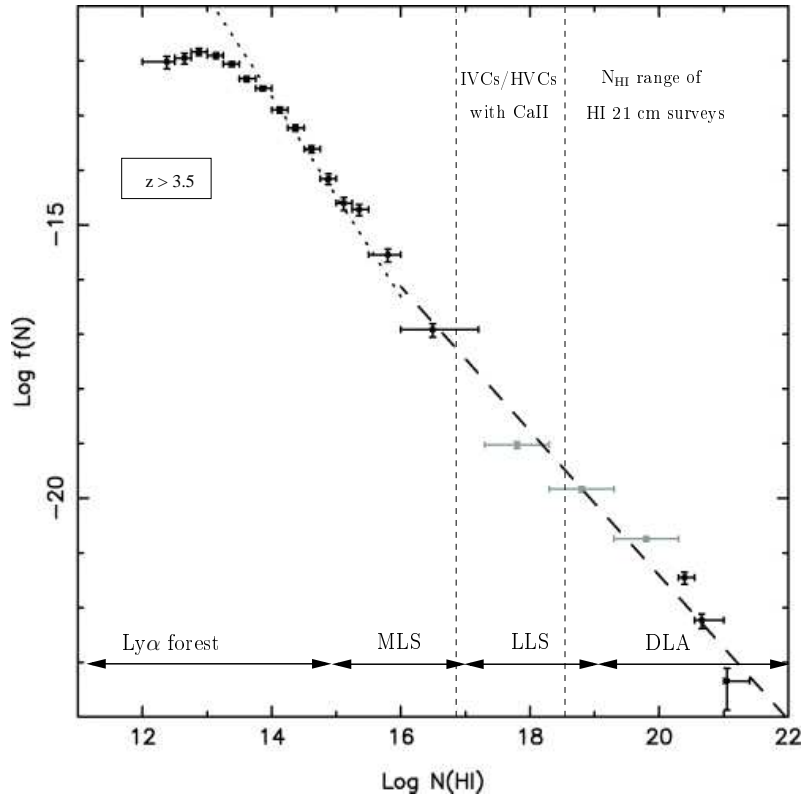
Fig. 1.7: Column density distribution (CDD) function of QSO absorption line systems
at $z > 3.5$ generated by Richter (2005). Plotted is the logarithm of the H I col-
umn density distribution function, $f(N)$, (see Section 6.1.1) versus the logarithm of
H I column densities. Additionally, shown are the approximate H I column density
regimes for the different QSO absorption line systems.

distribution function, $f(N)$, of QSO absorption line systems at $z > 3.5$ computed by Pe-
titjean et al. (1993), which is the number of absorbers as a function of column density (see
Section 6.1.1). Additionally shown are the approximate H I column density regimes for the
Lyman-α forest and the metal, Lyman limit and damped Lyman α systems. The vertical
dashed lines mark the sensitivity ranges of IVC and HVC observations using optical (Ca II)
absorption spectroscopy and current H I 21 cm surveys. For convenience the Ca II column
densities have been converted to N_{HI} ranges; compare Section 6.1.1. Most of the observed
Ca II and Na I absorption components (and therefore the converted H I column densities)
are close to or below the detection limit of the H I 21 cm surveys.

1.5   21 cm observations of extraplanar gas

Another powerful method to learn something about the extraplanar gas of galaxies is
to study emission lines in the 21 cm regime. 21 cm emission line spectroscopy has the
advantage of high velocity resolution, whereas only nearby (typically $z = 0.06$ for large H I

surveys like "The Arecibo Legacy Fast ALFA Survey" (ALFALFA) and the "Effelsberg-Bonn HI Survey" (EBHIS) (Winkel et al. 2008)) sources can be observed.

A huge amount of neutral hydrogen gas, with velocities incompatible with the Galactic rotation, is located in the halo of the Milky Way (e.g., Wakker 1991; Wakker & van Woerden 1997; van Woerden et al. 1999; Lockman et al. 2002). The large IVC and HVC complexes have masses up to $10^6 \ldots 10^7 \, \mathrm{M_\odot}$ (an exception is the Magellanic system with $3 \cdot 10^8 \, \mathrm{M_\odot}$; for further details see Wakker 2004). However, little attention has been paid so far to the low column density gas with $N_{\mathrm{HI}} < 10^{19} \, \mathrm{cm^{-2}}$ because the large H I surveys have detection limits of a few times $N_{\mathrm{HI}} \sim 10^{18} \, \mathrm{cm^{-2}}$ to $N_{\mathrm{HI}} \sim 10^{19} \, \mathrm{cm^{-2}}$. More sensitive observations with the GBT (Lockman et al. 2002) and the Arecibo telescope (Hoffman et al. 2004) revealed the presence of low column density high-velocity gas. Wakker (2004) detected H I emission with column densities down to $7 \cdot 10^{17} \, \mathrm{cm^{-2}}$ (median completeness limit), and it seems that there is no cutoff in the high-velocity population at low N_{HI}. They found that for a randomly chosen direction on the sky, the probability to find high-velocity gas with $N_{\mathrm{HI}} > 7 \cdot 10^{17} \, \mathrm{cm^{-2}}$ is about 30% and about 15% for $N_{\mathrm{HI}} > 2 \cdot 10^{18} \, \mathrm{cm^{-2}}$. Brüns & Westmeier (2004) and Hoffman et al. (2004) observed HVCs with diameters of $< 35'$, the so-called ultra-compact high-velocity clouds (or mini HVCs).

1.6 Motivation and outline of the thesis

While there are a large number of recent absorption line studies on the nature of IVCs and HVCs and their role for the evolution of the Milky Way, relatively little attention has been paid so far to the abundance and distribution of the low-column density neutral component of intermediate- and high-velocity gas in the Galactic halo below the detection limit of large H I surveys. Furthermore, little effort has been made to investigate the connection between the Galactic population of IVCs and HVCs and the distribution and nature of intervening metal-absorption systems from galaxy halos seen in QSO spectra. In fact, almost all recent absorption studies of IVCs and HVCs were carried out in the FUV to study in detail metal abundances and ionisation conditions of halo clouds using the many available transitions of low and high ions in the ultraviolet regime. These studies were designed as follow-up absorption observations of known IVCs and HVCs, thus providing a 21 cm *emission-selected* data set. However, to statistically compare the absorption characteristics of Galactic halo structures with the properties of intervening metal-absorption systems towards QSOs one requires an *absorption-selected* data set of IVCs and HVCs.

In this thesis I concentrate on the study of low-column density, circumgalactic metal-line absorption systems in the halo of our own galaxy and link them to the distribution of neutral gaseous structures in the Milky Way as seen in H I 21 cm emission.

I discuss low-column density extraplanar structures, which are most likely located in the inner and outer halo of the Milky Way, as detected in optical Ca II and Na I absorption towards QSOs along 177 sight lines through the Milky Way halo. This study allows us to directly compare the observed absorption column-density distribution of gas in the Milky Way halo with the column-density distribution of intervening absorbers toward QSOs. Moreover, the study enables us to identify neutral and ionised absorption structures at low gas column densities and small angular extent that remain unseen in the large 21 cm IVC

and HVC all-sky surveys, but that possibly have a considerable absorption cross section. I supplement our absorption-line data with new H I 21 cm observations to investigate the relation between intermediate- and high-velocity Ca II absorption features and halo 21 cm emission. Additionally, I present follow-up H I synthesis observations of some of the absorbers to analyse the small-scale structure within the observed gas clouds. The analysis of small-scale structures is an important step on the way to learn more about the connection between the different gas phases in the halo of the Milky Way. We want to compare characteristics, distribution, metallicity, and origin of the intermediate- and high-velocity gas with absorption line systems in the circumgalactic environment of other galaxies and their gaseous halos, as observed by Charlton et al. (2000), Ding et al. (2003a) and Bouché et al. (2006).

Chapter 2 gives an overview about the physics of absorption and emission lines. Chapter 3 provides a detailed introduction into the principles and methods of radio interferometry. The different instruments used for the work, as well as the obtained datasets and their reduction are presented in Chapter 4. The basic results from the optical, single-dish and high-resolution data are presented in Chapter 5. Chapter 6 presents the statistical analysis of the absorber sample and discusses their physical properties and possible origins. The analysis and the discussion of the follow-up observations of four different sight lines with radio synthesis telescopes are presented in Chapter 7. Chapter 8 contains the conclusions and the outlook.

Physics of absorption and emission lines

In this chapter a brief overview will be given about the fundamental physics which can be used to derive important physical parameters from observations. These quantities are necessary for the analysis and the understanding of the gaseous structures in the galactic halo.

2.1 Radiative transfer

The radiative transfer equation describes the propagation of light, emitted from a source, on its way through a medium to an observer. Photons can be absorbed, (re-)emitted, or scattered by atoms and ions.

The total change of the intensity $I = \int_0^\infty I_\nu \mathrm{d}\nu$ over a certain distance $\mathrm{d}s$ due to emission and absorption is given by the radiative transfer equation

$$\frac{\mathrm{d}I_\nu}{\mathrm{d}s} = -\kappa_\nu I_\nu + j_\nu \tag{2.1}$$

with I_ν the intensity of the emitting source, κ_ν the absorption and j_ν the emission coefficient (which are related to the Einstein coefficients). The emission coefficient j_ν is defined as the energy E emitted by matter per unit volume $\mathrm{d}V$ per unit time $\mathrm{d}t$ per unit frequency $\mathrm{d}\nu$ into a unit solid angle $\mathrm{d}\Omega$

$$\mathrm{d}E = j_\nu \mathrm{d}V \mathrm{d}\Omega \mathrm{d}t \mathrm{d}\nu \,. \tag{2.2}$$

By travelling the distance $\mathrm{d}s$, a beam of photons with cross section $\mathrm{d}A$ travels through a volume $\mathrm{d}V = A\mathrm{d}s$. The intensity added to the beam by (spontaneous) emission is therefore

$$\mathrm{d}I_\nu = j_\nu \mathrm{d}s \,. \tag{2.3}$$

Similarly, the absorption coefficient κ_ν is given by the intensity loss in a beam of photons traveling over the path length $\mathrm{d}s$. The quantum-mechanical probability of absorption is proportional to the intensity of the emitting source, therefore one gets

$$\mathrm{d}I_\nu = -\kappa_\nu I_\nu \mathrm{d}s \,. \tag{2.4}$$

2.1.1 Optical depth

The optical depth is a measure for the opacity of a medium and is defined as

$$\tau_\nu = \int_0^{s_0} \kappa_\nu \mathrm{d}s\,. \tag{2.5}$$

Inserting Eq. (2.5) into Eq. (2.4) and integrating over the path length leads to

$$I_\nu = I_\nu^0 e^{-\tau_\nu}\,. \tag{2.6}$$

A medium is called optically thick when the change of τ_ν across the medium is $\Delta\tau_\nu > 1$. In that case, a photon of a given frequency is, on average, not able to traverse the medium without being absorbed. If $\Delta\tau_\nu < 1$ one speaks of an optically thin medium and a photon is generally able to cross the entire medium without being absorbed.

2.2 Optical and ultraviolet absorption line analysis

As mentioned in the previous chapter, intervening material along the line of sight between the QSO and the absorber produces absorption features in the spectra of QSOs. Since the most distant QSOs are at $z \approx 6$, they emitted the radiation that we observe at a very early state of the universe. Therefore, the analysis of these absorption lines provides important information about the evolution of gaseous structures in the IGM over a large redshift range ($z \approx 0 \ldots 6$).

2.2.1 Spectral lines

A spectral line is characterised by three main properties, central wavelength, strength, and shape. There are three types of absorption/emission spectra: individual (sharp) lines, series of lines called bands, and spectral continuum extending over a broad frequency regime.

Spectral lines are the result of the interaction between atoms or molecules and photons. When a photon has the energy according to the energy difference between two electronic states, electrons are able to change their orbitals by absorbing the photons. The probability that an electron in a bound level will make a transition to a higher or lower level is described by the Einstein transition probability. For a two-level system (upper level u and lower level l), the rate of an upward stimulated transition (absorption) is

$$-\frac{\mathrm{d}n_l}{\mathrm{d}t} = n_l B_{lu} I_\nu \tag{2.7}$$

where n_l is the number density of atoms in the lower state, I_ν is the light intensity, and B_{lu} is the Einstein coefficient for absorption.

Due to the limited lifetime of an excited state, the transition energy does not need to be infinitesimally sharp, but has a frequency dependence, which is described by the normalised Lorentzian function

$$L(\nu) = \frac{1}{\pi} \frac{\gamma/2}{(2\pi\Delta\nu)^2 + (\gamma/2)^2} \tag{2.8}$$

where γ is the damping constant and $\Delta\nu = \nu - \nu_0$ with ν_0 being the transition frequency. The damping constant γ is quantummechanically interpreted as the reciprocal of the mean life time of the upper state and is the full width at half maximum of the line profile.

One can write an expression for the absorption coefficient κ_ν as a function of frequency

$$\kappa_\nu = \frac{\pi e^2}{mc} n_l f_{lu} F(\nu) \qquad (2.9)$$

with f_{lu} as the oscillator strength, m the mass of the particle, c the speed of light, and e the elementary charge. The oscillator strength compares the absorption or emission rate of a transition with those of an ideal, classical, single electron, harmonic oscillator. It is a dimensionless number which is proportional to the Einstein constant for absorption B_{lu}

$$f_{lu} = \frac{mc\lambda^2}{\pi e^2 8\pi} \cdot \frac{g_l}{g_u} B_{lu} \qquad (2.10)$$

where g_l and g_u are the statistical weights of the lower and upper states, respectively.

2.2.2 Line profiles

Lorentzian-profile

The natural broadening is a consequence of the Heisenberg energy-time uncertainty principle. The excited levels of atoms have a finite lifetime and therefore slightly different energies. Hence, the transition frequency is not sharp. As a consequence, an observed absorption line is described by a Lorentzian profile (Eq. (2.8)).

Gaussian-profile

In an ideal gas, the thermal velocities of gas atoms are described by the Maxwellian velocity distribution $f(v)$

$$f(v) = 4\pi n(v) \left(\frac{m}{2\pi k_B T}\right)^{3/2} v^2 \exp\left(\frac{-mv^2}{2k_B T}\right) \qquad (2.11)$$

where $n(v)$ is the number of particles with velocity v, k_B is the Boltzmann constant, T the gas temperature and m the mass of a particle. Each of the atoms has an individual motion suspect to the Doppler shift, which means that the emitted photons will be redshifted or blueshifted depending on the velocity of the atom relative to the observer. The higher the temperature of the gas, the broader the spectral line emitted from that gas will be. This broadening effect is described by a Doppler-profile which is a Gauss function (in an ideal gas)

$$D(\nu) = \frac{1}{\sqrt{\pi}\Delta\nu_D} \cdot \exp\left[-\left(\frac{\Delta\nu}{\Delta\nu_D}\right)^2\right] \qquad (2.12)$$

with $\Delta\nu_D = \left(\frac{\nu_0}{c}\right) \cdot b_{th}$ the most probable deviation from the rest frequency ν_0 and b_{th} the thermal part of the Doppler-parameter b which is

$$b_{th} = \sqrt{\frac{2k_B T}{m}} = 0.129 \cdot \sqrt{\frac{T}{A}} \, \text{km s}^{-1} \qquad (2.13)$$

where A is the atomic weight.

As mentioned before b_{th} is only the thermal part of the Doppler-parameter. There is also a contribution due to turbulence, hence

$$b = \sqrt{b_{\text{th}}^2 + b_{\text{turb}}^2} \,. \tag{2.14}$$

One has to distinguish between macroscopic and microscopic motions in a gas. When the scale of a turbulence is much smaller than the mean free path of a photon one speaks of microscopic turbulences, otherwise of macroscopic turbulences.

Voigt-profile

An observed spectral line is determined by the combination of all the processes described above. The finally measured spectral profile is the convolution of the Lorentz profile (Eq. (2.8)) and the Doppler profile (Eq. (2.12))

$$F(\nu) = L(\nu) \otimes D(\nu) = \int_{-\infty}^{\infty} L(\nu - x) D(x) \mathrm{d}x = \frac{1}{\sqrt{\pi} 2\pi \Delta\nu_{\text{D}}} \cdot H(\alpha, y) \tag{2.15}$$

with $H(\alpha, y)$, the Voigt function

$$H(\alpha, y) = \frac{\alpha}{\pi} \int_{-\infty}^{\infty} \frac{e^{-x^2}}{(y - x)^2 + \alpha^2} \mathrm{d}x \,. \tag{2.16}$$

It is

$$\alpha = \frac{\gamma}{4\pi \Delta\nu_D} \tag{2.17}$$

and

$$y = \frac{\nu - \nu_0}{\Delta\nu_D} \,. \tag{2.18}$$

The parameter α compares the relative strength of Doppler broadening ($\Delta\nu_{\text{D}}$) and the natural linewidth (damping constant γ). If α is small, the line shape is approximated by a Doppler profile. Large α means strong damping and the Voigt profile shows damping wings.

2.2.3   Equivalent width and curve-of-growth (COG)

A common quantity for the description of the line strength is the so-called equivalent width W_λ. It is the width of a rectangle with the same area (measured between the level of the continuum and reference zero) as covered by the absorption line profile,

$$W_\lambda = \int_0^{\infty} \frac{|I_0 - I_\lambda|}{I_0} \mathrm{d}\lambda \tag{2.19}$$

with I_0 the continuum intensity and I_λ the intensity at a given wavelength. If we consider only absorption, the radiative transfer equation is described by Eq. (2.6). We get

$$W_\lambda = \int_0^{\infty} [1 - \exp(-\tau_\lambda)] \, \mathrm{d}\lambda \,. \tag{2.20}$$

Due to

$$\frac{W_\lambda}{\lambda} = \frac{W_\nu}{\nu} \tag{2.21}$$

the equivalent width can be written as a function of wavelength or frequency. Using Eq. (2.5), (2.9), and (2.20) one gets

$$W_\nu = \int_0^\infty \left[1 - \exp\left(-\int_{s_1}^{s_2} \kappa_\nu ds \right) \right] d\nu \tag{2.22}$$

$$= \int_0^\infty \left[1 - \exp\left(-\int_0^{s_0} \frac{\pi e^2}{mc} n_l(s) f_{lu} F(\nu) ds \right) \right] d\nu \tag{2.23}$$

$$= \int_0^\infty \left[1 - \exp\left(-\int_0^{s_0} \frac{\pi e^2}{mc} n_l(s) f_{lu} \frac{1}{\sqrt{\pi} 2\pi \Delta\nu_D} H(\alpha, y) ds \right) \right] d\nu . \tag{2.24}$$

One can distinguish between three different cases depending on the optical depth τ.

- $\tau \ll 1$ and $\alpha \ll 1$
  Using $\tau \ll 1$, Eq. (2.22) reduces to

$$W_\nu = \int_0^\infty \tau_\nu d\nu = \int_0^\infty \int_0^{s_0} \frac{\pi e^2}{mc} n_l(s) f_{lu} F(\nu) ds\, d\nu . \tag{2.25}$$

  Assuming that the gas is homogeneous along the line of sight, one can separate

$$W_\nu = \frac{\pi e^2}{mc} \int_0^{s_0} n_l f_{lu} ds \int_0^\infty F(\nu) d\nu . \tag{2.26}$$

  With $\alpha \ll 1$ (Eq. (2.17)), the absorption profile has the shape of a Gaussian (see Section 2.2). Hence, the integral $\int_0^\infty F(\nu)\, d\nu = 1$. The quantity $\int_0^{s_0} n_l ds = N_l$ is called the column density. If we finally express the equivalent width as a function of the wavelength we get

$$\frac{W_\lambda}{\lambda} = \frac{\pi e^2}{mc} N_l f_{lu} \lambda . \tag{2.27}$$

  For small optical depth the equivalent width is linearly proportional to the column density, N_l, along the line of sight with the length s (irrespectively of the b-value).

- $\tau \sim 1$ and $\alpha \sim 1$
  For a higher abundance of atoms, the line of sight becomes optically thick and saturates. Saturation means that the line intensity at the center is small. The equivalent width of the line increases moderately by only growing the wings (broadening of the line and the Doppler broadening dominates the increase of the line strength). In that case, Eq. (2.24) cannot be solved analytically. Numerically, one gets

$$\frac{W_\lambda}{\lambda} \sim \log N_l f_{lu} \lambda . \tag{2.28}$$

- $\tau \gg 1$ and $\alpha \gg 1$
  In this regime the damping is dominant over the Doppler broadening. Therefore, the shape of the spectral line shows Lorentzian damping wings. The equivalent width is given by

$$\frac{W_\lambda}{\lambda} = \sqrt{\frac{\gamma e^2 \lambda}{mc^3}} \cdot \sqrt{N_l f_{lu} \lambda} . \tag{2.29}$$
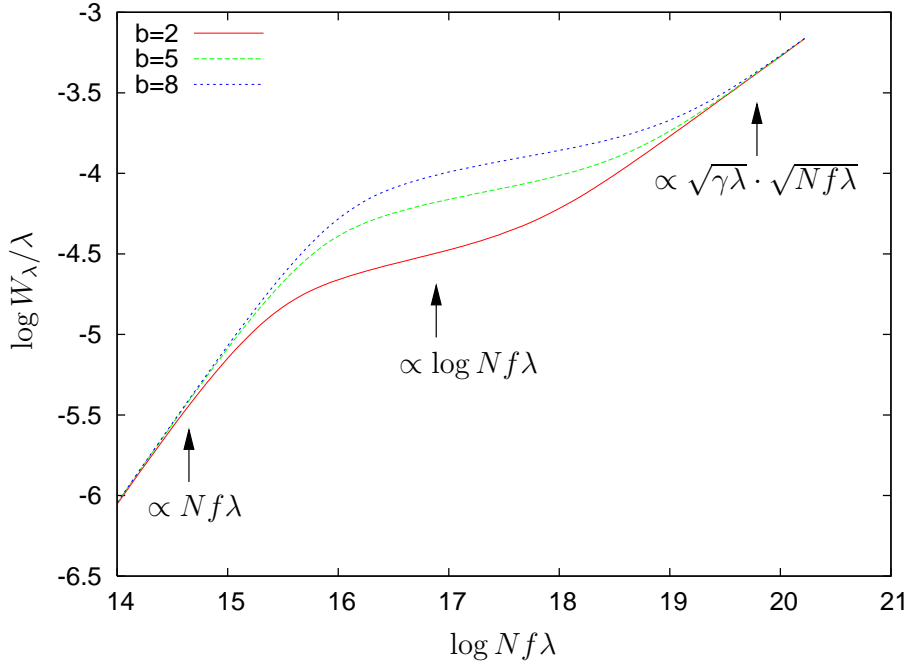
Fig. 2.1: The curve-of-growth, which describes how the line strength increases with
column density, for different values of the Doppler parameter b (in $\mathrm{km\,s^{-1}}$).

The equivalent width as a continuous function of the column density is called the curve-of-growth (COG). Figure 2.1 shows the COG for certain values of the oscillator strength f and the column density N in a double-logarithmic plot for different values of the Doppler parameter b. The three regimes discussed are marked in the figure.

By performing a curve-of-growth analysis, one can determine the column density N. One has to measure the equivalent width of a spectral absorption line by integrating over the intensity. In the case of weak or mildly saturated lines, Gaussian functions can be fitted to the spectral line. If the line is strongly saturated this approach is no longer valid because the dampening wings can not be neglected. The higher the optical depth the more intensity is lost in the center of the line and the stronger will be absorption in the wings.

In many interstellar absorbers the b value is not known. Then one has to determine W_λ for a sample of different absorption lines of the same element and ionisation level and thus with the same column densities (ideally with a large range of f values). After that, the b value can be determined by performing a curve of growth analysis.

2.3   H I spectral line analysis

In this section, the most important parameters which can be determined by the spectral analysis of H I lines are described.

2.3.1 Brightness temperature

An important measure in radio astronomy is the so-called brightness temperature T_{B}. T_{B} is the temperature that a blackbody would have to radiate the observed intensity of an object at a frequency ν. The brightness temperature can be calculated from the observed flux density, S_ν, in the way

$$T_{\mathrm{B}}(\nu)\,[\mathrm{K}] = S_\nu\,[\mathrm{Jy/Beam}]\frac{(\lambda_0\,[\mathrm{cm}])^2}{2.65\,\theta_{\mathrm{maj}}\theta_{\mathrm{min}}\,[']}\,, \qquad (2.30)$$

with $\theta_{\mathrm{maj,min}}$ the major and minor axis (FWHM) of the telescope beam for a given rest wavelength λ_0 of the transition. Note, that the brightness temperature is not the physical temperature of the object.

2.3.2 Upper temperature limit

The line width Δv follows directly from the observed spectral lines. In the 21 cm wavelength regime the observed line width is governed by the Doppler effect. With Eq. (2.11) one can derive an expression for the upper temperature limit (see Appendix A.1), because a higher temperature would result in a broader line width

$$T_{\mathrm{max}} = \frac{m\Delta v_{\mathrm{FWHM}}^2}{8 k_{\mathrm{B}} \ln 2}; \quad \text{or} \quad T_{\mathrm{max}}\,[\mathrm{K}] \approx 21.8 \cdot (\Delta v_{\mathrm{FWHM}}\,[\mathrm{km/s}])^2\,. \qquad (2.31)$$

The thermal contribution will be even lower than T_{max} because the line width is additionally affected by other effects like turbulence.

2.3.3 H I column density

In the case of small optical depth ($\tau \ll 1$) the column density is proportional to the integral of the observed spectral line profile

$$N_{\mathrm{HI}}\,[\mathrm{cm}^{-2}] = 1.823 \cdot 10^{18} \int T_{\mathrm{B}}(v)\mathrm{d}v\,\left[\mathrm{K\,km\,s}^{-1}\right]\,. \qquad (2.32)$$

The assumption of having optical thin gas is valid for IVCs and HVCs with $N_{\mathrm{HI}} \lesssim 10^{20}\,\mathrm{cm}^{-2}$.

2.3.4 Estimation of physical parameters

The determination of some physical parameters from H I 21 cm observations, like the size D, the mass M_{HI}, the H I density n_{HI} and the thermal gas pressure P, is only possible if the distance of an object is known. The total H I mass as a function of distance d is given by

$$M_{\mathrm{HI}} = m_{\mathrm{H}} \int_{\mathrm{source}} d^2 N_{\mathrm{HI}}(\theta, \phi)\,\mathrm{d}\Omega\,. \qquad (2.33)$$

Having a digitized column density map, each pixel i contains the column density $N_{\mathrm{HI}}^{(i)}$. The area of each pixel of angular size α can be described by $d^2 \tan^2 \alpha$ (if the map is not too large, e.g., in local tangential projection). Then we simplify Eq. (2.33) to

$$M_{\mathrm{HI}} = m_{\mathrm{H}} d^2 \tan^2 \alpha \sum_i N_{\mathrm{HI}}^{(i)} \qquad (2.34)$$

with m_{H} being the mass of the hydrogen atom.

One can estimate the mean density of an individual cloud using its measured peak column density and assuming spherical symmetry. Then the spatial size is $D = d \tan \varphi$ with φ the angular size of the object. The volume within the cloud covered by the sight line can be estimated for the spherical case to $V = A\,D$. We get

$$n_{\mathrm{HI}} = \frac{\text{Number of particles}}{\text{Volume}} = \frac{N_{\mathrm{HI}}\,A}{A\,D} = \frac{N_{\mathrm{HI}}}{d \tan \varphi}\,. \tag{2.35}$$

With the upper limit for the kinetic temperature, the derived density, and assuming an ideal gas one gets an expression for the upper thermal pressure limit

$$\frac{P}{k_{\mathrm{B}}} \le n_{\mathrm{HI}} T_{\mathrm{max}}\,. \tag{2.36}$$

2.4   Metal abundances

In the very early universe (shortly after the Big Bang) the only elements that were produced at large abundances were hydrogen and helium. All heavier elements which are observable today are the products of element fusion in stars. In astronomy, all chemical elements heavier than helium are considered as metals.

The metal abundance or metallicity is a measure of the amount of metals compared to the amount of hydrogen in an object of study compared to that ratio for the sun. The abundance (metallicity) $\frac{X}{H}$ of an element X is defined by

$$\left[\frac{X}{H}\right] = \log\left(\frac{N(X)}{N(H)}\right) - \log\left(\frac{N(X)}{N(H)}\right)_{\odot} \tag{2.37}$$

with N being the column density.

Metallicity measurements of astronomical objects are important because they provide an indication of their chemical age. As mentioned before, all elements heavier than helium are produced in stars during their lifetime. They recycle these heavy elements by releasing them back into the interstellar and intergalactic medium. This processed material becomes mixed into clouds where the next generation of stars are born. So, each new generation of stars is enriched with the metals produced in previous generations. Therefore, one can draw conclusions about the star-formation history of a galaxy. Metallicity measurements are also useful for studying the structure of our Galaxy and the circumgalactic material. Different parts of our Galaxy have different metal contents so we can infer their relative age. By comparing the metallicities of circumgalactic gas with the solar metallicity one can determine at what degree/level the gas has already been processed.

2.5   Photoionisation

When photons encounter atoms and the photons have energies larger than the ionisation potential of the atoms, an electron may be "kicked" out and the atom is ionised:

$$\text{atom} + h\nu \rightarrow \text{atom}^{+} + e^{-} \tag{2.38}$$

with h the Planck constant and ν the frequency of the photon.

The opposite effect where an ion catches an electron in a collision and transforms back into a neutral atom is called recombination

$$e^- + \text{ion} \rightarrow \text{atom} + \text{energy}\,. \tag{2.39}$$
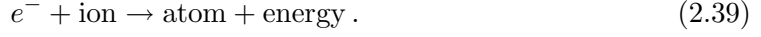
The ionisation balance is determined by the total ionisation rate, Γ_{total}, and the total recombination rate, $(\alpha(T) \cdot n_e)_{\text{total}}$,

$$\frac{n_{\text{ion}}}{n_{\text{atom}}} = \frac{\Gamma_{\text{total}}}{(\alpha(T) \cdot n_e)_{\text{total}}} \tag{2.40}$$

with

$$\Gamma_{\text{total}} = \Gamma_{\text{photo}} + \Gamma_{\text{coll.ionis.}} + \Gamma_{\text{chargeexch.}}\,, \tag{2.41}$$

and

$$(\alpha(T) \cdot n_e)_{\text{total}} = (\alpha_{\text{rad}} + \alpha_{\text{diel}}) \cdot n_e + \alpha_{\text{chargeexch}} \cdot n_x \tag{2.42}$$

where n_e is the electron density, n_x is the number density of the particular exchange particles, α_{rad}, α_{diel}, and $\alpha_{\text{chargeexch}}$ are the radiative, di-electronic, and charge exchange recombination rates (see de Boer 2006, for a complete overview). Table 2.1 shows the ionisation potentials, the transition wavelengths, and the theoretical photoionisation rates for the Milky Way disk of some of the important elements found in the ISM.

In case of IVCs and HVCs the density n_e is low and the temperatures are moderate. Therefore, Γ_{photo} and α_{rad} are the dominant terms (de Boer 2006). Using

$$\alpha_{\text{rad}} \simeq T_e^{-1/2} Z^2 \tag{2.43}$$

with the electron temperature, T_{e}, and the atomic number, Z, one gets an equation for the ionisation equilibrium

$$\frac{N_{\text{ion}}}{N_{\text{atom}}} = \frac{n_{\text{ion}}}{n_{\text{atom}}} = \frac{\Gamma_{\text{photo}} \sqrt{T_e}}{Z^2 \, n_{\text{e}}}\,, \tag{2.44}$$

with column densities N, assuming homogeneous density along the line of sight. This expression shows that ionised species are generally expected in warm, less dense regions, whereas the dense, cold regions they tend to be more in the neutral state. Hence, the observed b-values for neutral species are typically small.

Table 2.1: The ionisation potentials (IP), transitions, wavelengths, and photoionisation rates Γ_{photo} (theoretical, based on the mean interstellar radiation field of the Milky Way disk) for some elements observed in the ISM and IGM (de Boer et al. 1973; de Boer 2006, and references therein).

Atom	IP [eV]	Transition	Wavelength λ	Γ_{photo} $[10^{-12}s^{-1}]$
H I	13.6	$1s^2S \to 2p^2P$ (a)	1215.670 Å	
		$2s^2S \to 3p^2P$ (a)	6562.800 Å	
		$^2S_{1/2}$ (c)	1.42 GHz	
C I	11.256	$2p^2\ ^3P_0 \to 2p4d^3D_1$ (a)	1193.031 Å	120
		$2p^2\ ^3P_1 \to 2p4d^3D_2$ (a)	1193.009 Å	
		$2p^2\ ^3P_2 \to 2p4d^3D_3$ (a)	1193.240 Å	
C II		$2p^2P_{1/2} \to 2p^2\ ^2D_{3/2}$ (a)	1334.532 Å	
		$2p^2P_{3/2} \to 2p^2\ ^2D_{5/2}$ (a)	1335.708 Å	
C IV		$2p^2P_{1/2} \to 2s^2S_{3/2}$ (a)	1548.195 Å	
Na I	5.138	$3s^2S_{1/2} \to 3p^2P_{1/2}$ (a)	5895.924 Å	11
		$3s^2S_{1/2} \to 3p^2P_{3/2}$ (a)	5889.951 Å	
		$3s^2S_{1/2} \to 3p^2P_{3/2}$ (a)	3302.370 Å	
Mg I	7.644			37
Mg II		$3s^2S_{1/2} \to 3p^2P_{3/2}$ (a)	2795.528 Å	
Ca I	6.111			300
Ca II	11.868	$4s^2S_{1/2} \to 4p^2P_{1/2}$ (a)	3968.468 Å	1.3
		$4s^2S_{1/2} \to 4p^2P_{3/2}$ (a)	3933.663 Å	
O III		$2p^2\ ^3P_1 \to 2p^2\ ^1D_2$ (b)	4958.9 Å	
		$2p^2\ ^3D_2 \to 2p^2\ ^1D_2$ (b)	5006.9 Å	
		$2p^2\ ^1D_2 \to 2p^2\ ^1S_0$ (b)	4363.2 Å	

[a]Allowed transition, [b]Forbidden transition, [c]Hyperfine structure

Radio Interferometry

This chapter gives an overview about important aspects of radio interferometry, such as the functionality of high resolution radio synthesis telescopes and aperture synthesis.

3.1 Basic principles of radio interferometry

The angular resolution of a radio telescope is given by the half power beam width (HPBW)

$$\Theta_{\mathrm{HPBW}} \approx 1.22 \frac{\lambda}{D}\,, \tag{3.1}$$

with λ being the wavelength of the received radiation and D the diameter of the telescope dish. The HPBW is the smallest angular separation at which two sources are identifiable as separate objects. As seen in Eq. (3.1), one could improve the angular resolution by increasing the diameter of the telescope but there are of course limits (expenses and material). Even the largest radio telescopes (used at their shortest operating wavelength) have an angular resolution of only about one arcminute. Radio telescopes operate at much longer wavelengths than optical telescopes, therefore, radio telescopes must be much larger than optical telescopes to achieve a high angular resolution.

A solution for this problem is radio interferometry. Signals from multiple single dish telescopes are correlated to get higher angular resolutions. This correlation produces an interference pattern. Since the theory of radio interferometry is very complex, the two-element interferometer will first be discussed.

Figure 3.1 shows the antenna pattern of a single dish telescope and a two-element interferometer. The antenna pattern of the single dish telescope shows a main beam with a half power beam width given by Eq. (3.1) and adjacent side lobes. The antenna pattern of the ideal two-element interferometer (neglecting the antenna pattern of the individual telescopes) has no main beam and the side lobes do not decrease (Rohlfs & Wilson 1996). Practically, the synthesised antenna pattern has to be multiplied with the antenna pattern of the single dish telescopes, limiting the field-of-view of the instrument. Consequently, the sensitivity of the interference pattern decreases towards the rim.
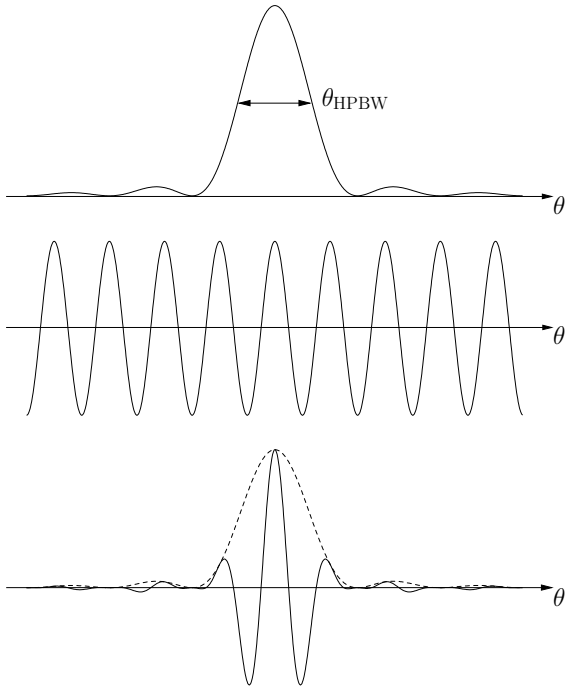
Fig. 3.1: **Top**: The antenna pattern of a single dish telescope. One can see the main beam with half power beam width of $\Theta_{\mathrm{HPBW}} \approx 1.22\lambda/D$ and adjacent side lobes. **Middle**: Pattern of a two-element interferometer, neglecting the antenna pattern of the individual telescopes. This pattern has no main beam and its side lobes do not decrease. **Bottom**: This pattern accounts for the fact that an interferometer consists of individual single dish telescopes each having its own (single dish) antenna pattern. Therefore, parts of the side lobes are suppressed.

As mentioned before, one can resolves point sources if their angular separation is larger than the HPBW of the telescope main beam. Compared to the effective angular resolution of an interferometer, single dish telescopes have larger HPBWs. Therefore they are only able to resolve extended sources but they are capable of measuring the total flux of the observed source (this will be discussed in Section 3.6). In contrast, an interferometer can resolve small-scale structures because of their high angular resolution. The disadvantage is that an interferometer is not able to measure the total flux of a diffuse, extended source. The reason for these properties will be discussed in Section 3.6.

The radiation, which is received through the side lobes, will be combined with the received radiation of the main beam. The image synthesis of an interferometer can be improved by minimisation of the side lobes. This can be achieved by independent measurements of the same object with different baselines.

3.2   Design of a two-element interferometer

Figure 3.2 shows the principle design of a two-element interferometer. Two single dish telescopes are located at a certain distance $\vec{B}$ from each other (baseline). Both telescopes point to the same direction in the sky. The arriving electromagnetic waves (for simplicity plane waves are assumed) are converted into an electric signal, which has to be amplified. Then it passes a mixer which down-converts the high frequency signal to an intermediate frequency. This is necessary because electronic devices work much better in the lower frequency regime. This process is called heterodyne principle (Klein 2006/2007). Finally, the signals pass additional amplifiers, a band pass filter, and a correlator (multiplication and integration of both signals).
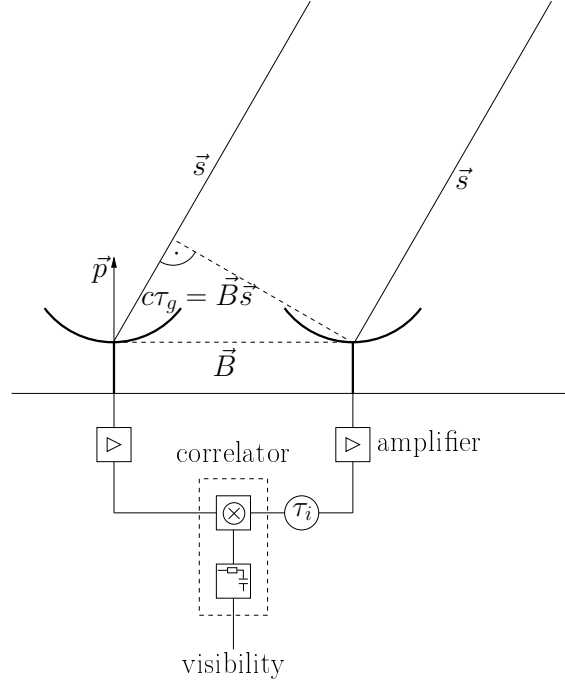
Fig. 3.2: Schematic view of the two-element interferometer.

At a given time the two telescopes measure different phases of the incoming radiation due to the different positions of the telescopes and instrumental effects. The geometric time delay τ_{g} is given by

$$\tau_{\mathrm{g}}c = \vec{B} \cdot \vec{s} \tag{3.2}$$

with c the speed of light, $\vec{B}$ the baseline vector and $\vec{s}$ the unit vector which is antiparallel to the direction of the waves arriving. One distinguishes between the geometrical delay τ_{g}, which is the time delay and phase shift due to the different telescope positions, and the instrumental delay τ_{i}, which is due to instrumental properties. Usually, τ_{i} is adjusted such that towards the reference point (direction of $\vec{s_0}$), which is the center of the observed map, the phase shift is zero (phase reference center). Figure 3.3 shows a possible source distribution. Both telescope main beams point in the direction $\vec{p}$ (in many cases one chooses $\vec{p} = \vec{s_0}$). Nevertheless, radiation reaches the telescopes from all directions. These resulting phase shifts contain the spatial information of the observed source. If we define a vector $\vec{\sigma}$ in the way

$$\vec{\sigma} = \vec{s} - \vec{s_0}\,, \tag{3.3}$$

it is clear that only sources which lie within the main beam of the telescope provide a significant fraction to the total intensity that is measured and correlated.

One has to consider that the measurements could be ambiguous. If $c\tau_{\mathrm{g}} = n\lambda_{\mathrm{radiation}}$ and n is an integer, no phase shift is observable. Therefore, it is crucial to know how much $\vec{B} \cdot \vec{s}$ has been shifted, i.e., determine n. This has to be done by measuring small baselines which means smaller τ_{g} and therefore $\tau_{\mathrm{g}}c < 1 \cdot \lambda$. Figure 3.4 shows the influence of both, the baseline and the angle of incident of the incoming radiation.
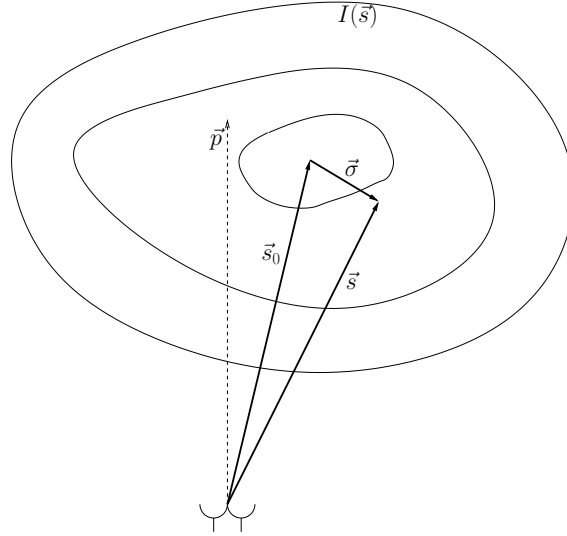
Fig. 3.3: A possible source distribution and geometry in interferometric measurements.
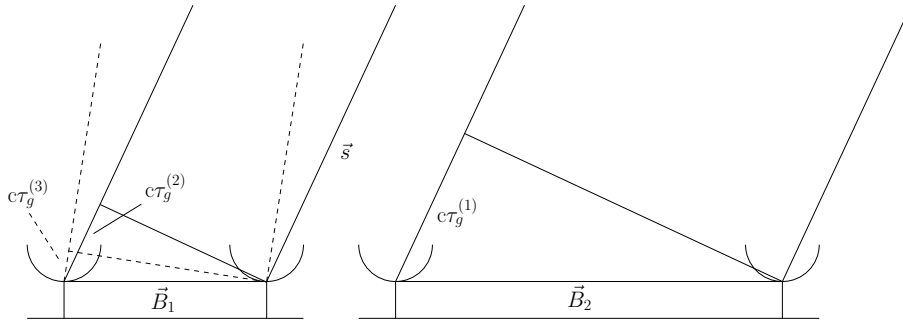
Fig. 3.4: Influence of different baselines and directions of incoming radiation on the geometrical delay. The larger the baseline the bigger is τ_gc. The steeper the incident angle of the incoming radiation the smaller is τ_gc.

3.3 Aperture Synthesis

If one assumes that an observed source has a brightness distribution $I_\nu(\vec{s})$, the power received per frequency range (bandwidth) $d\nu$ is given by

$$A(\vec{s})I_\nu(\vec{s}) \, d\Omega \, d\nu \tag{3.4}$$

with $A(\vec{s})$ the antenna pattern of the telescope and $d\Omega$ the solid angle (Rohlfs & Wilson 1996). The total response on the incoming radiation (from direction $\vec{s}$) of the correlator is obtained by integrating over the source. The result is the so-called correlation function

$$R(\vec{B}) = \iint_S A(\vec{s})I_\nu(\vec{s}) \exp\left[i\omega\left(\frac{1}{c}\vec{B}\vec{s} - \tau_i\right)\right] d\vec{s} d\nu. \tag{3.5}$$

with $\omega = 2\pi\nu$. The procedure of deriving the intensity distribution I_ν of the source from the measured correlation function $R(\vec{B})$ is called aperture synthesis. To solve Eq. (3.5) for

I_ν a coordinate system must be introduced in which the two vectors $\vec{B}$ and $\vec{s}$ are defined. With the introduced quantities $\vec{s_0}$ and $\vec{\sigma}$ Eq. (3.5) leads to

$$R(\vec{B})\mathrm{d}\nu = R_\nu(\vec{B}) = \exp\left[i\omega\left(\frac{1}{c}\vec{B}\vec{s_0} - \tau_\mathrm{i}\right)\right]d\nu\iint\limits_S A(\vec{\sigma})I(\vec{\sigma})\exp\left(i\frac{\omega}{c}\vec{B}\vec{\sigma}\right)\mathrm{d}\vec{\sigma}\,. \qquad (3.6)$$

The separated exponential factor extracted from the integral describes a plane wave which defines the phase of $R(\vec{B})$ in the image center (Rohlfs & Wilson 1996). $\vec{B}$, $\vec{s_0}$, and $\vec{\tau_\mathrm{i}}$ in the exponential term are known quantities which are chosen by the observer. The actual measure is the integral

$$V(\vec{B}) = \iint\limits_S A(\vec{\sigma})I(\vec{\sigma})\exp\left(i\frac{\omega}{c}\vec{B}\vec{\sigma}\right)\mathrm{d}\vec{\sigma}\,, \qquad (3.7)$$

which is called visibility. Since τ_i is adjusted to produce zero phase in the image center, the visibility is measured with respect to this reference point.

The visibility $V(\vec{B})$ and the resulting reconstructed intensity distribution I_ν are defined in different spaces. The visibility is measured in Fourier space which is described by the orthogonal coordinates (u, v, w). If one chooses a coordinate system such that

$$\frac{\omega}{2\pi c}\vec{B} = (u, v, w) \qquad (3.8)$$

where u, v, and w are measured in units of wavelength $\lambda = \frac{2\pi}{\omega}$, such that u points to an eastward and v to a northward direction while w is parallel to the direction of $\vec{s_0}$ (Figure 3.5). Accordingly, we introduce the notation $\vec{\sigma} = (x, y, z)$ such that x and y are the direction cosines with respect to the u and v axes. The x–y plane is therefore the projection of the celestial sphere onto a tangent plane with the tangent point $\vec{s_0}$. The z component is again parallel to $\vec{s_0}$ and hence, defined in the same way as w.

The phase information, which is measured in the Fourier space, is transformed into a spatial information by inverse Fourier transformation. In the coordinates (x, y, z), Eq. (3.7) converts to

$$V(u, v, w)\exp(-i2\pi w) = \int_{-\infty}^{\infty}\int_{-\infty}^{\infty} A(x, y)I(x, y)\exp\left[i2\pi(ux + vy)\right]\mathrm{d}x\mathrm{d}y\,. \qquad (3.9)$$

The phase factor $\exp(-i2\pi w)$ expresses the observed phase change of V relatively to what an array located in the u–v plane would measure, i.e., $V(u, v, w)\exp(-i2\pi w) \simeq V(u, v, 0)$. After applying the inverse Fourier transformation to Eq. (3.9) one gets

$$I'(x, y) = A(x, y)I(x, y) = \int_{-\infty}^{\infty} V(u, v, 0)\exp\left[-i2\pi(ux + vy)\right]\mathrm{d}u\mathrm{d}v \qquad (3.10)$$

with $I'(x, y)$ the intensity measured in position space, which has to be corrected for the antenna pattern (so-called primary-beam correction).
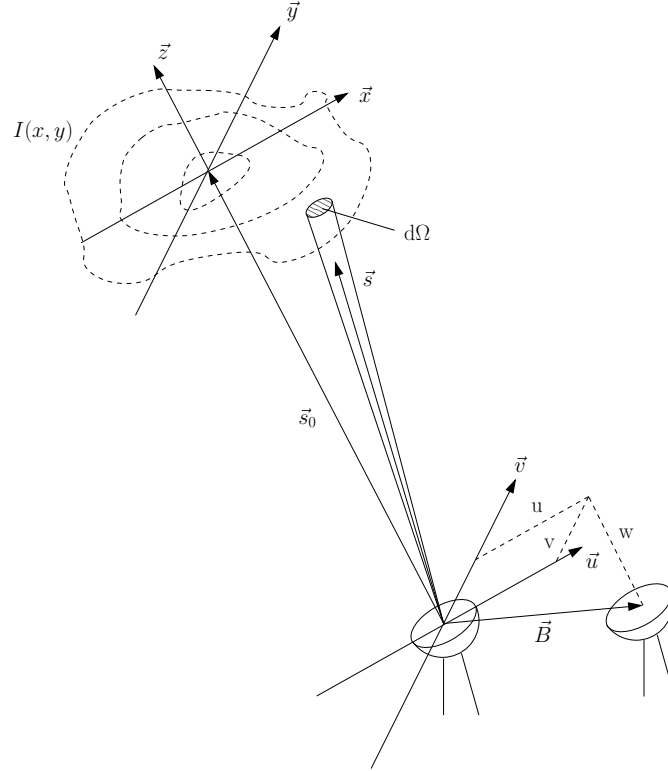
Fig. 3.5: Coordinate systems. The Fourier space is defined by the coordinates (u, v, w) and the position space is described by (x, y, z).

3.4   Dirty Beam and Dirty Image

As mentioned in Section 3.3 the visibility is the inverse Fourier transformation of the product of the intensity distribution I_ν and the antenna pattern A of an individual telescope

$$V_\nu^{\text{obs}} = \mathcal{F}^{-1}(I_\nu A) = \mathcal{F}^{-1}(I_\nu') \tag{3.11}$$

which is identical with (convolution theorem)

$$V_\nu^{\text{obs}} = \mathcal{F}^{-1}(I_\nu) \otimes \mathcal{F}^{-1}(A) . \tag{3.12}$$

In practice, the visibility is measured for discrete values of u and v only. The reconstructed map of the observed intensity distribution is called the dirty image/map $I_\nu^D(x, y)$ (this is the intensity which is measured by the observer). $I_\nu^D(x, y)$ is the inverse Fourier transformation of the product of the visibility $V_\nu(u, v)$ and the so-called sampling function $S_\nu(u, v)$ with

$$S_\nu(u, v) = \sum_{i=0}^{I-1} \sum_{j=0}^{J-1} \delta(u - i\Delta u)\delta(v - j\Delta v) . \tag{3.13}$$

Using again the convolution theorem leads to

$$
\begin{aligned}
I_\nu^D(x, y) &= \mathcal{F}^{-1}[V_\nu S_\nu](x, y) \\
&= \int_{-\infty}^{\infty} \int_{-\infty}^{\infty} V_\nu(u, v) S_\nu(u, v) \exp(2\pi i(ux + vy)) \mathrm{d}u \mathrm{d}v \\
&= \mathcal{F}^{-1}(V_\nu) \otimes \mathcal{F}^{-1}(S_\nu) \\
&= I_\nu' \otimes B_\nu^D
\end{aligned}
\tag{3.14}
$$

with B_ν^D the so-called dirty or synthesised beam, the response of the interferometer to a point source. In other words, B_ν^D is the antenna pattern as synthesised from a certain (u, v)-coverage.

One can combine $V_\nu S_\nu$ to the sampled visibility V_ν^s. Now it is easy to see that the Fourier transformation of V_ν^s is the convolution of the actual intensity distribution and the dirty beam. All points in the actual intensity distribution of the source are smeared with the dirty beam and this leads to the observed dirty image.

3.5 (u, v)-coverage

To allow an appropriate image reconstruction it is necessary to have good (u, v)-coverage, which means that one has to measure many different baselines. Special attention should be paid to the fact that it is impossible to measure the visibility for arbitrary values of (u, v). The visibility is defined in Fourier space. Every baseline corresponds to a certain frequency in Fourier space. Since there is a largest (finite array size) and a smallest (telescopes have a certain diameter) possible separation between the telescopes there is a corresponding smallest and largest frequency in spatial frequency space. To achieve a good (u, v)-coverage it is required to do measurements of a source with many different baselines. A possibility to get a satisfactory (u, v)-coverage is to use the Earth's rotation (Earth tracking, Józsa 2002). Then, a pair of single dish telescopes provides visibilities in the spatial frequency space along an ellipse. Figure 3.6 shows the hypothetical (u, v)-coverage for the WSRT in the 2×48 configuration and for an observing time of 12.5 hours. The different ellipses represent the spatial frequencies which are measurable with the corresponding interferometer configuration. The ensemble of ellipses is the mentioned sampling function.

3.6   Short-spacing problem

As already mentioned in Section 3.1, interferometers are not able to measure the total flux (and therefore the total column density of a source). As can be seen in Figure 3.6, there is a region in the (u, v)-coverage (around the center) where a determination of the visibility is impossible. This is due to the fact that the individual telescopes cannot be placed arbitrarily close together.

The minimal achievable telescope separation $d_{\min}$ (which corresponds to the minimal spatial frequency) converts after inverse Fourier transformation to a limit for the maximal angular scale $\Theta_{\max}$ in position space which can be observed. An interferometer is therefore not able to measure extended, diffuse structures. This is called short-spacing

XX YY   HS0810_uvflag_attsys_gain.mir 1.4217 GHz
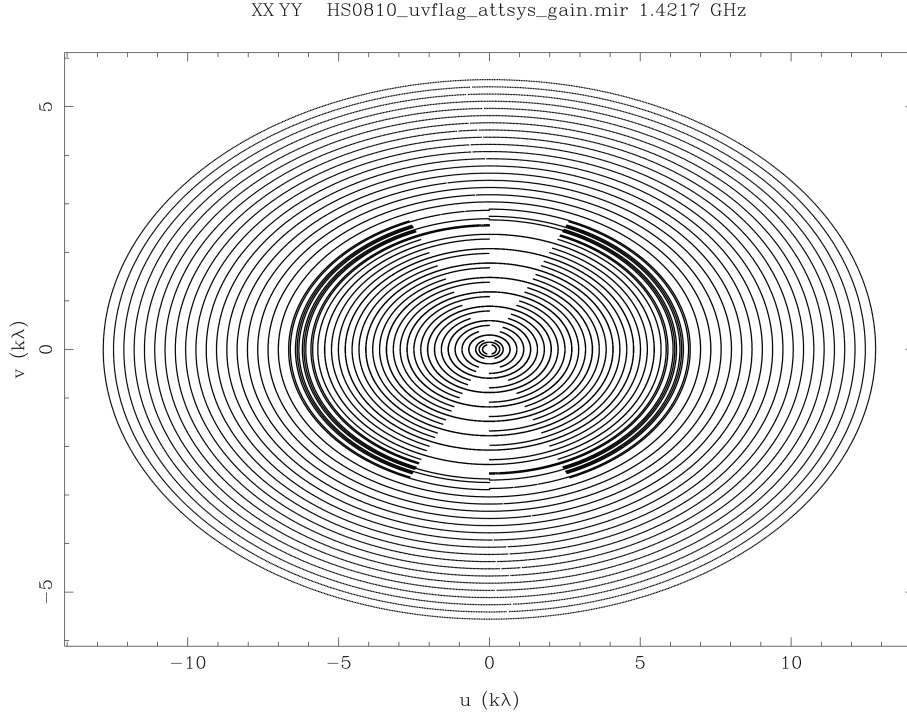
Fig. 3.6: Example for an observed u, v coverage (WSRT) for 14 antennae in the 2×48
configuration and 12.5 hours observing time. The declination of the observed source
J081331+254503 is $\delta(J2000) = 25°45'03.2''$.

problem. There is also a maximal separation $d_{\max}$ of the individual telescopes in an array
(determined by the size of the interferometer array), which corresponds to an upper spatial
frequency. Therefore, $d_{\max}$ determines the angular resolution of the interferometer.

In contrast, single dish telescopes measure the extended sources which corresponds to
the small spatial frequencies in the Fourier domain. Hence, single dish telescopes are able
to measure the total flux (total power), which corresponds to a spatial frequency of zero

$$\mathcal{F}(f(x))|_{k=0} = \int_{-\infty}^{\infty} f(x) \exp(-ikx)|_{k=0} \mathrm{d}x = \int_{-\infty}^{\infty} f(x)\mathrm{d}x = I(x) \, . \qquad (3.15)$$

3.7   Weighting

In radio astronomy there are three main methods for weighting the visibilities. The *natural
weighting* gives constant weights to all visibilities. This weighting gives optimum point-
source sensitivity by minimising the noise level in an image. However the synthesised
beam-shape and sidelobe levels are usually poor.

On the other hand, the *uniform weighting* gives a weight inversely proportional to the
sampling density function. This form of weighting minimises the sidelobe level. However
the noise level can be a factor of two worse than for natural weighting (Sault, B., Killeen,
N. 2004).

A compromise between the two methods provides the *robust weighting*. In interfero-
metric reduction programs, the so-called robustness parameter r can be used to weight the

hs0810+2554

Declination (J2000)

+28°

+26°

+24°

+22°

8ʰ30ᵐ   8ʰ20ᵐ   8ʰ10ᵐ   8ʰ00ᵐ

Right Ascension (J2000)
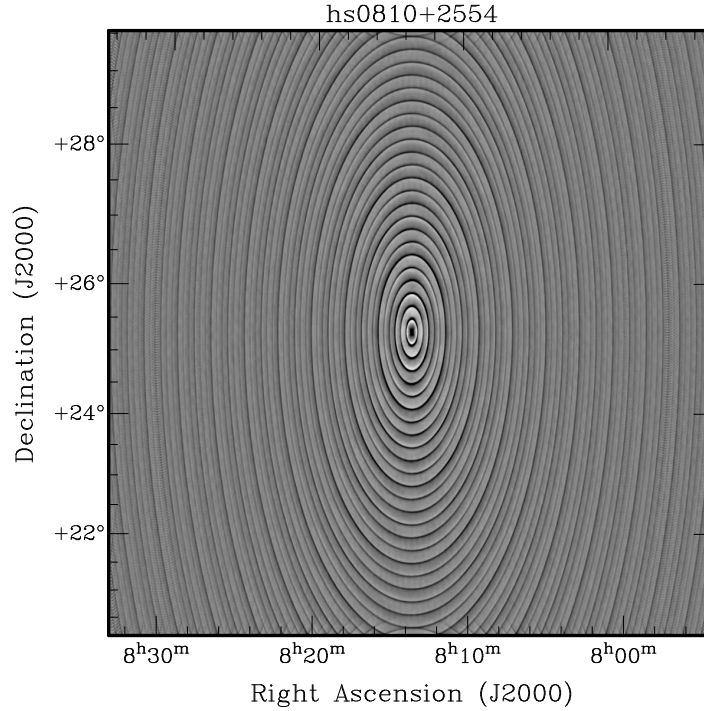
Fig. 3.7: Example of a dirty beam (WSRT) for the configuration 2×48 and 12.5 hours observing time. The direction of the observed source is $l = 197°$ and $b = 29°$.

visibilities. A robustness parameter of $r \leq -2$ corresponds to uniform weighting and $r \geq 2$ corresponds to natural weighting. With $r \approx 0.5$ one obtains nearly the same sensitivity as natural weighting but with a significantly better dirty beam.

3.8   Deconvolution

As described in Section 3.3 the observed intensity (dirty map) is the actual intensity of the source convolved with the dirty beam. Figure 3.7 shows a dirty beam which is the Fourier transformation of the sampling function; see Eq. (3.14). The aim of the data reduction is to reconstruct the actual intensity out of the dirty image by a deconvolution which suppresses the side lobes of the dirty beam. There are two common deconvolution methods used for this purpose, CLEAN (Högbom 1974) and the maximum entropy method (MEM) (Rohlfs & Wilson 2004; Sault, B., Killeen, N. 2004; Cornwell & Evans 1985).

In this work we will use the CLEAN method, which shall be briefly described. The algorithm produces a so-called model consisting of a set of point sources. This is achieved by searching the dirty image (cube) for the pixel containing the highest intensity. The

associated intensity value is multiplied with a factor of $\lesssim 0.1$ and added to the model. Simultaneously, the same intensity value multiplied with the dirty beam function is subtracted from the dirty image. This is repeated until the dirty image contains only noise (or a certain threshold is reached). Finally, the model is smoothed with a Gaussian of similar size as the main beam of the synthesised antenna pattern (dirty beam) and the residual noise from the dirty image is added.

Data acquisition and reduction

Since 21 cm surveys of the Milky Way's circumgalactic gas are typically limited to H I
*column densities above 10^{18} cm^{-2}, it is a good alternative to search for gaseous structures
with lower neutral gas column densities using high-resolution optical and ultraviolet (UV)
absorption spectroscopy towards extragalactic background sources like QSOs. In this work
we analysed UV and optical data observed with the VLT/UVES spectrograph. The absorption
line measurements were complemented by single-dish* H I *data (where possible).
Furthermore, four sightlines were additionally observed with high-resolution radio syntheses
telescopes, the WSRT and VLA. This strategy allows us to study the low column density
part of the intermediate- and high-velocity gas distributed in the Galactic halo which often
cannot be detected in all-sky 21 cm surveys.*

*This chapter presents the different datasets which were used for the analysis. A few
words will be said about the characteristics of the instruments with which the data were
observed. Furthermore, the data reduction for the various datasets will be briefly discussed.*

4.1 Resolution and detection significance

The resolution of a spectrograph is the smallest wavelength separation which the instrument
can resolve. For a given wavelength λ the resolving power is defined as

$$R = \frac{\lambda}{\Delta\lambda} \tag{4.1}$$

with $\Delta\lambda$ the resolution — the smallest wavelength separation which can be measured.
One has to distinguish between the physical resolution of the spectrograph, $\Delta\lambda_r$, and the
size of a pixel element, $\Delta\lambda_p$. To decide whether a detected signal is significant or not, the
so-called signal-to-noise ratio

$$\text{SNR} = \frac{I_{\text{signal}}}{\sigma_{\text{rms}}} \tag{4.2}$$

is used, which compares the level of a signal to the level of the background noise. I_{signal} is
the (peak) intensity of the spectral line and σ_{rms} the standard deviation of the (continuum)

noise level. The SNR per resolution element is linked to the SNR of a pixel element via (for a detailed discussion see Erni 2007)

$$\mathrm{SNR}_r = \sqrt{\frac{\Delta\lambda_r}{\Delta\lambda_p}} \cdot \mathrm{SNR}_p \,. \tag{4.3}$$

We define the detection significance x in units of σ_rms for a measured equivalent width W_λ, a given resolution R of a spectrograph and the wavelength λ as

$$x[\sigma_\mathrm{rms}] = \frac{W_\lambda}{\Delta\lambda_r}\mathrm{SNR}_r = \frac{W_\lambda R \cdot \mathrm{SNR}_r}{\lambda} \,. \tag{4.4}$$

It not only considers the peak value of a spectral line (which determines the SNR) but also the width of the profile.

4.2 Ultraviolet and optical data

This section deals with the observation and reduction of the UV data.

4.2.1 Ultraviolet and Visual Echelle Spectrograph at the VLT

The data basis of our analysis are optical and ultraviolet spectra of low- and high-redshift QSOs obtained between 1999 and 2004 with the Ultraviolet and Visual Echelle Spectrograph (UVES) at the ESO Very Large Telescope (VLT). These spectra, observed for different purposes by various groups, are publically available in the ESO data archive.[1]

UVES is a cross-dispersed Echelle spectrograph which operates from the atmospheric cut-off at 300 nm to the long wavelength limit of about 1100 nm. To achieve such a large bandwidth, the light beam from the telescope is split into two arms (UV to blue, and visual to red) within the instrument. Both arms can be operated separately or in parallel via a dichroic beam splitter. The resolving power is $R \sim 40000$ when a $1''$ slit is used. The maximum resolution is $R \sim 80000$ or $R \sim 110000$ in the blue- and the red Arm, respectively. A detailed description of the UVES instrument is given by Dekker et al. (2000).

The 177 spectra used in this study have a spectral resolution of $R \sim 42000$, corresponding to a velocity resolution of about $6.6\,\mathrm{km\,s^{-1}}$. To have a measure for the general quality of a normalized spectrum we define the *inverse noise level* per resolution element

$$\mathrm{INL}_r = \sqrt{\frac{\Delta\lambda_\mathrm{r}}{\Delta\lambda_\mathrm{p}}}\frac{1}{\sigma_\mathrm{p}^\mathrm{rms}} \,, \tag{4.5}$$

which equals SNR_r for a saturated absorption line (having $I_\mathrm{signal} = 1$). For the two $\lambda\lambda 3934.8, 3969.6$ Ca II ($\lambda\lambda 5891.6, 5897.6$ Na I) lines INL_r is between $10\,(25)$ and $190\,(410)$ with a median value of about $90\,(100)$.

Some of the spectra were reduced with the UVES pipeline implemented in the ESO-Midas software-package as part of the data reduction process of the UVES Large Programme (Bergeron et al. 2004). The pipeline reduction includes flat-fielding, bias- and

---

[1] http://archive.eso.org

sky-subtraction, and a relative wavelength calibration. The data were normalised via a continuum fit using polynomials. The remaining data were reduced and normalised by an automated procedure with a modified version of the UVES pipeline as part of the SQUAD project (Murphy et al. 2008, in preparation).

As we use the Ca II and Na I doublets, we define a detection limit 4σ for the stronger line of the doublets and a 2σ limit for the weaker lines. For the median (minimal, maximal) SNR_r of about 90 (10, 190) for Ca II and 100 (25, 410) for Na I the former limits corresponds to equivalent width limits of $W_\lambda^{\mathrm{CaII}} \approx 4\,\mathrm{m\AA}$ (50 mÅ, 2 mÅ) and $W_\lambda^{\mathrm{NaI}} \approx 6\,\mathrm{m\AA}$ (23 mÅ, 1 mÅ). Assuming optically thin absorption, these limits can be converted to column density detection limits using

$$N = \frac{W_\lambda\, \mathrm{m_e c^2}}{\pi\, \mathrm{e^2}\, \lambda^2\, f}.\eqno(4.6)$$

resulting in $\log(N_{\mathrm{CaII}}^{\mathrm{median}}/\mathrm{cm}^{-2}) = 10.67$ and $\log(N_{\mathrm{NaI}}^{\mathrm{median}}/\mathrm{cm}^{-2}) = 10.44$.

4.2.2   Voigt-Profile fitting with MIDAS

For the further analysis, as mentioned before, the pre-reduced and normalised UVES data were processed with MIDAS (Ballester 1992; Ballester et al. 2000). The first step was to convert the measured frequencies into LSR velocities. To get the information about the b-values and the column densities along the lines of sight, Voigt profiles were fitted into the spectral lines via the method of χ^2-minimisation. The ESO-MIDAS LYMANFIT programme enables the simultaneous fitting of one or more components being different transitions of the same element. This allows to analyse weak absorption lines and to get more accurate results. One should avoid saturated lines in the fit procedure because of the less accurate results.

4.3   H I data

The following paragraphs present the H I data obtained with a single-dish telescope and high-resolution radio interferometers. The steps of the data reduction will be discussed.

4.3.1   Single dish observations

100-m telescope at Effelsberg

Follow-up H I 21 cm observations were obtained in 2006 and 2007 with the 100-m radio telescope at Effelsberg. At 21 cm wavelength its HPBW is $9'$. The different sources were observed with the 8192-channel autocorrelator (AK90), which has a bandwidth of 10 MHz. To maximise the integration time spent on the source in-band frequency switching was used. For our observations, the velocity resolution is about $0.5\,\mathrm{km\,s^{-1}}$, and the rms is about $4\dots6\cdot10^{-2}\,\mathrm{K}$. The integration time per sight line was between 15 and 20 min.

To calibrate the data, the standard flux calibration source S7 was observed at the beginning and at the end of each observing period. The next step was the stray radiation correction based on the work of Kalberla et al. (1980). Stray radiation is emission which enters the receiver through the side lobes of the antenna. Depending on the observed direction in the sky, stray radiation can make up to 50% of the detected signal. The
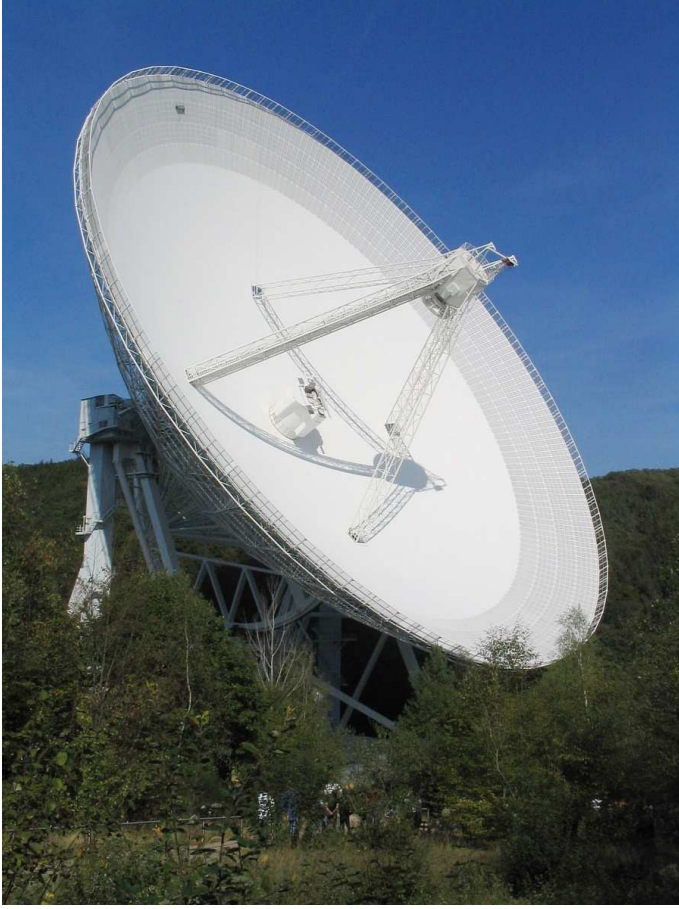
Fig. 4.1: The 100-m telescope at Effelsberg. The photo was taken by Tobias Westmeier.

stray radiation affects, depending on the direction, different radial-velocity ranges. These velocity ranges overlap with radial velocities observed in several IVCs and lead to erroneous flux measurements. HVCs are usually not affected by stray radiation as they lie in different radial velocity regimes.

The resulting spectra were analysed using the GILDAS tool CLASS[2]. Polynomial baselines of up to 4th order were fitted and substracted from the data. For this purpose, windows were set individually around the line emission. All data within these windows were not considered by the fit. The spectra were averaged over both polarisations and Gaussian functions were fitted to the spectral lines. A 3σ detection limit was used as detection criterion for the line emission.

The Leiden-Argentine-Bonn Survey (LAB)

Furthermore, we used data from the Leiden-Argentine-Bonn (LAB) all-sky H I 21 cm survey (Kalberla et al. 2005b) for the sight lines where observations with the 100-m telescope were not possible to search for H I emission in IVCs and HVCs.

The LAB survey is a combination of the Leiden/Dwingeloo Survey (LDS, Hartmann & Burton 1997), covering the sky north of $\delta = -30°$, and the Instituto Argentino de

---

[2] http://www.iram.fr/IRAMFR/GILDAS

Radioastronomía Survey (IAR, Arnal et al. 2000; Bajaja et al. 2005), which covers the sky south of $\delta = -25°$. The HPBW of the LAB survey is about $36'$ (the effective resolution is about $1°$, because the LAB survey is not fully sampled). The LSR velocity coverage is in the range of $-450\,\mathrm{km\,s^{-1}}$ to $+400\,\mathrm{km\,s^{-1}}$ at a velocity resolution of $1.3\,\mathrm{km\,s^{-1}}$. The entire LAB data were combined and corrected for stray radiation at the Argelander-Institut für Astronomie in Bonn (Kalberla et al. 2005b).

4.3.2   Radio Interferometer observations

For four of the sight lines with intermediate- and high velocity Ca II and Na I absorption and corresponding H I emission we obtained additional high-resolution data with the Very Large Array (VLA) and the Westerbork Synthesis Radio Telescope (WSRT) to search for small-scale (pc or sub-pc scales) structures within the gas clouds. At $\lambda = 21\,\mathrm{cm}$, both instruments have a synthesised beam of less than $1'$ (FWHM), leading to high spatial resolution. The observations with WSRT and VLA therefore partially resolve the structure of the absorbing gas. In the following paragraphs, the properties of the instruments and the data reduction are discussed.

Westerbork Synthesis Radio Telscope (WSRT)

The WSRT consists of 14 antennas, each of which has a diameter of $25\,\mathrm{m}$. Ten of the dishes have a fixed location, while four at the eastern end of the array can be moved on rails. The WSRT data were recorded in February 2007 using the 2×48 configuration. This configuration provides a good compromise between sensitivity and resolution. Each observing period was preceded and followed by observations of calibration sources. A correlator bandwidth of $2.5\,\mathrm{MHz}$ was chosen. The spectral channel width is $0.5\,\mathrm{km\,s^{-1}}$ with a total of 1024 channels for each of the two polarisations. The observing time for both absorbers in the direction of J081331+254503 and QSO B1331+170 was $12\,\mathrm{h}$ with additional $1\,\mathrm{h}$ for the (primary) pre- and post-calibrators.

The WSRT data were analysed with the MIRIAD software package[3]. The first step was to flag bad datapoints in the source and calibrator datasets, in order to exclude these during the following reduction tasks. The primary calibrators were used for the absolute flux, phase, gain, and bandpass calibration. Due to phase changes during the $12\,\mathrm{h}$ observation, an additional relative phase calibration was necessary. For this purpose a self-calibration using the continuum sources in each field was performed. The continuum emission was substracted from the visibility data and the resulting phase solution was applied to the original data set.

Finally, data cubes were calculated via Fast Fourier Transformation (FFT) using a robust parameter of $r = 0.5$. The cubes have a velocity width of $0.5\,\mathrm{km\,s^{-1}}$ per spectral channel. The CLEAN algorithm (Högbom 1974) was applied to reconstruct the image. The resulting data cubes and moment-0 maps were primary-beam-corrected.

Very Large Array (VLA)

The VLA consists of 29 radio antennas in a Y-shaped configuration. Each antenna has a diameter of $25\,\mathrm{m}$. The VLA observations were carried out in February 2007 using the DnC

---

[3] ftp://ftp.atnf.csiro.au/pub/software/miriad/

Table 4.1: Observational parameters of the high resolution measurements with the WSRT and the VLA. Listed are the instrument used, the date of observation, the chosen configuration, the coordinates of the sources, field of view Ω_{HPBW}, the spatial Θ_{HPBW} and spectral resolution δv, the bandwidth $\Delta\nu$, and the resulting noise level σ_{rms} in the final datacubes.

| Instrument | Config. | l | b | Ω_{HPBW} | Θ_{HPBW} | δv | $\Delta\nu$ | σ_{rms} |
		[°]	[°]	[deg]	[″]	[km s^{-1}]	[MHz]	[mJy Beam^{-1}]
WSRT	2×48	348.5	75.8	0.5	80×180	2.5	2.5	9.9
	2×48	196.9	28.6	0.5	80×120	2.5	2.5	8.5
VLA	DnC	49.4	-78.6	0.5	100×100	1.3	1.56	10.6
	DnC	211.8	-32.1	0.5	100×100	1.3	1.56	13.3

configuration. This hybrid configuration consists of the southeast and southwest arms in the smallest (D) configuration and the northern arm in the larger C configuration. It is especially well suited for extended sources with a declination south of $\delta = -15°$. For each of the two polarisations the correlator has a bandwidth of 1.56 MHz with 256 spectral channels, resulting in a channel separation of 1.3 km s^{-1}.

The observing time for the sightline against QSO J0003−2323 was 6 h and 12 h for QSO B1331+170 with additional 1 h for the primary and secondary calibrators. The primary calibrators 0137+331 and 0542+498 were observed for about 30 min each at the beginning and the end of the three measuring periods of the source observations. The secondary calibrators 0025−260 and 0447−220 using for the additional phase calibration were observed once every hour for about 5 minutes.

The VLA data of QSO B0450−1310B and QSO J0003−2333 were contaminated by many interferences and antenna failures. As both sources were observed on multiple occasions, the individual parts had to be handled separately and were merged only after self-calibration. The data reduction was performed with MIRIAD. First, calibration based on the observed primary and secondary calibrators was done. A median filter was applied, and malfunctioning antennas as well as obvious interferences were flagged. Along with continuum subtraction, an iterative self-calibration was carried out to account for phase changes during the observations. After merging the respective visibility sets, data cubes were calculated via FFT using a robust parameter of $r = 0.4$ for QSO J0003−2333 and of $r = 2$ for QSO B0450−1310B. In order to improve sensitivity, the beam was artificially increased to a size of $100'' \times 100''$ by convolution with a Gaussian. The resulting data cubes have a velocity width of 1.3 km s^{-1} per spectral channel. Again, primary beam corrections were applied. All information about the WSRT and VLA observations are summarised in Table 4.1

Results from Ca II (Na I) absorption and H I emission measurements

This chapter presents the results from the optical absorption and radio emission line measurements of low-column density Ca II, Na I and H I intermediate- and high-velocity clouds in the Galactic halo. Ca II (Na I) absorption is found along 47 (25) out of 177 studied lines of sight.[1] In total, 78 (30) individual Ca II (Na I) absorption components are found. The analysis of the data obtained with the WSRT and VLA reveals the presence of compact and cold low-column density clumps of neutral atomic hydrogen in these directions. This result indicates that the Milky Way halo contains a large number of low-column density gas structures.

5.1 Previous studies

Ground- and space based spectroscopic instruments like UVES, STIS, and FUSE enable us to study the gaseous halos of galaxies (in particular the Milky Way) in absorption against QSOs. Absorption spectroscopy has the advantage that it is very sensitive to low column densities ($\log(N_{\mathrm{HI}}/\mathrm{cm}^{-2}) \gtrsim 11$) which are undetectable in emission. Of particular interest for the analysis of the low-column density, multi-phase extraplanar gas are the FUV and UV wavelength regimes, because several atomic and molecular species have their transitions in the range between $900\ldots4000\,\text{Å}$. Furthermore, some well detectable metal lines are also visible in the optical regime, i.e., the Na I D doublet. The combination of absorption line measurements together with H I emission line observations provide a powerful diagnostic method to study the halo gas of galaxies in detail for both low and high redshift.

The observation of absorption line systems in the halo of the Milky Way were up to now mostly focused on to 21 cm *emission-selected* LVCs, IVCs, and HVCs. Relatively

---

[1] Note, that in some cases either one or both of the spectral regimes containing the Ca II and Na I absorption could not be used due to instrumental issues or blending. The number of sight lines which could be used to search for Ca II (Na I) features were 146 (155).

● Sight lines observed with UVES and Effelsberg. There are observed absorption and corresponding emission lines
▲ Sight lines observed with UVES and Effelsberg. There are only absorption lines in the UVES data
⬣ Sight lines observed with UVES, Effelsberg and the VLA or WSRT
■ Sight lines with absorption lines observed with UVES. No Effelsberg observations are available.
○ Sight lines observed with UVES with no absorption lines .

Fig. 5.1: HVC-all-sky column density map created by Westmeier (2007) based on the data of the LAB Survey (Kalberla et al. 2005b). The different symbols mark the positions of 177 sight lines that were observed with UVES. Along 53 lines of sight we detect halo Ca II and Na I absorption components. For 27 of them we have obtained additional H I observations with the Effelsberg 100-m telescope. Four sight lines were re-observed with high resolution radio synthesis telescopes.

little effort has been made to investigate the connection between the Galactic population of IVCs and HVCs and the distribution and nature of intervening metal-absorption systems from halos of other galaxies seen in QSO spectra. To statistically compare the absorption characteristics of the extraplanar Galactic halo structures with the properties of intervening metal-absorption systems towards QSOs one requires an *absorption-selected* dataset of IVCs and HVCs. Therefore, Richter et al. (2005) started to analyse archival optical data to search for Ca II absorption in spectra of distant QSOs that are randomly distributed on the sky. These absorption line systems are reliable tracers of neutral hydrogen in intermediate- and high-velocity extraplanar gas clouds at low H I column densities. From a first inspection, Richter et al. (2005) found Ca II in about 50% of the QSO sight lines, also in directions where no corresponding H I emission was found in the data of large H I surveys like the LAB survey. These results imply that the Milky Way halo is filled with low-column density neutral gas.

5.2   UV- and single-dish H I data

Figure 5.1 shows an all-sky HVC map (Section 1.2.2) which was created by Westmeier (2007) based on the data of the LAB survey (Kalberla et al. 2005b). The symbols mark the positions of the 177 sight lines that were observed with UVES.

For the further analysis we have transformed all spectra to the Local Standard of Rest (LSR) velocity scale. Note, that most of the gas near zero velocities is located in the Galactic disk. To separate low-velocity gas in the disk from extraplanar intermediate- and high-velocity gas in the halo we have used the concept of the so-called deviation velocity (see Section 1.2.1) together with a kinematic model for the Milky Way developed by Kalberla (2003) and Kalberla et al. (2007). With this model we can determine whether an observed velocity in a given direction is expected for interstellar gas participating in the Galactic disk rotation or not. To distinguish between IVCs and HVCs we use the definition of Wakker (1991) in which a cloud is defined as IVC, if $|v_{\mathrm{dev}}| \leq 50\,\mathrm{km\,s^{-1}}$ and as HVC if $|v_{\mathrm{dev}}| > 50\,\mathrm{km\,s^{-1}}$; see Section 1.2.1. Using these selection criteria for the 177 UVES spectra we detect 78 Ca II and 30 Na I halo absorption components along 53 lines of sight at intermediate and high velocities. These 53 sight lines are indicated in Fig. 5.1 with the filled symbols. For 27 of these sight lines we have carried out deep H I 21 cm observations with the Effelsberg 100-m telescope. Additionally, for all sight lines we searched for associated emission in the LAB survey (Kalberla et al. 2005b).

Figure 5.2 shows one examplary spectrum with optical absorption of Ca II λ3934.77 Å, Ca II λ3969.59 Å, Na I λ5891.58 Å, Na I λ5897.56 Å together with the corresponding H I λ21 cm emission profiles observed with the 100-m telescope at Effelsberg and LAB. A complete presentation of the 53 obtained spectra is given in Appendix A.2.

Some of the halo Ca II and Na I absorbers show multiple components, indicating the presence of sub-structures. Along 14 sight lines the intermediate- and high-velocity Ca II and Na I absorption is connected with H I gas (detected with the 100-m telescope) with typical column densities in the range of a few times $10^{18}\,\mathrm{cm^{-2}}$ up to $10^{20}\,\mathrm{cm^{-2}}$. The measured H I line widths vary from $\Delta v_{\mathrm{FWHM}} = 3.2\,\mathrm{km\,s^{-1}}$ to $32.0\,\mathrm{km\,s^{-1}}$, giving a range of upper temperature limits of $250\,\mathrm{K}$ up to about $22500\,\mathrm{K}$ (using Eq. (2.31)) for the gas. To allow a comparison of the H I line widths (given in Δv_{FWHM}) with that of the Ca II and Na I lines (given as b-values), we convert Δv_{FWHM} into b-values using Eq. (2.13) and (2.31). Measured column densities and b-values (UVES and Effelsberg) for the 53 sight lines are summarised in Table 5.1. Note, that there is only one single case (QSO B0438$-$166) where no Ca II but Na I was detected.

It is important to note at this point that in many cases there is no high- or intermediate-velocity H I 21 cm emission seen in the low-resolution LAB survey, whereas the higher resolution 100-m telescope detects emission lines at the corresponding position and velocity. This demonstrates how important high-resolution measurements are, considering beam smearing effects and the fact that the H I column densities of most of the Ca II and Na I absorption components are close to or below the detection limit of large H I surveys. In our sample, 13 sight lines out of 27 show intermediate- or high-velocity Ca II and Na I absorption without any corresponding counterparts in the H I data, suggesting that either the H I column densities are below the detection limit of the Effelsberg radio telescope or that the diameters of these clouds are very small so that beam-smearing effects make them undetectable.

The directions of several of the intermediate- and high-velocity absorbing systems as well as their velocities indicate a possible association with known large and extended HVC or IVC complexes, independent of whether they are detected in 21 cm or not. Other sight lines, in contrast, do not appear to be associated with any known HVC or IVC complexes. Obviously, optical absorption spectra allow us to trace the low neutral column density

Table 5.1: Summary of the UVES and Effelsberg measurements for intermediate- and high-velocity Ca II and Na I absorbers towards 53 QSOs. The columns give the name of the QSOs, coordinates, LSR and deviation velocities, Ca II and Na I column densities, b-value for the Ca II and Na I lines, H I column densities, and the converted b-values for the H I lines. A possible association with known HVC or IVC complexes is indicated as well. n/a means defect spectrum, blending or not observed (in case of H I). A non-detection is denoted with a "-".

QSO	l [°]	b [°]	v_{LSR} [km s^{-1}]	v_{dev} [km s^{-1}]	$\log N_{\mathrm{CaII}}$ [N in cm^{-2}]	b_{CaII} [km s^{-1}]	$\log N_{\mathrm{NaI}}$ [N in cm^{-2}]	b_{NaI} [km s^{-1}]	$\log N_{\mathrm{HI}}$ [N in cm^{-2}]	b_{HI} [km s^{-1}]	HVC/IVC complex*
QSO J1232-0224	293.2	60.1	−21	−21	11.5	2	11.0	1	19.9	10	-
QSO B1101-26	275.0	30.2	199	199	11.7	6	-	-	-	-	LA
			−17	−17	11.7	6	11.2	3	20.1	7	-
			−27	−27	11.3	4	-	-	-	-	-
QSO J0003-2323	49.4	−78.6	−98	−85	11.9	6	-	-	-	-	MS
			−112	−99	11.8	6	-	-	19.6	19	MS
			−126	−113	11.9	6	-	-	-	-	MS
QSO B0450-1310B	211.8	−32.1	−5	−5	n/a	n/a	11.5	5	20	2.3	-
			−20	−20	n/a	n/a	12.0	2	19	6.8	-
QSO B0515-4414	249.6	−35.0	−5	−5	11.7	3	9.4	2	n/a	n/a	-
			−17	−17	10.9	1	-	-	n/a	n/a	-
			−41	−41	11.3	4	10.8	3	n/a	n/a	-
			−58	−58	11.3	1	-	-	n/a	n/a	-
QSO B1036-2257	267.4	30.4	−24	−24	11.9	7	12.0	1	19.6	2	-
QSO J1344-1035	323.5	50.2	−65	−60	11.8	4	-	-	-	-	-
QSO B0109-353	275.5	−81.0	79	46	12.4	7	11.0	6	n/a	n/a	-
			−108	−142	12.4	7	-	-	n/a	n/a	MS
			−162	−197	12.3	12	-	-	n/a	n/a	MS
QSO B1448-232	335.4	31.7	−100	−68	10.9	2	-	-	-	-	L
			−130	−99	11.6	9	-	-	-	-	L
			−150	−119	11.6	1	11.8	2	18.9	5	L
			−157	−126	11.5	5	-	-	-	-	L

Table 5.1: *continued.*

QSO	l [°]	b [°]	v_{LSR} [km s^{-1}]	v_{dev} [km s^{-1}]	$\log N_{\text{CaII}}$ [N in cm^{-2}]	b_{CaII} [km s^{-1}]	$\log N_{\text{NaI}}$ [N in cm^{-2}]	b_{NaI} [km s^{-1}]	$\log N_{\text{HI}}$ [N in cm^{-2}]	b_{HI} [km s^{-1}]	HVC/IVC complex*
QSO J2155-0922	47.5	−44.8	−166	−78	11.1	1	-	-	-	-	GCN
			−209	−121	11.8	6	-	-	-	-	GCN
QSO J1211+1030	271.7	70.9	76	32	11.5	2	-	-	-	-	-
			−26	−26	11.6	4	-	-	19.7	14	IV Spur?
J143649.8-161341	336.6	39.7	76	24	11.4	3	-	-	-	-	-
LBQS 0049-2820	302.7	−89.1	−118	−118	11.6	3	-	-	n/a	n/a	MS
			−171	−171	12.0	8	-	-	n/a	n/a	MS
			−186	−186	11.2	1	-	-	n/a	n/a	MS
			−205	−205	12.1	3	-	-	n/a	n/a	MS
QSO B0002-422	332.7	−72.4	89	76	11.8	6	-	-	n/a	n/a	MS
QSO B0122-379	271.9	−77.3	40	14	11.7	4	-	-	n/a	n/a	MS
QSO B1347-2457	319.5	35.8	−95	−77	11.5	3	-	-	-	-	-
J092913-021446	235.7	33.2	176	45	11.7	3	-	-	-	-	WA
J081331+254503	196.9	28.6	−23	−23	n/a	n/a	11.1	5	19.8	37	-
J222756-224302	32.6	−57.3	−118	−77	12.1	7	-	-	-	-	-
QSO J0830+2411	200.0	31.9	−21	−21	n/a	n/a	11.3	3	19.2	8	-
QSO B0952+179	216.5	48.4	−30	−30	n/a	n/a	11.6	9	n/a	n/a	IV Spur
J135256-441240	314.4	17.3	−107	−66	12.1	4	11.1	6	n/a	n/a	-
			−115	−74	12.3	1	11.2	6	n/a	n/a	-
			−125	−84	11.7	3	-	-	n/a	n/a	-
			−51	−10	11.7	3	-	-	n/a	n/a	-
LBQS 1246-0217	301.9	60.3	−21	−21	12.0	8	-	n/a	n/a	-	IV-Spur
J030211-314030	230.0	−61.3	−209	−209	12.9	10	-	n/a	n/a	-	MS?
QSO B1212+3326	173.1	80.1	−37	−34	11.0	4	11.0	2	-	-	IV Arch?
			−49	−47	11.5	2	10.5	2	19.7	18	IV Arch?
			−57	−52	11.6	8	-	-	-	-	IV Arch?
			−76	−73	11.0	4	-	-	-	-	IV Arch?

Table 5.1: *continued.*

QSO	l [°]	b [°]	$v_{\rm LSR}$ [km s^{-1}]	$v_{\rm dev}$ [km s^{-1}]	$\log N_{\rm CaII}$ [N in cm^{-2}]	$b_{\rm CaII}$ [km s^{-1}]	$\log N_{\rm NaI}$ [N in cm^{-2}]	$b_{\rm NaI}$ [km s^{-1}]	$\log N_{\rm HI}$ [N in cm^{-2}]	$b_{\rm HI}$ [km s^{-1}]	HVC/IVC complex*
QSO B2314-409	352.0	−66.3	−37	−37	12.1	7	-	-	n/a	n/	IV Spur
			−56	−56	11.9	5	-	-	n/a	n/a	IV Spur
QSO J1356-1101	327.7	48.7	−108	−101	12.0	6	n/a	n/a	-	-	-
QSO B0458-0203	201.5	−25.3	−7	−7	12.1	4	12.1	2	19.3	3	AC shell
QSO J0103+1316	127.3	−49.5	−351	−258	11.7	4	n/a	n/a	-	-	-
QSO J0153-4311	268.9	−69.6	124	75	12.4	6	-	-	n/a	n/a	MS
QSO B0216+0803	156.9	−48.7	11	11	n/a	n/a	12.1	1	19.8	9	-
QSO B2348-147	72.1	−71.2	91	91	11.4	1	n/a	n/a	-	-	MS
QSO J0139-0824	156.2	−68.2	−100	−76	12.2	2	-	-	-	-	MS
QSO B0112-30	245.5	−84.0	−13	−13	11.9	2	13.1	1	n/a	n/a	-
QSO J0105-1846	144.5	−81.1	192	192	11.4	1	-	-	-	-	MS
			167	167	11.2	3	-	-	-	-	MS
			108	108	11.4	2	11.0	3	-	-	MS
J142253-000149	345.7	55.1	−12	−9	12.8	2	11.6	3	n/a	n/a	IV-Spur, L?
QSO B1104+0104	255.1	53.7	−27	−27	12.3	7	12.7	2	n/a	n/a	IV-Spur
QSO J0256+0110	174.7	−48.8	8	19	11.7	4	12.1	3	n/a	n/a	-
QSO J0911+0551	224.7	33.7	−27	−27	11.7	1	10.7	1	n/a	n/a	IV-Spur
QSO B1140+2711	209.8	74.7	−43	−43	12.3	8	-	-	n/a	n/a	IV-Spur/-Arch
QSO B2225-404	359.8	−57.8	−122	−63	12.5	1	-	-	n/a	n/a	MS?
QSO B1126+0220	261.4	58.2	71	71	11.6	4	-	-	n/a	n/a	-
			85	85	11.4	2	-	-	n/a	n/a	-
QSO B0951+0815	228.9	43.9	−49	−49	11.8	3	-	-	n/a	n/a	IV-Spur
QSO J0423-2618	224.7	−42.9	177	177	11.9	5	-	-	n/a	n/a	-
J012944-403346	274.9	−74.4	−33	−33	11.5	5	-	-	n/a	n/a	MS?

Table 5.1: *continued.*

QSO	l	b	v_{LSR}	v_{dev}	$\log N_{\mathrm{CaII}}$	b_{CaII}	$\log N_{\mathrm{NaI}}$	b_{NaI}	$\log N_{\mathrm{HI}}$	b_{HI}	HVC/IVC
	[°]	[°]	[km s^{-1}]	[km s^{-1}]	[N in cm^{-2}]	[km s^{-1}]	[N in cm^{-2}]	[km s^{-1}]	[N in cm^{-2}]	[km s^{-1}]	complex*
QSO J1039-2719	270.0	27.0	184	17	11.3	5	-	-	-	-	WD
			−11	−11	12.6	1	11.6	6	20.1	6.8	-
J123437-075843	290.4	70.4	88	49	11.6	2	-	-	-	-	-
			74	35	11.9	7	-	-	-	-	-
QSO B1331+170	348.5	75.8	−9	−9	12.4	11	11.3	6	18.9	2.7	-
			−27	−27	12.0	5	11.3	3	-	-	IV Spur
QSO J1429+0117	349.2	55.1	−19	−19	11.8	3	-	-	n/a	-	-
QSO B0438-166	214.1	−36.25	−14	−14	-	-	12.1	2	n/a	-	-
J120342+102831	266.6	69.9	−35	−35	11.9	8	11.4	2	n/a	-	IV-Spur
J144653+011355	354.7	52.1	16	8	11.8	4	-	-	-	-	-
			−48	−47	11.5	4	-	-	-	-	-
LBQS 0042-2930	335.8	−87.5	−28	−28	12.2	3	11.6	2	n/a	-	MS?

* LA – Leading Arm, MS – Magellanic Stream, GCN – Galactic Center North, IV Spur – Intermediate-velocity Spur,
IV Arch – Intermediate-velocity Arch, AC shell – Anti-center shell
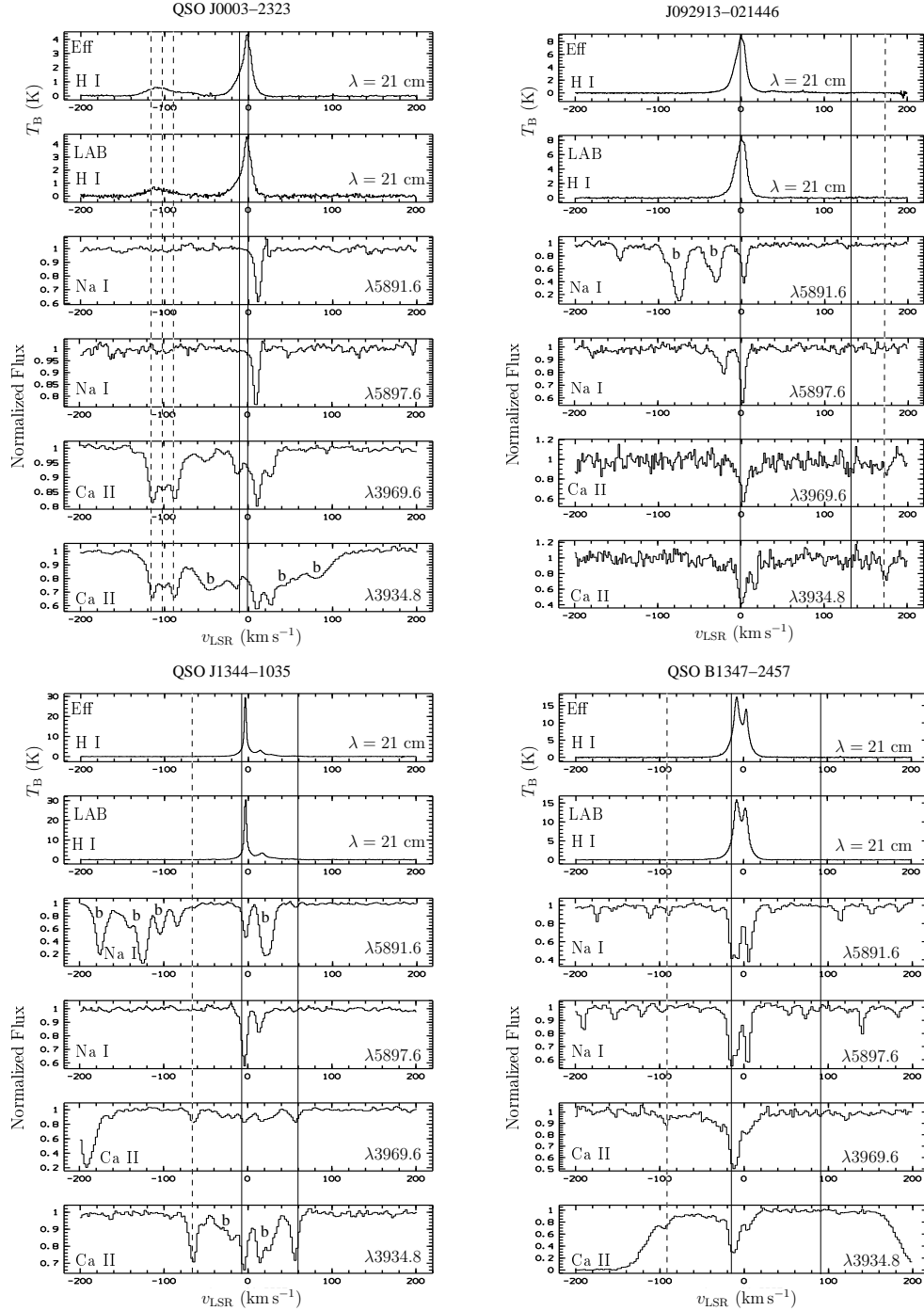
Fig. 5.2: Ca II and Na I absorption and H I emission spectra in the direction of the QSOs QSO J0003−2323, J092913−021446, QSO J1344−1035, and QSO B1347−2457 obtained with UVES and the 100-m telescope at Effelsberg. Additionally shown are the archival H I data from the Leiden-Argentine-Bonn (LAB) survey (Kalberla 2003). The location of the absorption and corresponding emission lines are indicated by dashed lines. The solid lines mark the minimal and maximal LSR velocity which is expected for the Galactic disc gas in the particular sky direction according to the Milky Way model developed by Kalberla (2003); Kalberla et al. (2007). Blended lines from intervening absorption systems are denoted with b.

Fig. 5.3: VLA 21 cm column density map of high-velocity H I gas in the direction of QSO B1448−232 (Richter et al. 2005). Several compact, cold clumps with low H I column densities ($\lesssim 10^{19}\,\mathrm{cm}^{-2}$) were detected.
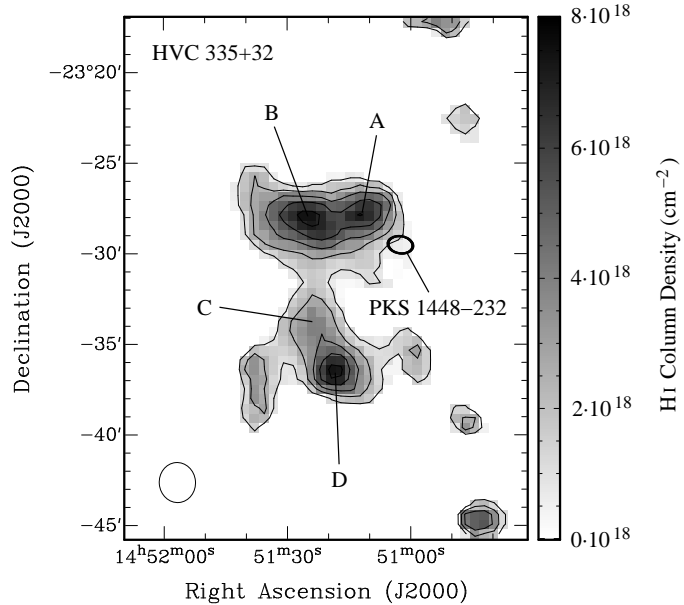
environment of the Galactic halo much better than 21 cm emission measurements. The distribution of neutral or weakly ionised gas is more complex than indicated by H I 21 cm observations alone.

Although the column densities have been measured with high accuracy, observations with high-resolution synthesis telescopes would be required to determine the Ca or Na abundances of the intermediate- and high-velocity gas (see Section 7). Other difficulties of Ca and Na determination are the complex ionisation properties of singly ionised calcium and neutral sodium as well as dust depletion effects which introduce uncertainties in elemental abundances studies of these species (see Wakker & Mathis 2000). Note, that ionised material may represent a significant if not dominating fraction of the total gas amount in and around these halo clumps. The ionisation stage and the depletion of an element depends on the physical conditions in the halo, which may vary from location to location (Sembach & Savage 1996). Another critical aspect is that many of the sight lines have blending problems with high-redshift ($z > 2$) Lyman-α forest lines. The consequence is that a significant fraction of Ca II and Na I high-velocity features may even remain unnoticed.

5.3 High-resolution H I data

Based on the above mentioned results we have used high-resolution H I data to search for small-scale structures embedded in the halo gas clouds that are not resolved with the Effelsberg telescope. Richter et al. (2005) observed one sight line (QSO 1448−232) with particularly prominent high-velocity Ca II and Na I absorption lines with UVES, Effelsberg and the VLA; see Fig. 5.3. The high-resolution VLA H I data resolve the HVC into several compact, cold clumps. As part of this PhD project we obtained high-resolution 21 cm observations for two additional sight lines with the WSRT (J081331+254503 and QSO B1331+170) and for two other sight lines with the VLA (QSO J0003−2323 and QSO B0450−1310B).

Table 5.2: Summary of the physical properties of the clumps observed in the direction of the QSOs J081331+254503 and QSO B1331+170 with the WSRT and QSO J0003−2323 and QSO B0450−1310B with the VLA. The columns give the name of the QSOs, the clumps, the coordinates, the velocities in the LSR frame, the FWHM derived from a Gauss fit and associated b-values, the peak Amplitude, the peak H I column density (with a typical error of about $10^{18}\,\mathrm{cm}^{-2}$), the peak brightness temperature, the upper temperature limit, and the mean radial size, ϕ (FWHM).

QSO	Clump	$\alpha(J2000)$ [h:m:s]	$\delta(J2000)$ [d:m:s]	v_{LSR} [km s^{-1}]	Δv_{FWHM} [km s^{-1}]	b_{HI} [km s^{-1}]	Amplitude [mJy/Beam]	N_{HI} [cm^{-2}]	T_{B} [K]	$T_{\mathrm{kin}}^{\mathrm{max}}$ [K]	ϕ [']
QSO J0003−2323	A	00:03:46	−23:05:55	−117.6	3.0 ± 0.4	1.8	86 ± 10	$1.9 \cdot 10^{19}$	5.2	200	3.1
	B	00:04:16	−23:17:13	−120.0	3.1 ± 0.2	1.9	37 ± 3	$8.9 \cdot 10^{18}$	2.2	210	3.1
	C	00:04:14	−23:21:13	−119.7	3.2 ± 0.9	1.9	34 ± 8	$9.1 \cdot 10^{18}$	2.0	220	3.4
	D	00:03:45	−23:30:37	−119.1	5.6 ± 1.5	3.4	17 ± 4	$7.3 \cdot 10^{18}$	1.0	690	2.5
	E	00:03:17	−23:29:43	−118.6	2.3 ± 0.3	1.4	33 ± 3	$6.9 \cdot 10^{18}$	2.0	110	2.2
QSO B1331+170 (component 1)	A	13:34:29	16:48:59	−27.8	4.1 ± 0.3	2.5	20 ± 1	$6.5 \cdot 10^{18}$	1.0	370	2.9
	B	13:34:15	16:59:22	−27.4	3.2 ± 0.2	1.9	38 ± 2	$9.2 \cdot 10^{18}$	1.9	220	2.0
	C	13:34:30	17:06:42	−27.5	5.7 ± 2.4	3.4	18 ± 4	$8.2 \cdot 10^{18}$	0.9	700	1.7
	D	13:34:22	17:07:46	−25.8	4.9 ± 1.0	3.0	25 ± 4	$9.9 \cdot 10^{18}$	1.3	520	2.2
	E	13:34:29	17:14:17	−26.6	2.5 ± 1.3	1.5	20 ± 9	$7.5 \cdot 10^{18}$	1.0	140	1.7
	F	13:34:18	17:14:03	−26.5	1.8 ± 0.5	1.1	50 ± 13	$1.2 \cdot 10^{19}$	2.6	70	1.8
QSO B1331+170 (component 2)	G	13:33:03	16:24:12	−9.8	6.2 ± 0.8	3.7	42 ± 4	$1.6 \cdot 10^{19}$	2.1	840	2.3
	H	13:33:20	16:27:30	−10.6	4.0 ± 0.3	2.4	41 ± 3	$1.1 \cdot 10^{19}$	2.1	350	2.2
	I	13:33:54	16:46:55	−10.3	3.7 ± 0.3	2.2	34 ± 2	$8.9 \cdot 10^{18}$	1.7	300	3.4
	J	13:34:17	17:04:54	−11.5	4.1 ± 0.6	2.5	48 ± 6	$1.5 \cdot 10^{19}$	2.4	360	3.9
QSO B0450−1310B	A	04:52:40	−13:15:40	−17.6	7.6 ± 0.6	4.6	36 ± 2	$2.3 \cdot 10^{19}$	2.2	1250	2.7
	B	04:52:43	−13:12:16	−16.8	6.9 ± 1.4	4.2	20 ± 3	$1.4 \cdot 10^{19}$	1.2	1050	1.7
	C	04:52:18	−13:12:58	−15.7	6.6 ± 2.0	4.0	19 ± 5	$9.9 \cdot 10^{18}$	1.2	960	1.8
	D	04:53:29	−13:07:40	−16.8	13.0 ± 3.4	7.9	9 ± 1	$9.2 \cdot 10^{18}$	0.6	3700	1.5
	E	04:53:23	−13:04:40	−18.3	7.8 ± 0.2	4.7	9 ± 1	$8.6 \cdot 10^{18}$	0.6	1300	1.4
J081331+254503	A	08:14:59	25:31:15	−20.8	6.1 ± 0.7	3.6	42 ± 4	$2.0 \cdot 10^{19}$	2.5	800	2.7
	B	08:14:51	25:35:35	−22.1	4.8 ± 0.7	2.9	17 ± 2	$6.8 \cdot 10^{18}$	1.0	490	1.9
	C	08:14:25	25:34:50	−21.2	2.4 ± 0.2	1.5	26 ± 2	$5.8 \cdot 10^{18}$	1.6	130	1.6
	D	08:13:52	25:41:19	−21.4	4.0 ± 0.2	2.4	17 ± 1	$5.8 \cdot 10^{18}$	1.0	350	2.4
	E	08:12:44	25:38:52	−23.4	3.6 ± 0.9	2.2	10 ± 2	$3.5 \cdot 10^{18}$	0.6	280	2.4
	F	08:12:25	25:43:38	−23.2	8.3 ± 2.1	5.0	7 ± 1	$4.3 \cdot 10^{18}$	0.4	1500	3.0

Fig. 5.4: VLA 21 cm column
density map (integrated over
$v_{\rm lsr} = -121 \ldots -116 \, {\rm km \, s^{-1}}$)
of the high-velocity gas in the
direction of QSO J0003−2323.
Several H I clumps with low col-
umn densities ($N_{\rm HI} \leq 1.9 \cdot 10^{19} \, {\rm cm^{-2}}$) are detected. The
beam size of $100'' \times 100''$ is in-
dicated in the lower left corner.
The contours are in steps of $\sigma_{\rm rms}$
starting at $2\sigma_{\rm rms}$ (where $\sigma_{\rm rms} = 1.6 \cdot 10^{18} \, {\rm cm^{-2}}$). The line of
sight towards QSO J0003−2323
(RA = $00^{\rm h}03^{\rm m}45^{\rm s}$, Dec =
$-23°23'55''$) is indicated in the
figure.
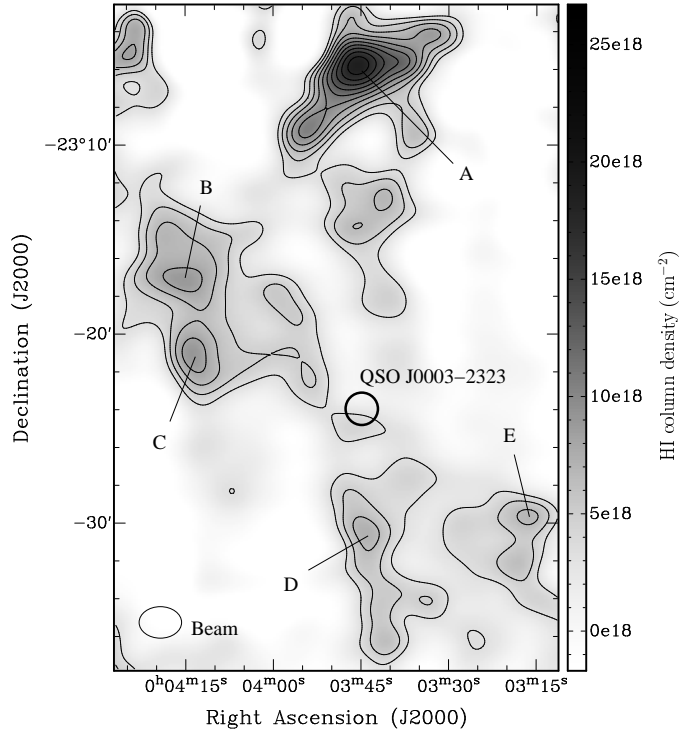
Using the reduced high-resolution data cubes (as described in Section 4.3.2) column
density maps were computed. Various physical parameters could be derived. All structures
above a threshold of $\geq 4\sigma_{\rm rms}$ were considered in our analysis. From the moment-0 maps
the peak column densities were inferred as well as the angular sizes of individual clumps
(using the Gaussian radial fit method of the *Karma* task *kvis*). The latter, however, can
only be considered as rough estimates, as the clumps are neither necessarily spherical nor
need to have Gaussian column density profiles. The spectra containing the highest total
flux were extracted and Gaussian velocity profiles were fitted. This returned peak fluxes
(which can be converted to peak brightness temperatures, $T_{\rm B}$), velocity widths (leading to
an upper temperature limit), and LSR velocities of each clump. Note, that velocity profile
widths are not only given in FWHM but are also converted to b-values to allow for better
comparison with the absorption lines. The derived physical properties of the clumps are
summarised in Table 5.2.

5.3.1   QSO J0003−2323

As mentioned in Section 5.2, we clearly ($\approx 31\sigma_{\rm rms}$) detect Ca II ($\lambda\lambda \sim 3934.77, 3969.59$)
in this system. No corresponding Na I was observed down to column density limit of
$N_{\rm NaI} \sim 3 \cdot 10^{10} \, {\rm cm^{-2}}$ (corresponding to the median of $\rm SNR_r \approx 100$ of all sight lines with
detected Na I absorption). The Ca II absorption spreads between $v_{\rm lsr} \approx -120 \ldots -80 \, {\rm km \, s^{-1}}$
having $b_{\rm CaII} \sim 6 \, {\rm km \, s^{-1}}$. A corresponding broad ($b = 19.3 \, {\rm km \, s^{-1}}$) 21 cm emission line is
found in the Effelsberg data at $v_{\rm lsr} \approx -112 \, {\rm km \, s^{-1}}$ with an H I column density of about
$\log(N_{\rm HI}/{\rm cm^{-2}}) = 19.6$. This absorbing system is kinematically compact, i.e., the multiple
components with comparable b-values are spread over less than $\approx 100 \, {\rm km \, s^{-1}}$ (Ding et al.

2005). The position as well as the velocities of the Ca II absorbing system indicate a possible association with the Magellanic System.

Figure 5.4 shows the high-resolution H I column density map of the high-velocity gas in the direction of QSO J0003−2323 observed with the VLA. The observations reveal the presence of several H I clumps. Clumps with $\geq 4\sigma_{\mathrm{rms}}$ ($\sigma_{\mathrm{rms}} = 1.1 \cdot 10^{18}\,\mathrm{cm}^{-2}$) significance level are labelled with letters A to E.

The small-scale clumps have H I peak column densities of $\sim 7\ldots 9 \cdot 10^{18}\,\mathrm{cm}^{-2}$, except for clump A with $1.9 \cdot 10^{19}\,\mathrm{cm}^{-2}$, corresponding to peak-brightness temperatures of $T_{\mathrm{B}} \sim 1\ldots 2\,\mathrm{K}$ (clump A: $5\,\mathrm{K}$). All clumps have angular diameters of $\phi < 3.5'$ (FWHM) and are mostly relatively isolated or only weakly connected to each other. However, this could be an instrumental effect as the interferometric data lack small spatial frequencies. Note also, that the clumps might not be resolved by the VLA beam, as the spatial features visible in the map match approximately the size of the beam ($100'' \times 100''$). This means that there could be even substructure within the visible cores.

The line widths are very small with $\Delta v_{\mathrm{FWHM}} \leq 3\,\mathrm{km\,s}^{-1}$, typically, implying that the absorbing gas is cool with an upper temperature limit of $T_{\mathrm{kin}} \leq 200\,\mathrm{K}$. Only clump D reveals slightly larger velocity widths, leading to an upper limit of $T_{\mathrm{kin}} \leq 700\,\mathrm{K}$. An important point is that in the H I single dish and interferometric data only one emission line was detected, while the absorption measurements reveal a multi-component structure. There also exists a slight velocity offset between the Ca II absorption components and the velocities of the H I clumps seen in emission (see Tables 5.1 and 5.2). This indicates that absorption and emission measurements trace somewhat different regions of the same overall structure. Figure 5.4 shows that the quasar sightline do not pass any of the clumps directly, but rather traces the outer boundary of clump C, which is barely detected in 21 cm emission. The detection of multiple, relatively strong Ca II absorption components towards QSO J0003−2323 thus indicates that there are additional, low-column density neutral gas structures along this sightlines that cannot be detected and/or resolved even with deep 21 cm synthesis observations. The complex spatial structure and kinematics of the outer layers of HVCs has been previously observed (Brüns 1998; Brüns et al. 2001; Ben Bekhti et al. 2006) and was also found in numerical simulations (Quilis & Moore 2001), pointing towards interactions of the clouds with the ambient medium, i.e., ram-pressure stripping causing head-tail structures.

5.3.2   QSO B1331+170

The two-component intermediate-velocity absorbers located towards QSO B1331+170 are detected in Ca II (at a 19σ level) as well as in Na I (14σ). The lines spread between $v_{\mathrm{lsr}} \approx -40\ldots 0\,\mathrm{km\,s}^{-1}$. The position as well as the velocity of the line at $v_{\mathrm{lsr}} \approx -27\,\mathrm{km\,s}^{-1}$ indicate a possible association with the intermediate-velocity complex IV-Spur.

There is a corresponding H I line at $v_{\mathrm{lsr}} \approx -9\,\mathrm{km\,s}^{-1}$ detected with the 100-m telescope at Effelsberg and possibly there is also a feature at $-27\,\mathrm{km\,s}^{-1}$, however, not detected clearly. The peak column density of the observed line is $N_{\mathrm{HI}} = 6.3 \cdot 10^{19}\,\mathrm{cm}^{-2}$.

The high-resolution WSRT 21 cm column density map (Fig. 5.5) reveals the presence of two components at $v_{\mathrm{lsr}} \sim -27\,\mathrm{km\,s}^{-1}$ (component 1) and $v_{\mathrm{lsr}} \sim -10\,\mathrm{km\,s}^{-1}$ (component 2) matching the absorption signatures in velocity. In case of component 1 six clumps were identified, labelled with letters A to F. The H I peak column densities range from about
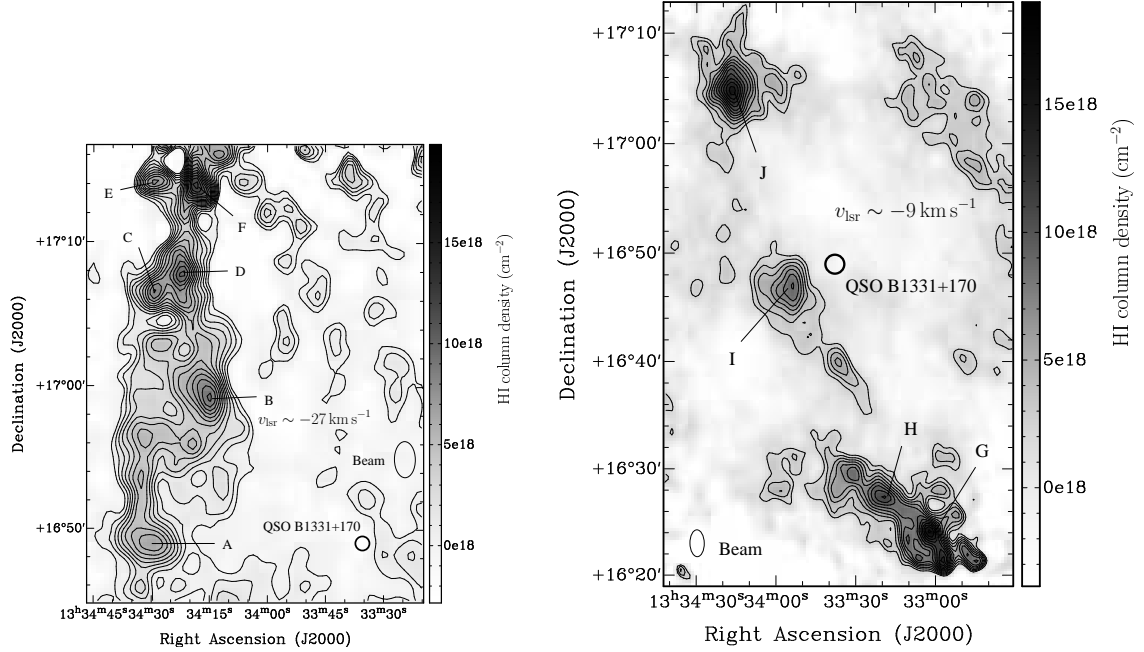
Fig. 5.5: WSRT 21 cm column density maps of the intermediate-velocity gas in the direction of QSO B1331+170. Several small H I clumps with low column densities ($N_{\mathrm{HI}} \leq 1.2 \cdot 10^{19}\,\mathrm{cm}^{-2}$) were detected at two distinct velocities of $v_{\mathrm{lsr}} \sim -27\,\mathrm{km\,s}^{-1}$ and $v_{\mathrm{lsr}} \sim -10\,\mathrm{km\,s}^{-1}$ (column densities calculated using the velocity interval $v_{\mathrm{lsr}} = -30\ldots-21\,\mathrm{km\,s}^{-1}$ and $v_{\mathrm{lsr}} = -14\ldots-1\,\mathrm{km\,s}^{-1}$, respectively). The beam size of $80'' \times 150''$ is shown in the maps. The contours start at $2\sigma_{\mathrm{rms}}$ in steps of $\sigma_{\mathrm{rms}} = 8 \cdot 10^{17}\,\mathrm{cm}^{-2}$. Note, that for the component at $v_{\mathrm{lsr}} \sim -27\,\mathrm{km\,s}^{-1}$ the line of sight towards QSO B1331+170 (RA $= 13^{\mathrm{h}}33^{\mathrm{m}}36^{\mathrm{s}}$, Dec $= 16°49'04''$) lies about $10'$ away from the nearest clump, while for the second component the line of sight is near clump I.

$\sim 6.5 \cdot 10^{18}\,\mathrm{cm}^{-2}$ to $1.2 \cdot 10^{19}\,\mathrm{cm}^{-2}$ and have peak brightness temperatures on the order of $T_{\mathrm{B}} \sim 1.0\ldots2.5\,\mathrm{K}$. Compared to the other three observed sources and component 2, this object is spatially more compact. Furthermore, the individual clumps are less isolated. The spatial separation between the position of the QSO and the emission in the high-resolution H I data is about $10'$. The angular diameters ϕ of the clumps are about $2'$. The line widths of the six clumps are in the range of $\Delta v_{\mathrm{FWHM}} \approx 2\ldots6\,\mathrm{km\,s}^{-1}$ which implies that the absorbing gas has an upper temperature limit of $T_{\mathrm{kin}}^{\mathrm{max}} \leq 700\,\mathrm{K}$. Clump F has an extraordinarily small width of only $1.8\,\mathrm{km\,s}^{-1}$ ($T_{\mathrm{kin}}^{\mathrm{max}} \leq 70\,\mathrm{K}$). Component 2 exhibits four clumps (G to J) having larger column densities of $\sim 0.9\ldots1.6 \cdot 10^{19}\,\mathrm{cm}^{-2}$ and peak brightness temperatures ($\sim 2\,\mathrm{K}$).

5.3.3   QSO B0450−1310B

Towards QSO B0450−1310 two Na I D lines at low and intermediate velocities were clearly detected at the 25σ and 11σ level, respectively. Unfortunately, no Ca II spectra are avail-
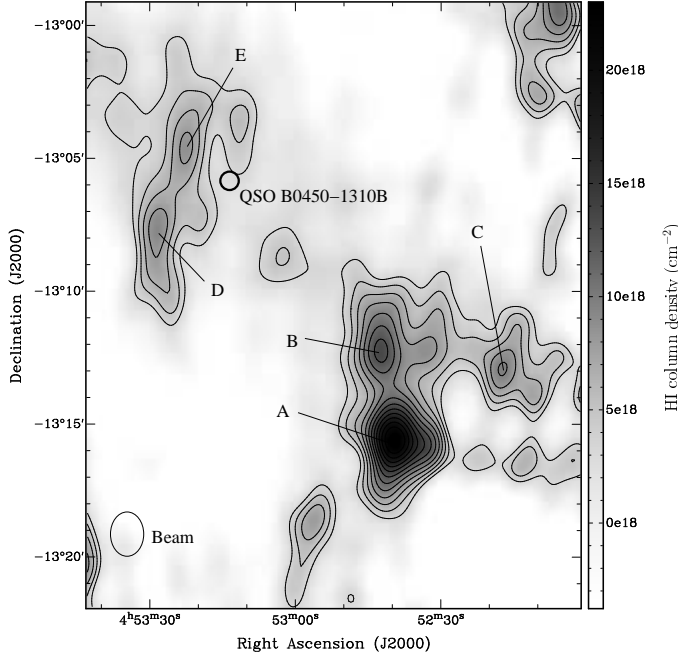
Fig. 5.6: VLA 21 cm column density map (integrated over $v_{lsr} = -22 \ldots - 9 \, \mathrm{km \, s^{-1}}$) of the intermediate-velocity gas observed in the direction of QSO B0450−1310B. H I clumps with column densities $N_{HI} \leq 2.3 \cdot 10^{19} \, \mathrm{cm^{-2}}$ are detected. The beam size of $100'' \times 100''$ is shown in the lower left corner. The contours start at $2\sigma_{rms}$ in steps of $\sigma_{rms} = 1.6 \cdot 10^{18} \, \mathrm{cm^{-2}}$. The line of sight towards QSO B0450−1310B (RA = $04^{h}53^{m}13^{s}$, Dec = $-13°05'46''$) passes the outer parts of clumps D and E.

able for this line of sight at the moment. The two absorption lines have central velocities of $v_{lsr} \approx -5$ and $-20 \, \mathrm{km \, s^{-1}}$. There is no obvious association with known IVC complexes.

For both components H I counterparts in the spectrum obtained with the 100-m telescope at Effelsberg were found, having small b_{HI}-values of 2.3 and 6.8 $\mathrm{km \, s^{-1}}$. Such narrow line widths were also measured for the Na I absorption lines ($b_{NaI} = 2, 5 \, \mathrm{km \, s^{-1}}$, which is less than the velocity resolution of the UVES instrument of about $7 \, \mathrm{km \, s^{-1}}$). The column densities of both H I systems are relatively small with $\log(N_{HI}/\mathrm{cm^{-2}}) = 19.8$ and $\log(N_{HI}/\mathrm{cm^{-2}}) = 19.3$. The Na I absorption line at $-20 \, \mathrm{km \, s^{-1}}$ reveals a larger column density and smaller width than the line at $-5 \, \mathrm{km \, s^{-1}}$. Interestingly, this is the opposite of what is observed for the H I emission.

The H I high-resolution map shown in Fig. 5.6 obtained with the VLA displays two main structures consisting of few clumps each. Clumps with a significance level of $\geq 4\sigma_{rms}$ ($\sigma_{rms} = 1.6 \cdot 10^{18} \, \mathrm{cm^{-2}}$) were labelled with letters A to E. The peak brightness temperatures are in the range of $T_B = 0.6 \ldots 2.2 \, \mathrm{K}$ and have H I column densities between $9 \cdot 10^{18} \, \mathrm{cm^{-2}}$ and $2.3 \cdot 10^{19} \, \mathrm{cm^{-2}}$. The angular diameters are very small with $\phi \approx 1.5 \ldots 2.5'$. The line widths of the clumps vary from about $\Delta v_{FWHM} = 7 \, \mathrm{km \, s^{-1}}$ up to $\Delta v_{FWHM} = 13 \, \mathrm{km \, s^{-1}}$ which corresponds to upper temperatures of $T_{kin} \approx 1000 \, \mathrm{K}$ and $T_{kin} \approx 3700 \, \mathrm{K}$, which is much higher than derived for the other sight lines. The small-scale features lie at velocities of about $v_{lsr} = -18 \, \mathrm{km \, s^{-1}}$, which is close to the higher-column density absorption line, while the diffuse gas observed with the 100-m telescope is mainly found at different velocities. This shows again, that absorption and emission measurements sample somewhat different regions and gas phases within the overall cloud complex. Possibly, the gas interacts with an ambient medium, producing colder cores containing Na I in the interface region, while the diffuse gas is dragged away by ram-pressure.
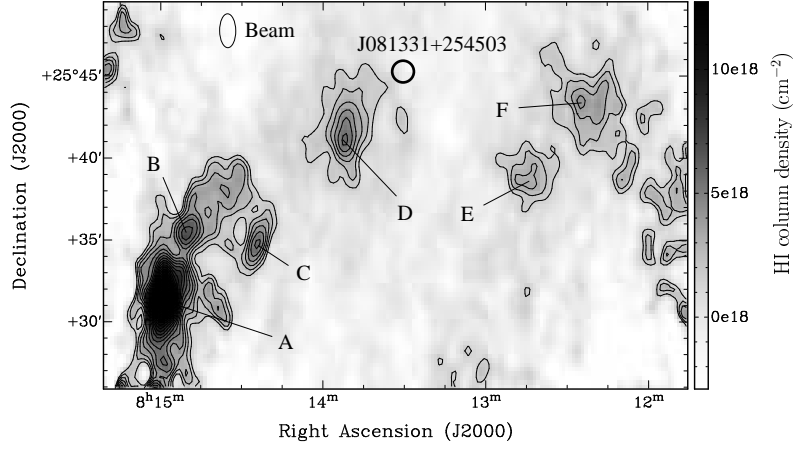
Fig. 5.7: WSRT 21 cm column density map (integrated over $v_{lsr} = -25 \ldots -18 \, \mathrm{km \, s^{-1}}$) of the intermediate-velocity gas in the direction of the QSO J081331+254503. Several small H I clumps with low column densities ($N_{HI} \leq 2 \cdot 10^{19} \, \mathrm{cm^{-2}}$) are detected. The beam size of $80'' \times 120''$ is shown in the upper left of the figure. The contours start at $2\sigma_{rms}$ in steps of $\sigma_{rms} = 8 \cdot 10^{17} \, \mathrm{cm^{-2}}$. The line of sight towards J081331+254503 (RA $= 08^h 13^m 31^s$, Dec $= 25° 45' 03''$) passes the very outer parts of clump D.

5.3.4 J081331+254503

The only single-component absorber in our sample lies towards QSO J081331+254503. A Na I D absorption line is detected at $v_{lsr} \approx -21 \, \mathrm{km \, s^{-1}}$ at the 11σ and 6σ level, respectively. There is no Ca II spectrum available for this sight line. The corresponding Effelsberg H I emission line has a b_{HI}-value of about $37.0 \, \mathrm{km \, s^{-1}}$ and a column density of $N_{HI} = 6.3 \cdot 10^{19} \, \mathrm{cm^{-2}}$. There is no association with any known IVC complex.

Figure 5.7 shows the WSRT 21 cm map of the intermediate-velocity gas in the direction of the QSO. The high resolution observations reveal the presence of six H I clumps labelled with the letters A to F. These small-scale clumps ($\phi \leq 3'$) have typical peak H I column densities in the range of $\sim 0.4 \ldots 2.0 \cdot 10^{19} \, \mathrm{cm^{-2}}$ and peak brightness temperatures of $T_B \sim 0.5 \ldots 2.5 \, \mathrm{K}$. The line widths of $\Delta v_{FWHM} \leq 8.3 \, \mathrm{km \, s^{-1}}$ lead to an upper temperature limit of $T_{kin} \leq 1500 \, \mathrm{K}$. The mean radial velocity is $v_{lsr} \approx -22 \, \mathrm{km \, s^{-1}}$ matching that of the the absorption line.

Analysis of the halo absorber sample

This chapter presents the results from a statistical study of low-column density absorbers in the Milky Way halo. The results show that in some cases the absorption is associated with known IVC or HVC H I complexes, in other cases the observed absorption has no 21 cm counterpart. The Ca II column density distribution follows a power-law $f(N) = C \left(N/\mathrm{cm}^{-2} \right)^{\beta}$ with a slope of $\beta \approx -1.6$. This is similar to the distribution found for intervening Mg II systems that trace the gaseous environment of other galaxies at low and high redshifts. The question will be discussed, whether the observed low-column density clouds possibly represent the local counterparts of Mg II systems at low and high z. This chapter has been partly adapted from the corresponding refereed journal article (Ben Bekhti et al. 2008a)

6.1   Statistical properties

We perform a statistical analysis of the 78 Ca II and 30 Na I intermediate- and high velocity absorption components detected along 53 QSO sight lines out of the total sample of 177. We compute the distribution of Ca II, Na I, and H I column densities, deviation velocities, and b-values. Correlations of these values are analysed via scatter plots and the frequency of occurrence of single and multiple absorption components is determined.

6.1.1   Column densities

Fig. 6.1 shows the Ca II and Na I column density distribution (CDD) functions, $f(N)$ for the halo absorber sample, as derived from the UVES data. Following Churchill et al. (2003), we define
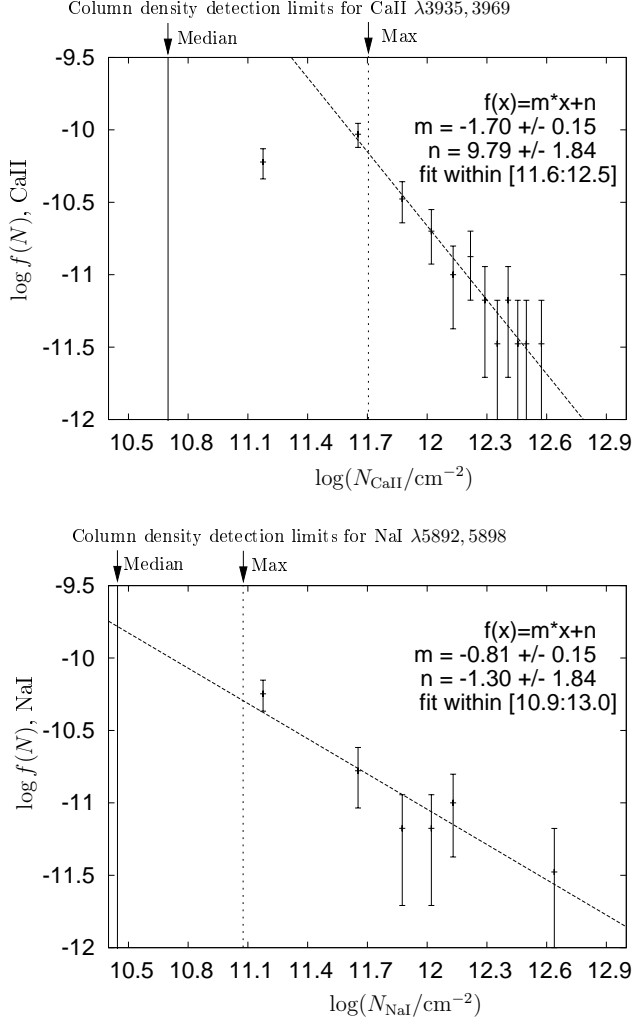
$$f(N) = \frac{m}{\Delta N},$$
(6.1)

Column density detection limits for CaII $\lambda 3935, 3969$

$f(x) = m*x + n$
$m = -1.70 +/- 0.15$
$n = 9.79 +/- 1.84$
fit within [11.6:12.5]

Column density detection limits for NaI $\lambda 5892, 5898$

$f(x) = m*x + n$
$m = -0.81 +/- 0.15$
$n = -1.30 +/- 1.84$
fit within [10.9:13.0]

Fig. 6.1: The Ca II and Na I column density distributions $f(N)$ detected with UVES. The dashed lines represent a power law fit $f(N) = C \left(N/\mathrm{cm}^{-2}\right)^{\beta}$ with $\beta = -1.7 \pm 0.2$ and $\log C = 9.8 \pm 1.8$ for Ca II, and $\beta = -0.8 \pm 0.2$ and $\log C = -1.3 \pm 1.8$ for Na I, calculated for the range of column densities from $\log(N_{\mathrm{CaII}}/\mathrm{cm}^{-2}) = 11.6 \ldots 12.5$ and $\log(N_{\mathrm{NaI}}/\mathrm{cm}^{-2}) = 10.9 \ldots 13.0$, respectively. The vertical solid lines indicate the UVES 4σ detection limits $\log(N_{\mathrm{CaII,NaI}}/\mathrm{cm}^{-2}) = 10.7, 10.4$ for the median $\mathrm{SNR_r}$ and the dotted line represent the detection limit for the worst case $\mathrm{SNR_r}$ $\log(N_{\mathrm{CaII,NaI}}^{\max}/\mathrm{cm}^{-2}) = 11.7, 11.0$.

where m is the number of absorbers in the column density range $[N, N + \Delta N]$. Integrating $f(N)$ over the observed column density range yields the total number of clouds, M, as

$$M = \int\limits_{N_{\min}}^{N_{\max}} \mathrm{d}N \, f(N) \,. \tag{6.2}$$

The distribution of the Ca II (Na II) column densities for $\log N_{\mathrm{CaII(NaI)}} > 11.6$ follows a power law $f(N) = C \left(N/\mathrm{cm}^{-2}\right)^{\beta}$ with $\beta = -1.7 \pm 0.2$; $\log C = 9.8 \pm 1.8$ for Ca II and $\beta = -0.8 \pm 0.2$; $\log C = -1.3 \pm 1.8$ for Na I. The vertical solid lines indicate the UVES 4σ detection limits $\log(N_{\mathrm{CaII}}/\mathrm{cm}^{-2}) = 10.7$ and $\log(N_{\mathrm{NaI}}/\mathrm{cm}^{-2}) = 10.4$ for the median $\mathrm{SNR_r}$ (Section 4.2) and the dotted lines represent the detection limit for the worst case $\mathrm{SNR_r}$ $\log(N_{\mathrm{CaII}}^{\max}/\mathrm{cm}^{-2}) = 11.7$ and $\log(N_{\mathrm{NaI}}^{\max}/\mathrm{cm}^{-2}) = 11.0$. Note, that only the statistical noise is taken into account for the determination of $\mathrm{SNR_r}$. The flattening of the Ca II distribution towards lower column densities is probably caused by selection effects, as it turns into effect at the column densities below $N_{\mathrm{CaII,NaI}}^{\max}$.

Fig. 6.2: The plot displays
$\log N_{\mathrm{HI}}$ (from our follow-up ob-
servations with the 100-m tele-
scope) versus $\log N_{\mathrm{CaII}}$. The
solid line shows the relation
found by Wakker & Mathis
(2000). Our data show too
much scatter to confirm their
result. However, the observed
range of column densities is
much smaller in our case (1 dex
vs. 3 dex)
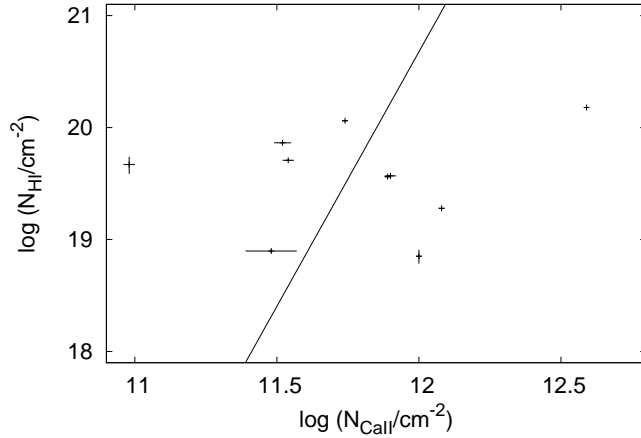
To better understand the relation between absorption-selected IVCs and HVCs from
UVES and the 21 cm halo clouds seen with the 100-m telescope, the (converted) H I column
density distributions of these data sets were compared. It is known that Ca II traces
neutral gas in the interstellar medium (ISM). However, since Ca II is not the dominant
ionisation stage of calcium in the diffuse ISM and calcium is depleted into dust grains,
the conversion between Ca II (Na I) column densities and H I column densities is afflicted
with large systematic uncertainties and thus has to be used with caution. Yet, it is an
observational fact that there exists such relations between the column densities of these
three ions in the ISM as shown by Wakker & Mathis (2000). The authors find a correlation
between the abundance A(Ca II), A(Na I), and N_{HI} from 21 cm data in the form

$$\log \left(N_{\mathrm{HI}}/\mathrm{cm}^{-2} \right) = \frac{\log \left(N_{\mathrm{CaII}}/\mathrm{cm}^{-2} \right) - 7.45}{0.22} \tag{6.3}$$

and

$$\log \left(N_{\mathrm{HI}}/\mathrm{cm}^{-2} \right) = \frac{\log \left(N_{\mathrm{NaI}}/\mathrm{cm}^{-2} \right) + 5}{0.84}. \tag{6.4}$$

Although the scatter in these relations (especially for Na I) is substantial (see Wakker
& Mathis 2000, their Fig. 1) Eq. (6.3) and (6.4) allow us to roughly estimate H I column
densities from our measured Ca II and Na I column densities and to compare the CDDs
from absorption and emission.

Figure 6.2 displays the relation between $\log N_{\mathrm{HI}}$ (from our observations with the 100-
m telescope) and $\log N_{\mathrm{CaII}}$. The solid line shows the relation found by Wakker & Mathis
(2000) (as in Eq. (6.3)). Using our data points we are not able to reproduce their fit. This
is attributed to the fact that our H I column densities cover only one order of magnitude,
while Wakker & Mathis (2000) determined the relation for a range of $\log N_{\mathrm{HI}} = 18 \ldots 21$.[1]

Note, that at the current stage it is not meaningful to calculate a relation between Na I
and H I from our 21 cm data as we have only five data points available.

Fig. 6.3 shows the converted H I column density distribution functions, $f(N)$, applying
Eq. (6.3) and (6.4) to the Ca II and Na I column densities. The dashed lines represents the

---

[1] The data from Wakker & Mathis (2000) would also not allow constraints when restricted to our column
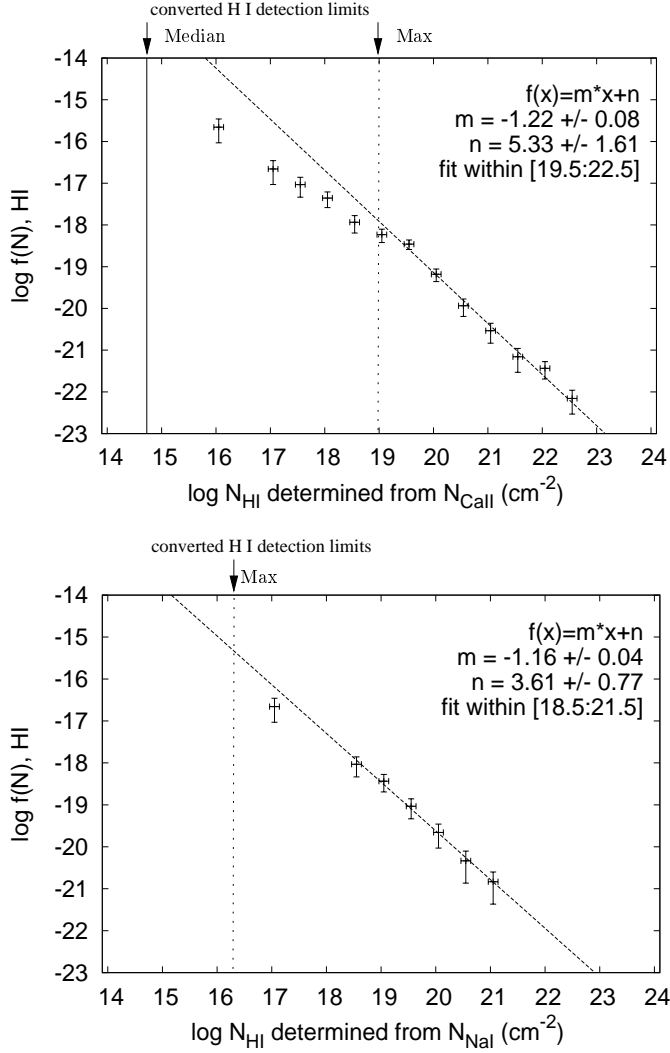density range (see Wakker & Mathis 2000, Figure 1).

Fig. 6.3: Converted H I column density distribution functions $f(N)$. The H I column densities were calculated from the Ca II (top panel) and Na I (bottom panel) column densities via the correlation between $N_{\mathrm{CaII,NaI}}$ and N_{HI} (Wakker & Mathis 2000). The dashed lines represent a power law fit $f(N) = C \left(N/\mathrm{cm}^{-2}\right)^{\beta}$ with $\beta = -1.2 \pm 0.1$ and $\log C = 5.3 \pm 1.6$ for Ca II, and $\beta = -1.2 \pm 0.04$ and $\log C = 3.6 \pm 0.8$ for Na I calculated for the range $\log(N_{\mathrm{HI}}/\mathrm{cm}^{-2}) = 19.5 \ldots 22.5$ and $\log(N_{\mathrm{HI}}/\mathrm{cm}^{-2}) = 18.5 \ldots 21.0$, respectively. The vertical lines indicate the converted 4σ level.

power law fits $f(N) = C \left(N/\mathrm{cm}^{-2}\right)^{\beta}$, with $\beta = -1.2 \pm 0.1$; $\log C = 5.3 \pm 1.6$ for Ca II and $\beta = -1.2 \pm 0.04$; $\log C = 3.6 \pm 0.8$ for Na I calculated for $\log(N_{\mathrm{HI}}/\mathrm{cm}^{-2}) = 19.5 \ldots 22.5$ and $\log(N_{\mathrm{HI}}/\mathrm{cm}^{-2}) = 18.5 \ldots 21.5$, respectively. Fig. 6.4 (top panel) shows $f(N_{\mathrm{HI}})$ resulting from our follow-up observations with the 100-m telescope. Here, we find $\beta = -0.28 \pm 0.08$; $\log C = -13.54 \pm 1.48$ for the range $\log(N_{\mathrm{HI}}/\mathrm{cm}^{-2}) = 18.5 \ldots 20$. Note, that only 15 H I emission features were detected along 27 lines of sight with the 100-m telescope. Therefore, the significance of the fit result is poor.

Apparently, the H I slopes for the two different data sets (UVES and Effelsberg) deviate from each other. There are several reasons for these differences. The used Ca II-to-H I column density conversion (Eq. (6.3)) is possibly not appropriate for our absorbers because of the uncertainties regarding ionisation, dust depletion, and beam smearing effects. The observations were accomplished with very different instruments. The 100-m telescope has a resolution of only HPBW $= 9'$ and is therefore only able to detect the diffuse, extended gas component of the absorbing systems, whereas UVES with its high (pencil beam) resolution is able to detect the compact, dense, small-scale structures within the diffuse envelope

Fig. 6.4: Top panel: The H I column density distribution $f(N_\mathrm{HI})$ resulting from the follow-up observations with the 100-m telescope. The distribution follows a power law with $\beta = -0.28 \pm 0.08$; $\log C = -13.54 \pm 1.48$ for the range $\log(N_\mathrm{HI}/\mathrm{cm}^{-2}) = 18.5\ldots20$. Note, that only a small number of absorption lines were detected with the Effelsberg telescope. Therefore, the significance of the fit result is not very high. **Bottom panel**: The H I column density distribution for the HVC sample compiled from the LAB data (Kalberla & Haud 2006). The dashed line represents a power law fit with $\beta = -2.81 \pm 0.09$; $\log C = 39.17 \pm 1.72$ calculated for the column density range $\log(N_\mathrm{HI}/\mathrm{cm}^{-2}) = 19.5$ to $\log(N_\mathrm{HI}/\mathrm{cm}^{-2}) = 21$.
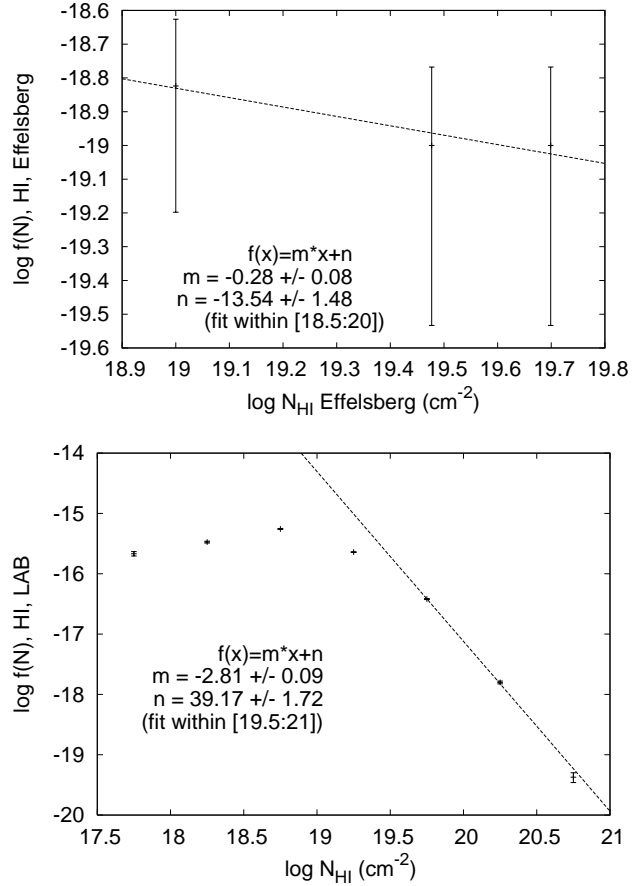
of the Ca II and Na I absorbers. Especially, small-scale, high-column density structures would get affected by beam smearing, leading to a bias. The measured column densities would be smaller than the actual ones. The slope of the column-density distribution from 21 cm data therefore is expected to steepen with stronger beam-smearing. Furthermore, as mentioned before, our H I column densities measured with the 100-m telescope cover only one order of magnitudes compared to four orders in case of Wakker & Mathis (2000). As can be seen in Fig. 6.2 the scatter is large and, hence, there is no good constraint on the correlation between Ca II and H I column densities. Note that the slope of the H I (converted from Ca II) CDD (Fig. 6.3) shows a slight flattening at low column densities $\log(N_\mathrm{HI}/\mathrm{cm}^{-2}) < 19$. This is most likely due to incompleteness caused by the detection limit of the UVES instrument. We will be able to discuss all these effects in more detail when we have a larger sample of Ca II (Na I) absorbers.

To be complete, the distribution of HVCs detected with the LAB survey (Kalberla et al. 2005b) was analysed. The bottom panel of Fig. 6.4 displays the H I column density distribution for the HVC sample compiled from the LAB data by Kalberla & Haud (2006). Here, we obtain a power-law $N_\mathrm{HI}^{-2.8}$ calculated for the range $\log(N_\mathrm{HI}/\mathrm{cm}^{-2}) = 19.5\ldots21$.
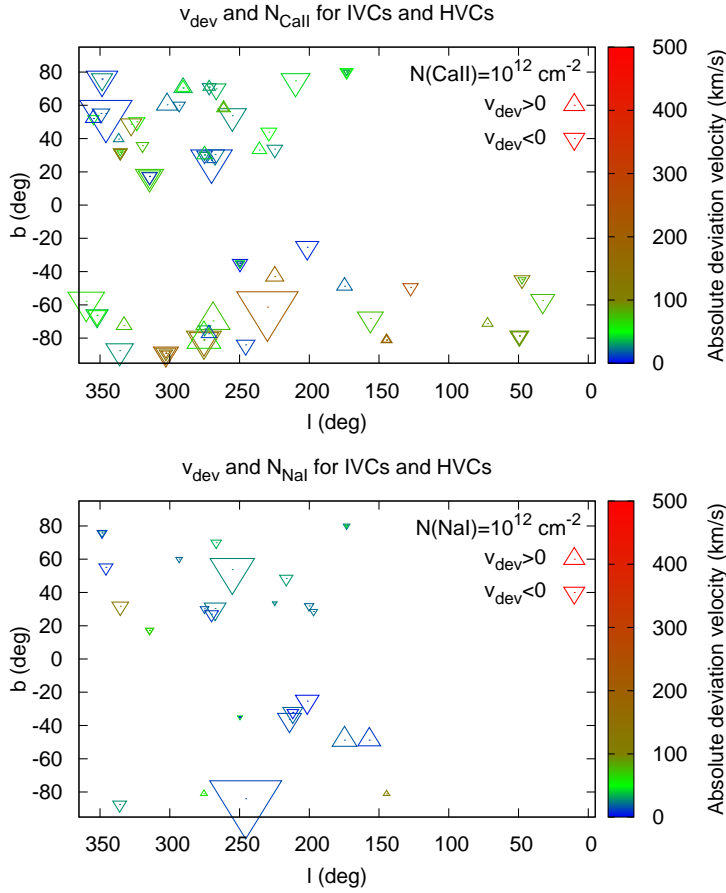
Fig. 6.5: Distribution of deviation velocities of the observed intermediate- and high-velocity absorbing systems versus Galactic longitude and latitude. The area of the triangles is proportional to the Ca II and Na I column densities observed with the UVES instrument. The legend shows the size for $N_{\mathrm{CaII,NaI}} = 1 \cdot 10^{12} \, \mathrm{cm}^{-2}$ for comparison.

6.1.2 Deviation velocities

Fig. 6.5 shows the deviation velocities (introduced in Section 5.2) of all observed intermediate- and high-velocity Ca II and Na I absorbers versus Galactic longitude l and latitude b. The sizes of the triangles in Fig. 6.5 are proportional to the Ca II and Na I column densities observed with UVES. Note that we have no Ca II and Na I UVES data for the region $b > 0°$ and $l < 200°$. Therefore, the distribution on the sky is incomplete. We expect additional HST/STIS and KECK data for Ca II, Na I and other species to cover this region of the sky.

Fig. 6.6 shows the number of sight lines with intermediate or high velocity Ca II and Na I absorption lines plotted against the deviation velocity. In the distribution of Ca II (Na I) there is an accumulation at low deviation velocities $|v_{\mathrm{dev}}| < 100 \, \mathrm{km \, s}^{-1}$ ($|v_{\mathrm{dev}}| < 50 \, \mathrm{km \, s}^{-1}$). In addition, for both ions there is a slight excess to negative v_{dev}. It is unlikely that this is due to a selection effect caused by our inhomogeneous all-sky sample, as explained in the following. In the missing northern part of the sky most of the HVCs have negative LSR velocities due to the Galactic rotation. Therefore we also expect negative deviation velocities for this region of the sky. The excess is most likely physical, e.g., it indicates clouds infalling toward the Galactic disk.

Note that there is one sight line (QSO J0103+1316) with a very high Ca II deviation velocity of about $v_{\mathrm{dev}} \approx -260 \, \mathrm{km \, s}^{-1}$. This sight line passes the region between the Anti-
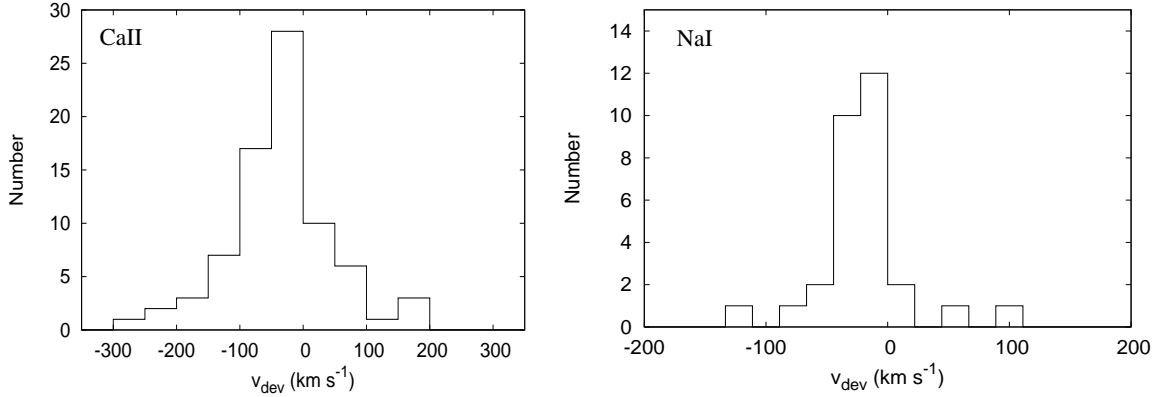
Fig. 6.6: Number of intermediate- or high-velocity Ca II and Na II absorption components versus deviation velocity.

Center Complex and the Magellanic Stream, where high negative LSR velocities are widely observed. A physical connection seems likely.

6.1.3 Doppler parameter and multi-component structure

Fig. 6.7 shows the distribution of Doppler-parameters (b-values) for the Ca II and Na I absorbers. The dashed vertical lines indicate the UVES velocity resolution of $\Delta v_{\mathrm{UVES}} \approx 7\,\mathrm{km\,s^{-1}}$. Therefore, lines with $b < 7\,\mathrm{km\,s^{-1}}$ are not resolved with the UVES instrument.[2] However, the histograms indicate that the bulk of the Ca II and Na I lines have b values smaller than $7\,\mathrm{km\,s^{-1}}$, and only a small fraction has $b > 7\,\mathrm{km\,s^{-1}}$.

Assuming thermodynamical equilibrium, we can derive an upper temperature limit (based on Eq. (A.5))

$$T < \frac{b_{\mathrm{therm}}^2 A}{f}\,. \tag{6.5}$$

In this expression b_{therm} is the Doppler parameter, A is the atomic weight and $f = 2 \cdot 10^{-6} \cdot k_{\mathrm{B}}/u$ with $k_{\mathrm{B}} = 1.38 \cdot 10^{-23}\,\mathrm{J/K}$ the Boltzmann constant and $u = 1.66 \cdot 10^{-27}\,\mathrm{kg}$ the atomic mass unit. A b-value of $7\,\mathrm{km\,s^{-1}}$ and $A_{\mathrm{CaII}} = 40$ ($A_{\mathrm{NaI}} = 23$) corresponds to an upper temperature limit of $T_{\mathrm{CaII}}^{\mathrm{max}} \approx 1.2 \cdot 10^5\,\mathrm{K}$ ($T_{\mathrm{NaI}}^{\mathrm{max}} \approx 6.8 \cdot 10^4\,\mathrm{K}$). For a mean b-value of $3\,\mathrm{km\,s^{-1}}$ one gets $T_{\mathrm{CaII}}^{\mathrm{max}} = 2.2 \cdot 10^4\,\mathrm{K}$ ($T_{\mathrm{NaI}}^{\mathrm{max}} = 1.3 \cdot 10^4\,\mathrm{K}$). Even if there is another contribution to b due to pressure or turbulence, the upper temperature limit holds, because then b_{therm} would be even lower, and, hence, the corresponding T_{max}.

However, since Ca II and Na I absorption traces mostly neutral gas it is clear that the b-value is dominated by turbulent gas motions (which does not necessarily mean that the turbulent motions are large) rather than by the temperature of the gas (otherwise higher ionisation states would be observed). This is also indicated by the much lower

---

[2] Since the b-value follows from the COG and is dependent on W_λ, only the integral value of a line profile is of interest. Even, if a line is not completely resolved, the integral is invariant, as the measured spectrum is a convolution of the true spectrum with the instrumental response function.
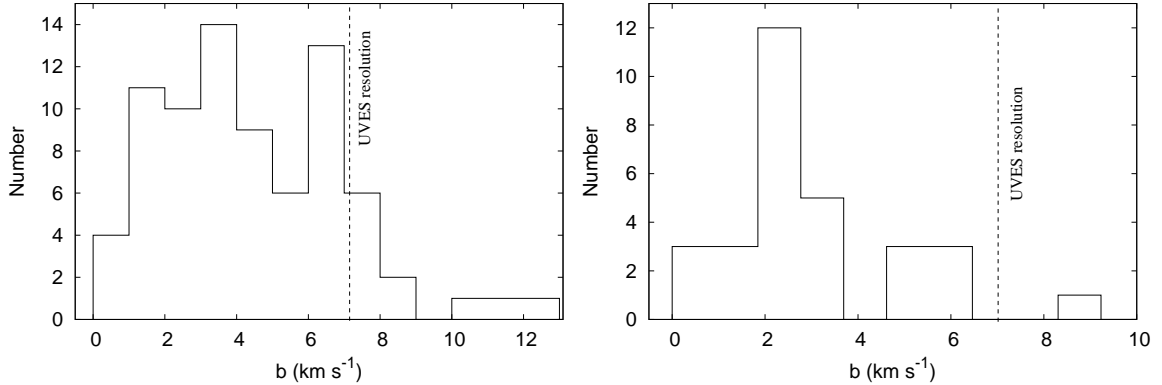
Fig. 6.7: Number of intermediate- and high-velocity Ca II and Na I absorption lines versus b-values. The dashed vertical line indicates the UVES velocity resolution of $\Delta v_{\mathrm{UVES}} \approx 7 \ \mathrm{km \, s^{-1}}$.

upper temperature limits estimated from the measured 21 cm line widths of typically $10^2 \ldots 10^3 \, \mathrm{K}$ (see Chapter 5, Table 5.2). The fact that most of the Ca II and Na II lines have b values of $< 7 \, \mathrm{km \, s^{-1}}$ indicates that turbulence and bulk motions in the gas are relatively small.

Sembach et al. (2003) used FUSE data to study highly ionised (O VI) high-velocity absorbing systems along sight lines through the Galactic halo in the directions of 100 extragalactic objects. Compared to our absorbers these highly ionised systems have much higher b-values in the range of $16 \ldots 72 \, \mathrm{km \, s^{-1}}$, suggesting that either high-ion absorbers exist in much more extended regions (kpc-scales) than the Ca II absorbers and/or that they have higher temperatures.

Systems that show Na I absorption possibly are even more confined, as the presence of Na I requires relatively high gas densities ($n_{\mathrm{H}} > 0.1 \, \mathrm{cm^{-3}}$) to achieve a detectable level of neutral sodium, which has an ionisation potential of $< 10 \, \mathrm{eV}$. For a constant thermal gas pressure, on the other hand, high densities imply low temperatures of the gas.

This idea is supported by high-resolution ($R \sim 68000$) observations by Sembach et al. (1993) and Sembach & Danks (1994). They obtained a sample of spectra in the direction of 55 stars at distances above 2 kpc, containing 231 Na I and 312 Ca II components. Some of the absorbers show a two-component temperature distribution of cold ($\sim 100 \, \mathrm{K}$) and warm (~ 1000 to $5000 \, \mathrm{K}$) gas likely presenting diffuse clouds and intercloud medium. Ca II traces both media, while Na I was detected preferentially in the denser clouds (Sembach et al. 1993; Sembach & Danks 1994).

Note that the presence of relatively cold, sub-pc and AU-scale structures in the Galactic halo gas has been proven by other observations. One sight line in the direction of PKS 1448−232 with distinct Ca II and Na I absorption and corresponding H I emission lines was recently observed by Richter et al. (2005) with the VLA. At an angular resolution of about $2'$ (HPBW) they detected several cold ($T < 1000 \, \mathrm{K}$) clumps of neutral gas with fairly low peak column densities of $N_{\mathrm{HI}} \approx 7 \cdot 10^{18} \, \mathrm{cm^{-2}}$. In addition, ultraviolet measurements of molecular hydrogen in Galactic extraplanar clouds have shown that small, dense gaseous clumps at sub-pc scale are widespread in the lower halo, in particular in the intermediate-velocity clouds (Richter et al. 1999, 2003a,b). A detailed discussion of

Table 6.1: Number of IVC and HVC Ca II and Na I absorption components observed
with UVES and their absolute and percental values. The total number of sight lines
which show Ca II (Na I) absorption lines is 47 (25). The last two columns show the
data of strong Mg II absorbers with redshifts $1.0 \leq z \leq 2.7$ analysed by Prochter
et al. (2006, see Section 6.3.3 for a detailed description) for comparison. Their total
number of absorbers is 26.

Number of components	Sight lines with Ca II absorption	Sight lines with Na II absorption	Sight lines with Mg II absorption
1	29 (62%)	20 (80%)	5 (19%)
2	9 (19%)	5 (20%)	13 (50%)
3	4 (9%)	0 (0%)	2 (8%)
4	5 (11%)	0 (0%)	3 (12%)
5	0 (0%)	0 (0%)	1 (4%)
6	0 (0%)	0 (0%)	0 (0%)
7	0 (0%)	0 (0%)	1 (4%)

small-scale structures observed in the direction of four sight lines from our data sample is
presented in Chapter 7.

To check whether a single or a multi-component absorption structure is typical for the
extraplanar Ca II (Na II) absorbers, Table 6.1 shows the number of IVC and HVC Ca II
(Na I) absorption components. Obviously, Ca II (Na I) absorption systems with a single
or a double absorption-component structure are more common with 81% (100%) than
systems with more than two absorption components with 19% (0%). This result indicates
that either there is not much substructure in the Ca II and Na I absorbers or that only the
densest clumps can be detected. However, from the 21-cm high-resolution data we know
that there is a lot of substructure in the H I.

6.1.4   Correlation between b, v_{dev}, and $N_{\mathbf{Ca}\text{II},\mathbf{Na}\text{I}}$

In this Section possible correlations between b-values, deviation velocities, and Ca II and
Na I column densities will be analysed.

Figure 6.8 shows a scatter plot of $b_{\mathrm{CaII,NaI}}$ versus $\log N_{\mathrm{CaII}}$. We find a weak correlation

$$b_{\mathrm{CaII}} \left[\mathrm{km\,s^{-1}}\right] = (2.4 \pm 0.5) \cdot \log\left(N_{\mathrm{CaII}}\left[\mathrm{cm^{-2}}\right]\right) + (-25 \pm 6), \qquad (6.6)$$

indicating that b_{CaII} increases with increasing $\log N_{\mathrm{CaII}}$. The b_{NaI} vs. $\log N_{\mathrm{NaI}}$ fit leads to
the opposite result, b_{NaI} decreases with increasing $\log N_{\mathrm{NaI}}$. The correlation is

$$b_{\mathrm{NaI}} \left[\mathrm{km\,s^{-1}}\right] = (-0.9 \pm 0.5) \cdot \log\left(N_{\mathrm{NaI}}\left[\mathrm{cm^{-2}}\right]\right) + (13 \pm 6). \qquad (6.7)$$

However, these results have to be handled with care, because of the low number statistics
and the very large scatter of the data points. Especially, in case of Na I the correlation is
not very well constrained.

The different behavior of b as a function of $\log N$ for both species can be explained
using Eq. (2.44). Under the assumption of ionisation balance in the absorbing systems, the
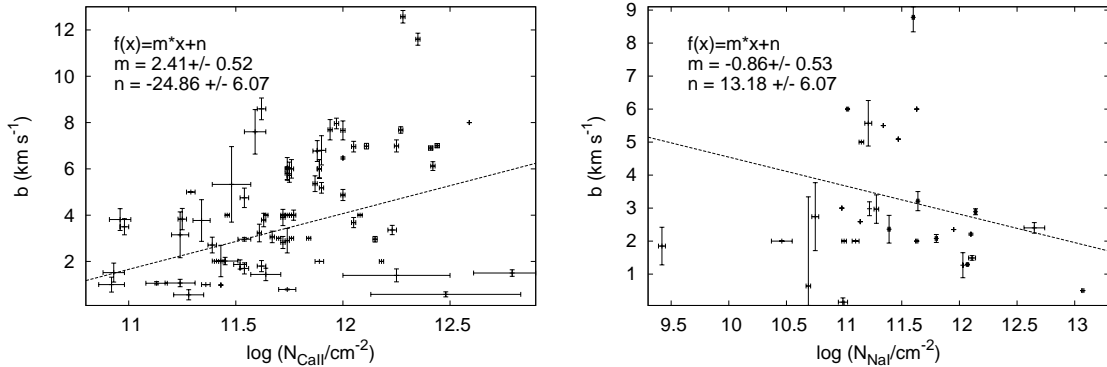
Fig. 6.8: b_{CaII} (b_{NaI}) values as a function of $\log N_{\text{CaII}}$ ($\log N_{\text{NaI}}$). There is a correlation between b_{CaII} and $\log N_{\text{CaII}}$ with $b_{\text{CaII}} = (2.4 \pm 0.5) \cdot \log N_{\text{CaII}} + (-25 \pm 6)$. The three outlier data points in the Ca II plot were not included for the fit. The results for b_{NaI} versus $\log N_{\text{NaI}}$ have to be handled with care, because of the low number statistic and the large scatter of the different data points.

fraction of ionised to atomic gas depends weakly on the temperature ($\sim \sqrt{T_{\text{e}}}$) and anti-linear on the electron density n_{e}^{-1}. Thus, in order to observe the neutral atomic sodium, having a low ionisation potential and being easily ionised, the density must be high and the temperature low to provide the necessary recombination rate. Additionally, for an ideal gas in thermodynamic equilibrium follows $n \sim T^{-1}$, meaning that high-density gas has lower temperatures (and thus likely small b-values) and vice versa. The same mechanism explains the calcium observations, with the only difference that here the ionised part is measured, hence, the fraction of ionized to atomic calcium is expected to increase with increasing temperature (b-value) and decreasing density.

In Fig. 6.9 the $b_{\text{CaII,NaI}}$-values are plotted as a function of the deviation velocities. There is visibly no dependence of b-values on v_{dev}.

Figure 6.10 displays $\log N_{\text{CaII}}$ and $\log N_{\text{NaI}}$ versus the v_{dev}. Again, there is no correlation between Ca II (Na I) column densities and deviation velocities. Note, that drawing any conclusions for sodium is difficult due to the low number statistics.

6.2   Dust depletion

As mentioned in Section 6.1.1, the determination of calcium and sodium abundances and the conversion between N_{CaII}, N_{NaI}, and N_{HI} is afflicted with large systematic uncertainties due to the unknown amount of calcium/sodium being depleted onto dust grains, and ionisation effects.

The column density ratio $N_{\text{NaI}}/N_{\text{CaII}}$ has often been used as an indicator of the degree of dust depletion (Welsh et al. 1990; Bertin et al. 1993; Crawford et al. 2002; Kondo et al. 2006) because sodium is hardly depleted on grains while calcium can be heavily depleted (Savage & Sembach 1996). Table 6.2 lists the ratio $\log N_{\text{NaI}}/N_{\text{CaII}}$ for all absorption components where both elements were observed. The ratios are rather low with $N_{\text{NaI}}/N_{\text{CaII}} < 15$. Values of $N_{\text{NaI}}/N_{\text{CaII}} \leq 20$ are expected in diffuse, warm ($T \approx 10^3\,\text{K}$)
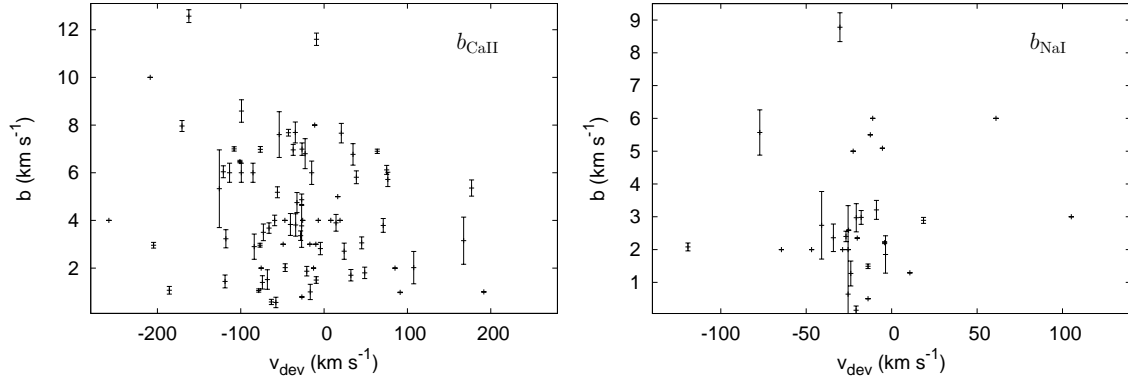
Fig. 6.9: b_{CaII} (b_{NaI}) versus the deviation velocity v_{dev}. There is no dependence of b-values on the deviation velocity.
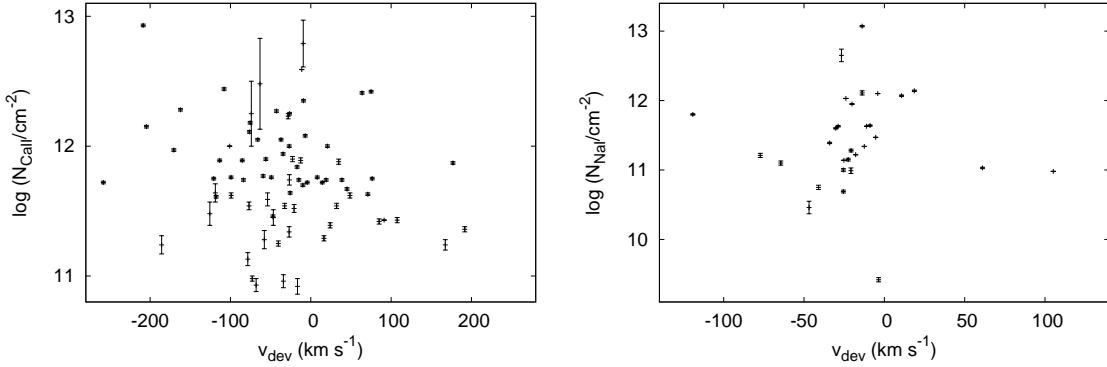

Fig. 6.10: Column densities N_{CaII} and N_{NaI} plotted as a function of deviation velocities. There is no obvious correlation between the two parameters.

low-density ($n_{\mathrm{H}} \approx 10\,\mathrm{cm}^{-3}$) regions like the ISM and the IGM where much of the calcium remains in the gas phase (Crawford et al. 2002). In contrast, values of $N_{\mathrm{NaI}}/N_{\mathrm{CaII}} \geq 100$ are expected in cold ($T \approx 30\,\mathrm{K}$), dense ($n_{\mathrm{H}} \geq 10^3\,\mathrm{cm}^{-3}$) regions like molecular clouds. Crawford et al. (2002) comment that even when the same velocity component is identified in both species, Na I and Ca II are not necessarily located in the same region of an observed cloud. As a result, the determined values represent just an average over the absorption path through the cloud.

To compare the derived $N_{\mathrm{NaI}}/N_{\mathrm{CaII}}$ ratios for the low-column density halo absorbers with absorbers located in different environments, we display in Fig. 6.11 our results in a $\log(N_{\mathrm{NaI}}/N_{\mathrm{CaII}})$ versus $\log N_{\mathrm{NaI}}$ plot created by Kondo et al. (2006). The red symbols show DLA data ($1.06 \lesssim z \lesssim 1.18$) obtained by Kondo et al. (2006) with the near-infrared instrument IRCS (Infrared Camera and Spectrograph) installed at the Subaru Telescope. Black and blue symbols show the data for the Milky Way (Vallerga et al. 1993)[3] and the

---

[3] The authors observed Ca II and Na I absorbers towards 46 early type stars in the local ISM with distances between $d = 20 \ldots 500\,\mathrm{pc}$ with the Coudé Echelle Spectrograph (CES).

Table 6.2: Listed are $\log N_{\mathrm{NaI}}$, $\log N_{\mathrm{CaII}}$, and the ratio $N_{\mathrm{NaI}}/N_{\mathrm{CaII}}$ for all absorption components where both elements were observed.

QSO	$\log N_{\mathrm{NaI}}$ [N in cm^{-2}]	$\log N_{\mathrm{CaII}}$ [N in cm^{-2}]	$\log(N_{\mathrm{NaI}}/N_{\mathrm{CaII}})$
QSO B1448−232	11.80 ± 0.01	11.64 ± 0.07	0.16 ± 0.07
QSO B0109−353	11.03 ± 0.01	12.41 ± 0.01	-1.38 ± 0.01
J120550+020131	13.05 ± 0.03	12.24 ± 0.14	0.81 ± 0.14
	11.73 ± 0.01	12.29 ± 0.04	-0.56 ± 0.04
QSO J1232−0224	11.36 ± 0.02	11.94 ± 0.01	-0.58 ± 0.02
	11.72 ± 0.02	11.77 ± 0.02	-0.05 ± 0.03
	10.99 ± 0.04	11.52 ± 0.03	-0.53 ± 0.05
QSO B0515−4414	10.75 ± 0.03	11.25 ± 0.02	-0.50 ± 0.04
	9.42 ± 0.03	11.72 ± 0.01	-2.30 ± 0.04
QSO B1212+3326	10.46 ± 0.09	11.45 ± 0.06	-0.99 ± 0.11
	11.00 ± 0.02	11.59 ± 0.03	-0.59 ± 0.04
QSO B1420+0011	11.64 ± 0.01	12.79 ± 0.02	-1.15 ± 0.02
QSO B1104+0104	12.65 ± 0.09	12.25 ± 0.01	0.40 ± 0.09
QSO J0256+0110	12.14 ± 0.01	11.74 ± 0.01	0.40 ± 0.01
QSO J0911+0551	10.69 ± 0.02	11.74 ± 0.04	-1.05 ± 0.05
LBQS 0042−2930	11.63 ± 0.01	12.23 ± 0.02	-0.60 ± 0.02
J135256−441240	11.21 ± 0.03	12.05 ± 0.01	-0.84 ± 0.03
	11.10 ± 0.03	12.25 ± 0.03	-1.15 ± 0.04
J120342+102831	11.39 ± 0.01	11.94 ± 0.01	-0.55 ± 0.01
QSO B1036−2257	12.03 ± 0.01	11.97 ± 0.01	0.06 ± 0.01
QSO B0458−0203	12.10 ± 0.01	12.08 ± 0.01	0.02 ± 0.01
QSO J1039−2719	11.63 ± 0.01	12.59 ± 0.01	-0.96 ± 0.01
QSO B1101−26	11.22 ± 0.01	11.74 ± 0.01	-0.52 ± 0.01
QSO B1331+170	11.14 ± 0.01	12.00 ± 0.01	-0.86 ± 0.01
QSO B1331+170	11.34 ± 0.01	12.35 ± 0.01	-1.01 ± 0.01
QSO B2343+125	11.44 ± 0.01	12.12 ± 0.01	-0.68 ± 0.01
	11.73 ± 0.01	12.18 ± 0.01	-0.45 ± 0.01
	12.13 ± 0.01	11.92 ± 0.01	0.21 ± 0.01
QSO B0112−30	13.07 ± 0.01	11.89 ± 0.02	1.18 ± 0.02
QSO J0105−1846	10.98 ± 0.01	11.43 ± 0.02	-0.45 ± 0.02

Large Magellanic Cloud (LMC) (Vladilo et al. 1993)[4]. The green symbols display our absorption components where both elements were observed. The green line represents a power-law fit through our data

$$\log(N_{\mathrm{NaI}}/N_{\mathrm{CaII}}) = (0.89 \pm 0.10) \cdot \log N_{\mathrm{NaI}} + (-10.75 \pm 1.20). \tag{6.8}$$

We find that the $N_{\mathrm{NaI}}/N_{\mathrm{CaII}}$ ratio in our absorbing systems are systematically smaller than those in the DLAs, the LMC and the Milky Way. Kondo et al. (2006) argued that dust depletion is generally smaller in a lower metallicity environment. However, as discussed in Section 6.1.4 low-density regions have a higher fraction of ionised-to-neutral gas. The observed ratio is most likely due to the fact that the densities in the DLAs, LMC, and MW are generally much higher than in our sources. Furthermore, the results indicate that most of the Ca II and Na II is in the gas phase rather than depleted onto dust grains.

---

[4] The authors used the CES instrument to observe Ca II and Na I absorbers towards 16 stars in a $30' \times 30'$ region of the LMC centered around SN 1987A.
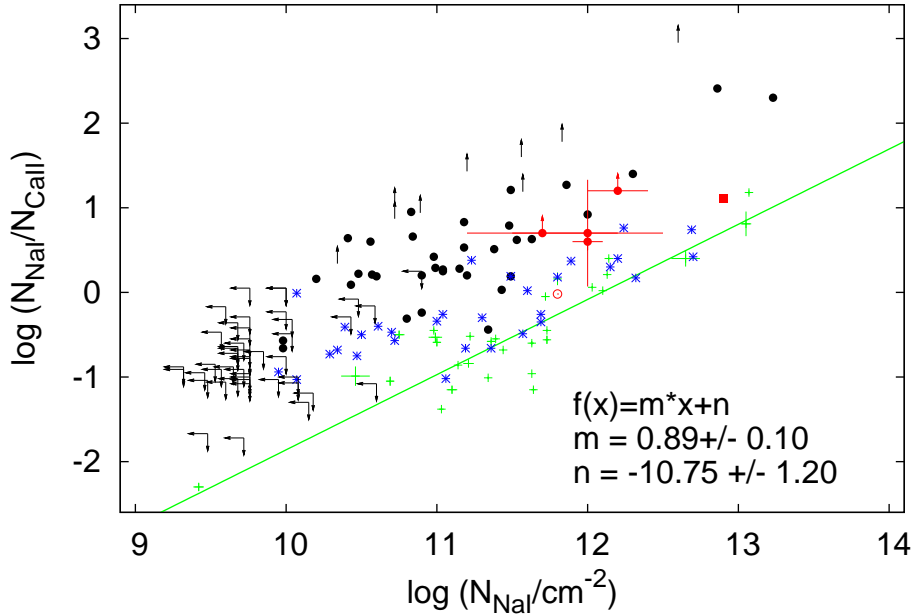
Fig. 6.11: Relation of $\log N_{\mathrm{NaI}}$ and $\log(N_{\mathrm{NaI}}/N_{\mathrm{CaII}})$. The red symbols show the DLA data $(1.06 \lesssim z \lesssim 1.18)$ from Kondo et al. (2006). Black and blue symbols show the data for the Ca II and Na I absorbers in Milky Way (Vallerga et al. 1993) and the LMC (Vladilo et al. 1993). The three datasets were kindly provided by Sohei Kondo. The green symbols show our absorption components where both elements were observed. The dashed green line represents a power-law fit $f(N) = C\left(N/\mathrm{cm}^{-2}\right)^{\beta}$ with $\beta = 0.89 \pm 0.10$ and $\log C = -10.75 \pm 1.20$.

6.3 Physical properties and origin of the absorbers

The fact that among 177 random lines of sight through the halo we have detected 47 Ca II and 25 Na I extraplanar absorption systems shows that the Milky Way halo contains a large number of neutral and weakly ionised gas structures.

6.3.1 Area filling factors

The area filling factor, A, is defined as the fraction of sight lines which shows intermediate- and high-velocity Ca II (Na I) absorption or H I emission compared to the total number of observed sight lines. From the sample we obtain a total Ca II (Na I) area filling factor of about $32 \pm 5\%$ ($16 \pm 3\%$) if no distinction between HVC and IVC gas is made. In 14 of the 25 sightlines observed with the 100-m Effelsberg telescope H I was detected. However, this does not allow us to compute an (unbiased) area filling factor, since the 21 cm measurements were not performed along random directions but only for lines of sight were metal absorption was already detected.

In Table 6.3 the detection rates are listed separately for HVC and IVC gas using the deviation velocity of the clouds as a separation criterion (see Section 5.2). The resulting

Table 6.3: The table lists the total detection rates from our sample for Ca II, Na I, and H I. Furthermore, conditional detection rates $(X \,|\, Y)$, were computed, i.e., the probability to find the species X if Y is detected.

	Ca II	Na I	H I	Ca II or Na I	(Na I|Ca II)	(H I|Ca II)	(H I|Na I)
HVC	24/146	3/155	2/13	24/177	3/21	2/13	1/2
IVC	28/146	22/155	12/16	34/177	16/28	9/13	11/11
Total	47/146	25/155	14/25	53/177	21/45	10/23	13/16

area filling factors for Ca II (Na I) are $16 \pm 3\%$ and $19 \pm 4\%$ ($2 \pm 1\%$ and $14 \pm 3\%$) for HVC and IVC gas, respectively. Furthermore, the conditional detection rates for H I, (H I | Ca II) and (H I | Na I), were calculated, i.e. the number of sightlines showing H I when Ca II (Na I) was previously measured. It is remarkable that Ca II is present almost evenly in HVC and IVC H I emission, while Na I and H I are only rarely detected in HVCs but more often in IVCs. That is possibly because closer to the disk the gas pressure is higher, hence the density and N_{NaI} must be increased. In most cases where Na I was measured, the follow-up 21 cm observations confirmed the absorbers. Obviously, Ca II is a much more sensitive tracer for low-column density material than Na I or H I. This is also confirmed by the conditional detection rate, (Na I | Ca II), where in 3 of 21 (16 of 28) cases HVC (IVC) gas was found in Na I when previously detected in Ca II.

One can roughly estimate the H I area filling factor by computing $A_{\mathrm{HI}} = A_X \cdot (\mathrm{H\,I}\,|\,X)$ under the assumption that the relative abundance is constant for all clouds (which is certainly not exactly true). Using the Ca II data, we obtain $A_{\mathrm{HI}} \sim 3\%$ (HVC) and $A_{\mathrm{HI}} \sim 13\%$ (IVC), while Na I leads to $A_{\mathrm{HI}} \sim 1\%$ (HVC) and $A_{\mathrm{HI}} \sim 14\%$ (IVC). Both species lead to a remarkably consistent estimate considering the rather low number counts for absorbers with high-velocities.

Wakker (2004) found for randomly chosen directions on the sky that the probability to find high-velocity gas with $N_{\mathrm{HI}} > 2 \cdot 10^{18}\,\mathrm{cm}^{-2}$ is about 15% (for $N_{\mathrm{HI}} > 7 \cdot 10^{17}\,\mathrm{cm}^{-2}$ the rate increases to 30%). Our data show a much smaller H I area filling factor, however, our H I column density limit is only about $\log(N_{\mathrm{HI}}/\mathrm{cm}^{-2}) \approx 19$.

6.3.2   Association with known IVC or HVC complexes

The spatial positions of 32 of the intermediate- and high-velocity Ca II and Na I absorbers as well as their velocities indicate a possible association with known large and extended IVC or HVC complexes (see Table 5.1). Since the distances to the absorbing systems are not known, position and velocity are the only indicators for possible associations with IVC or HVC complexes.

We find that 13 absorbing systems are likely associated with the Magellanic Stream (MS). In all 13 cases the sight lines pass only through the outer regions of the MS. In the case of QSO J0139−0824 and QSO J0105−1846 it is not clear whether the absorbers are parts of the MS or the Anti-Center shell (AC shell) because they are located between both complexes (see Fig. 5.1). Only for the sight line towards QSO J0003−2323 we carried out H I observations with the 100-m telescope at Effelsberg and found corresponding emission.

Another eleven systems are probably associated with the intermediate-velocity Spur (IV-Spur). The sight lines towards QSO J1211+1030 and QSO B1331+170 pass the inner, denser part of the IV-Spur whereas the other nine sight lines are located in the outer, clumpy and filamentary structures of the complex. For two of these sight lines we have additional H I observations but only in one case (QSO J1211+1030) we found a corresponding emission line.

The position and the velocity of the absorbing system towards QSO B1212+3326 indicate that this system is possibly part of the inner region of the intermediate-velocity Arch (IV-Arch). For this sightline we have obtained additional H I data. Only one component has a counterpart in H I.

One absorption component in the direction of QSO J1039−2719 is most likely associated with the HVC complex WD. We re-observed this sight line with the 100-m telescope at Effelsberg but we detected no corresponding H I emission line.

The sight line towards QSO B0458−0203 passes the very outer regions of the Anti-Center shell. The H I data reveal a corresponding emission line.

The velocity and the coordinates of the absorption component with the high positive LSR velocity in the direction of QSO B1101−26 is possibly associated with the Leading Arm (LA) of the Magellanic System. The sight line passes the outer region of the LA. The Effelsberg data show no corresponding H I emission line.

The absorbing system towards QSO 1448−232 is possibly associated with the HVC complex L (Richter et al. 2005).

The two absorbing components in the direction of QSO J2155−0922 are possibly part of the HVC complex GCN. The Effelsberg data show no corresponding H I emission line.

6.3.3   Comparison with Mg II systems and CDD functions

The low-column density intermediate- and high-velocity Ca II and Na I absorbers have a substantial area filling factor. If these absorbers represent a typical phenomenon of spiral galaxies like our Milky Way or M31 and if they were located in the halo of these galaxies, there is a possibility that they produce H I Lyman-Limit and Mg II absorption along sight lines which pass through their halo. There are two different populations of Mg II absorbers, the weak ($W_{\lambda 2796} \leq 0.3$ Å) and the strong ($W_{\lambda 2796} > 0.3$ Å) Mg II systems. While the weak Mg II absorbers are thought to be located within impact parameters of $D = 35 \ldots 100 \, h^{-1}$kpc (see Richter et al. 2008, and references therein), the strong Mg II systems are most likely located at $D \leq 40 \, h^{-1}$kpc (e.g., Petitjean & Bergeron 1990; Charlton & Churchill 1998; Ding et al. 2003b) or even in the discs of galaxies (Damped Lyman Alpha systems, DLAs, Rao et al. 2006). Many of the strong Mg II systems possibly represent the analogues of IVCs or HVCs (e.g., Savage et al. 2000). In fact, the properties of the high-velocity Ca II and Na I absorption lines resemble those of the strong Mg II absorption line systems observed in the circumgalactic environment of other galaxies (Ding et al. 2003a; Bouché et al. 2006; Prochter et al. 2006). The high-velocity Ca II and Na I absorbers thus may possibly represent the Galactic counterparts of strong Mg II systems as observed at low redshifts.

In Section 6.1 we have shown that absorption systems at intermediate and high velocities with a single or a double absorption component structure are more common than systems with more than two absorption components. Prochter et al. (2006) analysed

51 quasar spectra measured with the High Resolution Echelle Spectrograph (HIRES) to search for strong Mg II absorption systems. They found 26 strong Mg II ($W_\lambda > 1.0$ Å) absorber along 22 lines of sight with redshifts in the range of $1.0 \lesssim z \lesssim 2.7$. Their component analysis shows that there is a tendency for two or more Mg II absorption lines (Table 6.1). The more complex absorption structure for Mg II systems can be explained geometrically. While for other galaxies the impact parameter of the line of sight can vary, the sightlines through the Milky Way halo are always radial.

Important information about the distribution of neutral and weakly ionised extraplanar gas in the Milky Way is provided by CDD functions $f(N)$ of Ca II, Na I, and H I that we have derived in Section 6.1. We can compare the properties of these distribution functions with results from QSO absorption-line studies and extragalactic H I surveys. The slope of the Ca II CDD of Milky Way absorbers turns out to be $\beta = -1.7 \pm 0.2$ for the column density range of $\log(N_{\text{CaII}}/\text{cm}^{-2}) = 11.6 \dots 12.5$. This is nearly the same slope as derived for strong Mg II absorbers at intermediate redshifts ($z = 0.4 - 1.2$) of $\beta = -1.59 \pm 0.05$, as presented by Churchill et al. (2003). The similarity of the slopes suggests that (despite somewhat different ionisation and dust-depletion properties) Ca II and strong Mg II absorbers probe similar gaseous structures that are located in the environment of galaxies.

Concerning neutral hydrogen, Petitjean et al. (1993) have investigated the H I CDD function of intergalactic QSO absorption line systems at high redshift (mean redshift of $z \approx 2.8$) with the help of high spectral resolution data. Their H I data span a range from $\log(N_{\text{HI}}/\text{cm}^{-2}) = 12 \dots 22$ (see Section 1.4.2, Fig.1.7). They could show that a single power law with a slope of $\beta = -1.49$ provides only a poor fit to the data. Dividing the sample into two subsamples (lower and higher than 10^{16} cm^{-2}), they found a slope of $\beta = -1.83$ for the $\log(N_{\text{HI}}/\text{cm}^{-2}) < 16$ sample and $\beta = -1.32$ for the $\log(N_{\text{HI}}/\text{cm}^{-2}) > 16$ sample. Petitjean et al. (1993) point out that the overall H I distribution is more complex than had been thought and that even two power laws not perfectly describe the data. In a later study, Kim et al. (2002) showed that the slope of the H I CDD indeed varies between ~ -1.4 and ~ -2.0, depending on the mean absorber redshift and the column-density interval used. Unfortunately, very little is known about the H I absorber distribution in the range interesting for us, $\log(N_{\text{HI}}/\text{cm}^{-2}) = 15 \dots 19$ and at $z = 0$ due to the near impossibility to obtain low-redshift QSO data in the uv band. Lehner et al. (2007) have analysed the column-density distribution of intervening low-column density intergalactic H I absorbers at low redshift ($z < 0.4$) using HST/STIS data. They considered two different populations of H I absorbers, the narrow Lyα absorbers (NLAs) and the broad Lyα absorbers (BLAs). They find that for their NLAs the column density distribution $f(N_{\text{HI}})$ in the range $13.2 < \log(N_{\text{HI}}/\text{cm}^{-2}) < 16.5$ follows a power law with slope $\beta = -1.76$. The slope changes to $\beta = -1.84$ if they use the entire sample (NLAs and BLAs) for the fit in the same column density range.

Although there are substantial uncertainties in the conversion of Ca II and Na I into H I as discussed above, it is interesting that the slopes of the H I column density distributions of $\beta = -1.2 \pm 0.1$, as indirectly derived from our Ca II and Na I data for the $\log(N_{\text{HI}}/\text{cm}^{-2})$ range between 19 and 22 (18.5 and 21.5), is in general agreement with the statistics of low- and high-redshift QSO absorption line data. This implies that a significant fraction of high-column density ($\log(N_{\text{HI}}/\text{cm}^{-2}) > 16$) intervening QSO absorbers are closely related to their host galaxies in a way similar as the intermediate- and high-velocity Ca II and Na I

absorbers are connected to the Milky Way. It appears that the column density distribution of extraplanar neutral gas structures (i.e., HVCs and their extragalactic analogues) is roughly universal at low and high redshift. This underlines the overall importance of the processes that lead to the circulation of neutral gas in the environment of galaxies (e.g., fountain flows, gas accretion, tidal interactions) for the evolution of galaxies.

Bouché et al. (2006) present three hypotheses which could describe the Mg II absorbers and favor the idea that Mg II absorbers are produced in Galactic outflows driven by supernovae (Bond et al. 2001; Ellison et al. 2003). To find out whether our observed Ca II and Na I absorbers are the analogues of the strong Mg II absorbers or whether they are parts of the large IVC and HVC complexes, metallicity measurements are required. Metal abundances of some HVCs have been determined by absorption line measurements along several lines of sight (Wakker 2001; Richter et al. 2001a; Tripp et al. 2003). The results show that the metallicities are typically below solar, but larger than one would expect for primordial gas. The conclusion is that the high-velocity gas has already been processed in a Galactic environment. Rigby et al. (2002) and Charlton et al. (2003) showed that the strong Mg II absorbers have metallicities (e.g., Mg II, Si II, C II) greater than 10% solar or even as high as the solar value. If we assume that the Ca II and Na I absorbers are the analogues of the strong Mg II absorbers and arise in Galactic outflows, their metallicities should be roughly solar. Metallicities significantly below solar would be consistent with the assumption that these absorbers represent metal-poor gas falling onto the Milky Way (Wakker et al. 1999). In this case it is obvious that such an accretion of metal-poor gas could influence the chemical evolution of the Milky Way (de Boer 2004). An important task for future studies thus is to derive an estimate of the metal-content of the Ca II and Na I absorbers.

Analysis of the H I high-resolution 21 cm data

This chapter discusses the results of the follow-up H I *synthesis measurements carried out with the WSRT and the VLA. Four sight lines were observed (QSO B1331+170, QSO J0003−2323, QSO B0450−1310 and J081331+254503) showing prominent* Ca II *and* Na I *absorption and* H I *emission; see Section 5.3. The direction as well as the velocities of two absorbing systems indicate a possible association with the Magellanic Stream and IV Spur, respectively. Assuming the known distances of the corresponding complexes, distance-dependent physical parameters of the gas can be estimated.*

The high resolution observations also allow us (in principle) to calculate metal abundances of the clouds. Unfortunately, the sight lines towards three of the sources pass only the very outer envelope of the clumps so that a determination of Ca II *or* Na I *abundances turns out to be impossible. Parts of this chapter have been adapted from (Ben Bekhti et al. 2008b, submitted)*

7.1 Determination of physical parameters

The coordinates as well as the radial velocities of QSO B1331+170 (component 1, $v_{\mathrm{LSR}} \approx -27\,\mathrm{km\,s^{-1}}$) and QSO J0003−2323 ($v_{\mathrm{LSR}} \approx -119\,\mathrm{km\,s^{-1}}$) suggest that the low-column density gas is part of the IVC complex IV Spur and the Magellanic System (MS), respectively. An association of the gas along the other two sight lines with a known IVC or HVC complex is not confirmed. The clumps have an angular diameter of $\lesssim 3.5'$. Assuming they are spherical and located at the same distance of about 1 kpc as the IV Spur (Wakker 2001) and about 50 kpc as the MS (Yoshizawa & Noguchi 2003), the clumps have diameters of about $0.5 \ldots 0.8\,\mathrm{pc}$ (QSO B1331+170) and $30 \ldots 50\,\mathrm{pc}$ (QSO J0003−2323), respectively. Considering these assumptions, we are able to estimate physical parameters such as mass and pressure of the gas.

The total H I mass as a function of distance d is given by Eq. (2.34) using the angular size of a resolution element (pixel) of the N_{HI} column density map of $16''$ (for QSO B1331+170) and $6''$ (for QSO J0003−2323). The mean density of each clump can than be determined with the help of Eq. (2.35).

Table 7.1: Physical parameters of the small-scale structures that we observed in the directions of QSO B1331+170 with the WSRT and QSO J0003−2323 with the VLA. For the determination of the parameters we assume a spherical symmetry for the clumps and a distance of 1 kpc (IV-spur) and 50 kpc (MS), respectively.

QSO	clump	r	M_{HI}	n_{HI}	$\frac{P_{\max}}{\mathrm{k_B}}$
		[pc]	[$M_\odot$]	[cm^{-3}]	[cm^{-3} K]
QSO J0003−2323	A	45	470	0.14	27
	B	45	280	0.06	14
	C	49	160	0.06	14
	D	36	150	0.06	45
	E	32	160	0.07	8
QSO B1331+170	A	0.8	0.05	2.5	900
	B	0.6	0.07	5.0	1100
	C	0.5	0.02	5.5	3800
	D	0.6	0.06	5.0	2600
	E	0.5	0.02	4.8	700
	F	0.5	0.05	7.9	600

Using the upper limit for the kinetic temperature, the derived particle density, and assuming an ideal gas, one gets Eq. (2.36) for the upper thermal pressure limit. Inserting Eq. (2.35) into Eq. (2.36) provides

$$\frac{P_{\max}}{\mathrm{k_B}} = \frac{N_{\mathrm{HI}}}{d \tan \phi} T_{\max} = \frac{\sin b}{z} \frac{N_{\mathrm{HI}}}{\tan \phi} T_{\max} \qquad (7.1)$$

as a function of the (unknown) distance of the cloud, or as a function of height, z, above the Galactic plane (considering the latitude, b). However, the uncertainty in the determination of the angular sizes of the clumps is problematic, as it could have a large impact on the result if the clumps were not resolved.

Table 7.1 shows the estimated physical parameters for the clumps observed in the direction of QSO B1331+170 and QSO J0003−2323 for the assumed distances.

The small line widths of all the clumps, especially the ones of QSO J0003−2323 (Section 5.3.1 and Table 5.2), indicate that the absorbing gas is cold with upper temperature limits of $T_{\mathrm{kin}} \approx 100$ K for the clumps having the most narrow line widths of $\Delta v_{\mathrm{FWHM}} \approx 2$ km s^{-1} and $T_{\mathrm{kin}} \approx 3700$ K for the structures with the broadest values of $\Delta v_{\mathrm{FWHM}} \approx 13$ km s^{-1}. The temperatures could be even lower because effects like turbulent motions within the gas likely contribute to the observed line width. The temperatures and projected sizes of the clumps detected in the direction of QSO B1331+170 and QSO J0003−2323 show that the clumps are compact and cold, rather than diffuse and extended.

Due to the fact that the smallest spatial structures observed are of similar size as the synthesised WSRT and VLA beam it is possible that the observed clumps are not resolved and contain structures on even smaller scales. This fact raises the question whether IVCs and HVCs and their small-scale structures have fractal properties as discussed in Vogelaar & Wakker (1994). However, the answer to this question requires many more observations at different spatial resolutions.

We compared the determined upper pressure limits for our high-velocity absorbing system in the direction of QSO J0003$-$2323 and QSO B1331+170 with the results of Wolfire et al. (1995) which are based on model calculations of a parcel of gas in the Milky Way potential, considering the Galactic cosmic-ray flux, the Galactic and extragalactic radiation field, and the photoelectric heating from dust grains and polycyclic aromatic hydrocarbons (PAHs). The authors calculated for various scenarios the pressure limits $P_{\mathrm{min,max}}$ (in thermal equilibrium) for HVCs in the Galactic halo as a function of height z above the Galactic plane. They find that stable two-phase gas exists only within a narrow pressure range. Note, that both absorbing systems lie near the Galactic poles, hence the distance roughly equals the Galactic height. We adopt two of the scenarios, the Galactic fountain model (using a metallicity of $Z = 1$ and a dust-to-gas-ratio of $D/G = 1$) for the IVCs and the stripped LMC model ($Z = 0.4$, $D/G = 2$) for the HVC. Additionally, we use their modeled thermal halo pressure for gas temperatures of $T_6 = 1$ and $T_6 = 2$ ($T_6 \equiv T/10^6$ K). Note, that a Galactic fountain ($Z = 1$, $D/G = 0.3$) would lead to a valid pressure range even lower than for $D/G = 1$. Under the assumption that the observed HVC in the direction of QSO J0003$-$2323 is associated with the Magellanic Stream, we compare the derived upper pressure limit of $(P/\mathrm{k_B})_{\mathrm{upper}}$ with the pressure range of $P/\mathrm{k_B} \approx 20 \dots 180\,\mathrm{cm^{-3}\,K}$ for the HVC gas stripped from the MS (calculated using $Z \approx 0.4$ and $D/G = 0.2$; Wolfire et al. 1995).

The observed pressure values of clump A and D are relatively low but consistent with the Wolfire models. The other structures reveal pressures not compatible with the models. However, as discussed before, the physical size of the clumps might be overestimated (if unresolved). In that case, the derived upper pressure limit would be underestimated.

For QSO B1331+170 the simulated pressure range of $P/\mathrm{k_B} \approx 150 \dots 650\,\mathrm{cm^{-3}\,K}$ (assuming a Galactic fountain origin, a metallicity of about 1.0 solar and a dust-to-gas ratio of $D/G = 0.3$) or $P/\mathrm{k_B} \approx 650 \dots 3500\,\mathrm{cm^{-3}\,K}$ (metallicity of about 1.0 and a dust-to-gas ratio of $D/G = 1.0$) is consistent with our observations. For the two other sightlines towards QSO B0450$-$1310 and J081331+254503, the lack of distance information for the halo clouds in these directions unfortunately impedes a similar pressure analysis.

7.2   Pressure limits

Using Eq. (7.1) allows us to investigate the possible parameter space for the pressure values of the clouds and to compare it to the H I pressure expected in the vicinity of the Milky Way based on a model fitted to the LAB data (Kalberla 2003; Kalberla et al. 2007) and the models of Wolfire et al. (1995). We introduced this method in Ben Bekhti et al. (2006) in order to estimate lower distance limits for two HVCs.

Figure 7.1 shows the results for one exemplary clump of each of the objects with unknown distance (QSO B0450+1310B, QSO B1331+170 component 2, and J081331+254503), as well as for the two sources with known distance (QSO J0003$-$2323 and QSO B1331+170 component 1) to allow for a consistency check. The solid blue lines display the pressure of the clumps as a function of the distance and the associated errors, respectively. The solid green curve shows the pressure variation of the Milky Way gas derived from the model by Kalberla et al. (2007). The red and magenta curves displays the results of Wolfire et al. (1995)
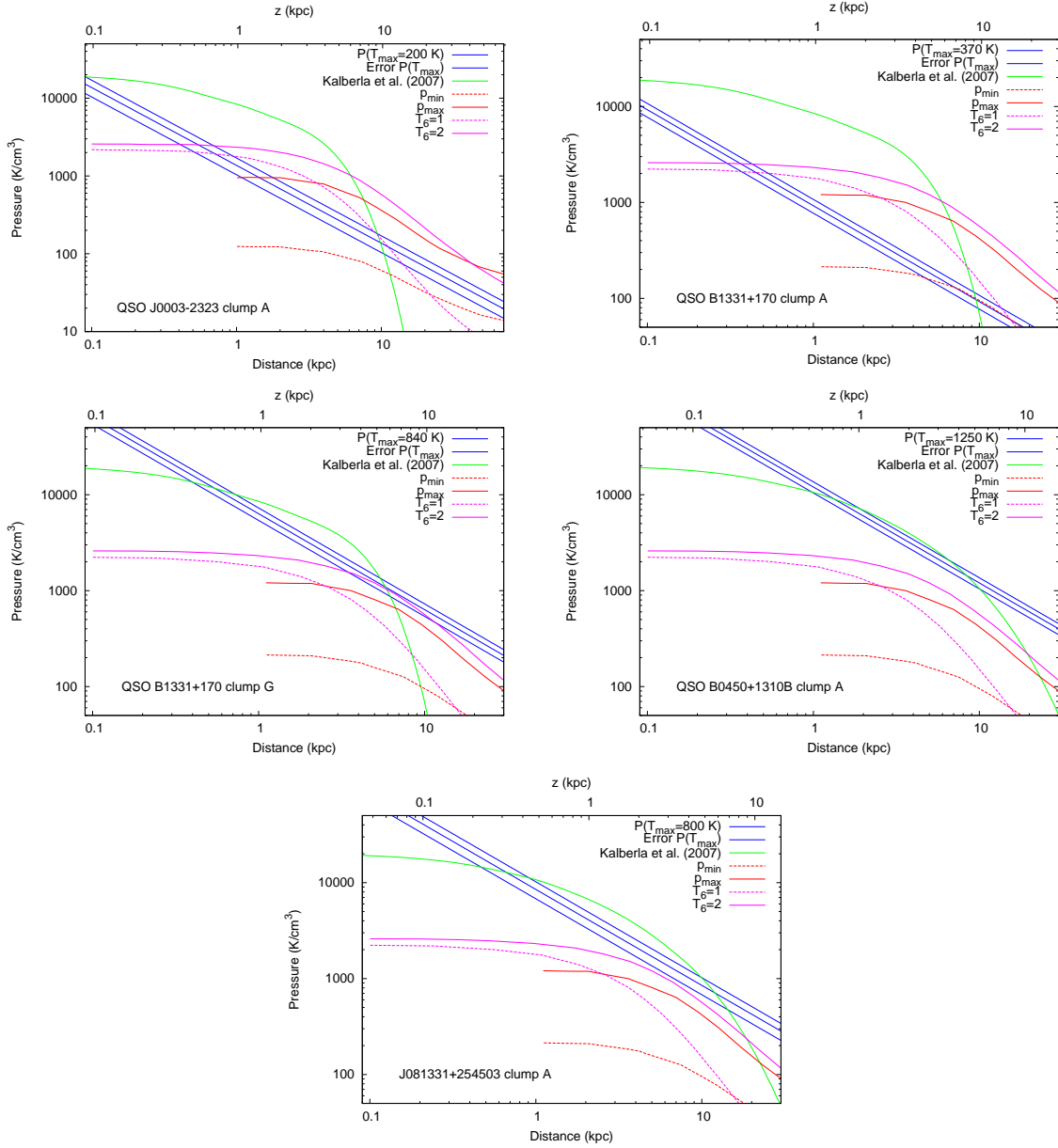
Fig. 7.1: Pressure variation according to Eq. (7.1) as a function of distance, d, (blue curves) or height above the Galactic plane, z, for one exemplary clump of each object. For consistency check, also the two sources with known distances (top row, QSO J0003−2323 and QSO B1331+170 component 1; compare Table 7.1) are shown. The pressure variation as derived from a model developed by Kalberla et al. (2007) for each of the sightlines was calculated (green curves). Furthermore, the resulting pressure limits $P_{\mathrm{min,max}}$ (red curves) computed by Wolfire et al. (1995), as well as thermal pressures of the halo gas at two different temperatures (magenta curves) $T_6 = 1$ and $T_6 = 2$ (T_6 is the temperature normalised to 10^6 K) are visualised. For the intermediate-velocity clouds the curves are based on a Galactic-fountain model ($Z = 1$, $D/G = 1$), for the HVC QSO J0003−2323 (upper left panel) the stripped LMC model ($Z = 0.4$, $D/G = 2$) was used. A Galactic-fountain model with $Z = 1$, and $D/G = 0.3$ leads to even lower pressure limits.

An important aspect is that for scale-heights $z \lesssim 4 \dots 5\,\mathrm{kpc}$ the Milky Way model of Kalberla, which is fitted to observational data, leads to much higher pressures than the models of Wolfire et al. (1995). For larger z there is a stronger turnover observed, than predicted by the Wolfire models.

The upper pressure limits calculated for the individual clumps have to be treated carefully. If the clumps are in pressure equilibrium (which not needs to be true) with the surrounding medium the true pressure must be lower than the plotted curve (blue solid line) tracing P_{max}. However, the uncertainties are rather large, for the reasons which were already discussed in Ben Bekhti et al. (2006). Most problematic is likely the uncertainty in the determination of the angular sizes of the clumps, which could have a great impact if the clumps are not resolved. For that reason, only (individual) clumps having a rather large column density and angular size were considered. Furthermore, it is unclear how reasonable the assumption of pressure equilibrium is, because the gas is likely turbulent (especially in the vicinity of the "boiling" Galactic disk) and possibly subject to interaction processes, as described in Section 5.3. Also, the models make global (or large-scale) predictions and lack the power to provide meaningful data on small fluctuations, which most likely can not be neglected in a Galactic fountain scenario.

In both cases with known distances, the results are consistent with the simulated pressure limits (Wolfire et al. 1995), but only in the case of QSO J0003$-$2323 (50 kpc) the MW model fits, whereas for QSO B1331+170 (1 kpc) the predicted pressure (at a distance of 1 kpc) is much higher than our upper pressure limit. This inconsistency is not surprising, since especially in the case of IVC and HVC complexes (and for large distances) the MW model is likely to fail. For the remaining three objects, the comparison with the Kalberla model leads to either upper distance limits of about $z \leq 0.3 \dots 0.6\,\mathrm{kpc}$ or lower distance limits of $z \geq 4 \dots 6\,\mathrm{kpc}$, the latter being unlikely for IVCs. Again, our data are consistent with the model of Wolfire et al. (1995).

In summary, we conclude that this method of obtaining distance-brackets is rather uncertain. Not only the error in the derived pressure limit leads to a wide range of allowed distances, but it is also questionable whether the global MW models can be applied to sources like the MS or IV Spur, not being explicitly described. Here, local physical properties might differ substantially.

7.3 Abundances

To better understand the nature and the origin of these low-column density, small-scale clumps in the halo and their relation to large IVC and HVC complexes it would be very helpful to constrain the chemical composition of these objects. Our optical observations provide column density information for the two species Ca II and Na I, while the 21 cm observations give N_{HI}.

However, there are a number of systematic effects that inhibit a reliable estimate for the absolute calcium and sodium abundances in the clouds. In diffuse neutral gas, Ca II and Na I are not the dominant ionization stages of these elements because of their low ionization potentials compared to hydrogen, and both elements usually are depleted into dust grains. Therefore, the measured Ca II and Na I column densities in the halo absorbers are not expected to be representative for the total calcium and sodium abundances in the

gas. Another severe systematic problem for determining the absolute abundances of these elements comes from the comparison of the absorption-line data with the H I 21 cm emission measurements. The beam sizes of the WSRT and the VLA still are very large compared to the pencil beam of the absorption measurements. Therefore, the H I column density values are just averages over a larger area on the sky, and the values at the quasar positions are not accurately known. In all our cases the quasar sightlines are located outside or at the edge of the H I clumps. There, one might just observe the Gaussian decline of the point spread function in a region where there might not even be any detectable signal at all. Also, the radial velocities and the component structure of the absorption lines are different than those seen in 21 cm emission. This points towards small-scale structure in the gas that is not detected and/or resolved in the beam-smeared H I data.

Despite all these substantial uncertainties, ionic gas phase abundances, A, for Ca II and Na I (relative to H I) have been published for a large number of Milky Way disk and halo absorbers (e.g., Wakker 2001; Wakker & Mathis 2000), implying that for each ion A scales with H I in a different manner and with different scatter. As an example, we compare the ionic gas phase abundance of Na in the halo absorber towards QSO B0450+1310B with these previous observations. We choose the QSO B0450+1310B sightlines as it passes relatively close to one of the H I clumps seen in the high- resolution 21 cm data (Fig. 3). For the halo absorber towards QSO B0450+1310B a column density of $N_{\mathrm{HI}} = 2.8 \cdot 10^{18}\,\mathrm{cm}^{-2}$ was measured by the VLA ($N_{\mathrm{NaI}} = 10^{12}\,\mathrm{cm}^{-2}$). The associated Na I abundance is $A_{\mathrm{NaI}} \approx 360 \cdot 10^{-9}$, which is about seven times larger than Na I abundances previously measured in diffuse halo clouds ($A_{\mathrm{NaI}} \leq 50 \cdot 10^{-9}$, $A_{\mathrm{CaII}} = 3 \ldots 350 \cdot 10^{-9}$; Wakker 2001; Wakker & Mathis 2000). However, Wakker (2001) points out that the Ca II (Na I) abundance in IVC and HVC gas varies by a factor of 2–5 (10) within and by a factor 5–10 (100) between clouds. Since all our clouds generally are of low column density, this substantial scatter makes it impossible to draw any meaningful conclusions about the Ca and Na abundances and overall metallicities of the absorbers based solely on our Ca II and Na I measurements.

A much more reliable method to study the metal content of weak halo absorbers is the analysis of UV and FUV spectra, as obtained with FUSE and HST/STIS. Richter et al. (2008) recently have studied the metallicities in seven low-column density high-velocity absorbers by comparing the column densities of O I with that of H I. The ratio O I/H I is a very robust measure for the metallicity of the gas, as it does not depend on ionization effects and dust depletion. In this study, N_{HI} has been derived from FUV absorption data by fitting the higher Lyman series lines in absorption against the quasars, but not from beam-smeared 21 cm emission observations. The UV measurements indicate that similar as for the large IVC and HVC complexes, low-column density halo clouds span an abundance range between 0.1 and 1.0 solar, suggesting multiple (Galactic and extragalactic) origins for the absorbers. Also relative abundance ratios (e.g., Fe/Si) have been used to constrain the enrichment history of these clouds (see Richter et al. 2008). Interestingly, the simultaneous detection of Ca II and other low ions such as O I, Si II, and Fe II in two high-velocity systems towards PHL 1811 implies that the high-velocity Ca II absorbers considered in this study and the weak UV absorption systems studied by Richter et al. (2008) trace the same population of low-column density halo clouds. Therefore, one would expect that metal-content and origin of the high-velocity Ca II systems are manifold as well.

Summary and outlook

Analysing the distribution and physical properties of low-column density gaseous structures in the extended halos of galaxies is essential for the understanding of the formation and evolution of structure in the Universe. Multiwavelength observations of extraplanar gas around galaxies are an important method for the study of the various processes that trigger the matter circulation between galaxies and their intergalactic medium. Metal-poor gaseous matter from the IGM is accreted onto the Galactic disc and metal-enriched gas from stellar winds and/or supernovae flows out into the halo and enriches the extraplanar gas with heavy elements. Furthermore, interaction and merging of galaxies feed the halos with large amounts of interstellar material. The latter processes indicate the on-going evolution of galaxies, which are of special interest for the theory of the hierarchical structure formation in the Universe.

An important laboratory to study all these processes in great detail is the Milky Way. Space- and Earth based spectroscopic instruments working in the UV, FUV, and optical regimes together with radio telescope measurements allow us to study the gaseous structures in the halo of the Milky Way in absorption and emission and to place the extraplanar gaseous environment of the Milky Way into a cosmological context.

8.1   Results from the UVES and Effelsberg data

The analysis in this thesis represents the first approach to systematically study the distribution and physical properties of the low-column density halo absorbers based on an absorption selected data base. We have analysed optical and ultraviolet absorption spectra of Ca II, Na I, and 21 cm emission of H I of extraplanar gas towards 177 extragalactic lines of sight using archival data from VLT/UVES as well as 21 cm data from the Effelsberg telescope and the LAB survey. Optical and ultraviolet Ca II (Na I) absorption of intermediate- and high-velocity gas was detected along 47 (25) lines of sight in 78 (30) individual absorption components. For 27 of these sight lines we have carried out H I 21 cm observations with the Effelsberg 100-m telescope to search for corresponding emission lines.

The large data samples make it possible, for the first time, to statistically analyse in detail the cloud distribution and properties. The analysis shows that about 50% of the Ca II (Na I) absorption systems are associated with known HVC or IVC complexes (many are related to the Magellanic Stream). The other 50% have no obvious association with an HVC or IVC complex. This could indicate that the H I column densities of these structures are below the detection limit of single-dish 21 cm observations. We find that the neutral and partly ionised low-column density structures have a substantial area filling factor of about 30%, implying that these structures are numerous in the Milky Way halo. This suggest that low-column density neutral gas structures may provide the missing link between the inner gaseous halo of the Milky Way and the surrounding intergalactic medium in the Local Group.

The Ca II column density distribution in the observed N_{CaII} regime follows a power-law $f(N) = C \left(N/\mathrm{cm}^{-2}\right)^{\beta}$ with a slope of $\beta \approx -1.6$. This distribution is similar to the distribution found for intervening Mg II systems that trace the circumgalactic gaseous environment of other galaxies at low and high redshift. Of particular interest is the fact that, after having transformed the observed Ca II and Na I column densities into H I column densities, we find that the gas in the halo follows the universal power-law of the column density distribution of QSO absorption line systems. This implies that a significant fraction of intervening QSO absorbers are closely related to galaxies like the intermediate- and high-velocity Ca II and Na I absorbers are connected to the Milky Way. It appears that the column density distribution of extraplanar neutral gas structures (i.e., HVCs and their extragalactic analogues) is roughly universal at low and high redshift.

The column density ratio $N_{\mathrm{NaI}}/N_{\mathrm{CaII}}$ was used as an indicator for the degree of dust depletion. The overall small values of $N_{\mathrm{NaI}}/N_{\mathrm{CaII}} < 15$ are expected in warm, diffuse ($T \approx 10^3\,\mathrm{K}$) low-density ($n_{\mathrm{H}} \approx 10\,\mathrm{cm}^{-3}$) regions like the ISM and the IGM where much of the calcium and sodium is in the gas phase. The distribution of $\log(N_{\mathrm{NaI}}/N_{\mathrm{CaII}})$ versus $\log N_{\mathrm{NaI}}$ follows a power law with $\beta \approx 0.9$. We compared the $N_{\mathrm{NaI}}/N_{\mathrm{CaII}}$ ratios of our low-column density absorbers with the data of Kondo et al. (2006) for DLAs ($1.06 \lesssim z \lesssim 1.18$), and the Ca II (Na I) absorbers in the LMC and the Milky Way. We found that the ratios of our absorbers are systematically smaller than those of Kondo et al. (2006). The results indicate that the densities in our Ca II and Na I absorber are much smaller than in DLAs, the LMC, and the Milky Way.

Most of the gaseous halo structures are characterised by single (55%)- or double (23%)-component absorption, indicating that either there is not much substructure in the clouds or that only the densest clumps can be detected. Since we observed substructure in the Ca II and Na I absorbers with the VLA and the WSRT the last assumption is more realistic. The components have b-values of $< 7\,\mathrm{km\,s^{-1}}$, corresponding to an upper temperature limit of $T_{\mathrm{CaII}} \approx 1.2 \cdot 10^5\,\mathrm{K}$ ($T_{\mathrm{NaI}} \approx 6.8 \cdot 10^4\,\mathrm{K}$). These small b-values indicate that turbulences and bulk motions in the gas are relatively small. Nevertheless, since Ca II and Na I traces mostly neutral or weakly ionised gas, the b-values are dominated by turbulent gas motions or pressure rather than by the temperature of the gas. The lower temperature limits measured from the 21-cm line widths of $10^2 \ldots 10^3\,\mathrm{K}$ confirm this assumption.

The scatter plots of $b_{\mathrm{CaII,NaI}}$ versus $\log N_{\mathrm{CaII}}, \log N_{\mathrm{NaI}}$ show a weak correlation of $b_{\mathrm{CaII}}\left[\mathrm{km\,s^{-1}}\right] = (2.4 \pm 0.5) \cdot \log N_{\mathrm{CaII}}\left[\mathrm{cm}^{-2}\right] + (-25 \pm 6)$, indicating that b_{CaII} increases with increasing $\log N_{\mathrm{CaII}}$. The b_{NaI} vs. $\log N_{\mathrm{NaI}}$ fit, $b_{\mathrm{NaI}}\left[\mathrm{km\,s^{-1}}\right] = (-0.9 \pm 0.5) \cdot \log N_{\mathrm{CaII}}\left[\mathrm{cm}^{-2}\right] + (13 \pm 6)$, has the opposite result: b_{NaI} decreases with increasing $\log N_{\mathrm{NaI}}$.

These results can be explained with the ionisation balance. In order to observe Na I (low ionisation potential), the density of the gas must be high and the temperature low to provide the necessary recombination rate. Assuming thermodynamic equilibrium, high densities mean lower temperatures and therefore, lower b-values. In case of Ca II the fraction of ionised to atomic calcium is of interest and expected to increase with increasing temperature and decreasing density.

The derived physical and statistical properties of the Ca II and Na I absorber suggest that these structures represent the local counterparts of strong Mg II ($W_\lambda > 0.3$Å) absorbing systems that are frequently observed at low and high redshift in QSO spectra and that are believed to trace the neutral and weakly ionized gas in the environment of other galaxies (within impact parameters of $D = 35\ldots100\,h^{-1}$kpc) at low and high redshifts. Of special importance is the fact that our derived Ca II CDD with a slops of $\beta = -1.7 \pm 0.2$ is similar to the slope found for Mg II absorbers of $\beta = -1.6 \pm 0.1$. This result indicates that both species probe similar gaseous structures in the extraplanar environment of galaxies.

8.2   Results from the H I high-resolution data

We performed follow-up high-resolution H I observations of four absorption systems out of the sample of sight lines where Ca II and Na I absorption and corresponding low-resolution H I emission was previously detected. The observation with radio synthesis telescopes are crucial to search for associated small-scale structures H I structures which possibly are not resolved with the Effelsberg telescope. The analysis of this small-scale structure provides an insight into the internal structure of IVCs and HVCs and gives information about physical processes in the ISM and IGM.

The observations with the WSRT and the VLA have revealed the presence of several cold compact (sub-pc scale) clumps in the direction of all four QSOs. These clumps have a relatively large absorption cross section of about 30%, implying that these clumps are very numerous in the Galactic halo.

The detected clumps have low peak column densities of $N_{\rm HI} \leq 3 \cdot 10^{19}\,{\rm cm}^{-2}$. The line widths of the clumpy structures are relatively narrow with $1.8 \leq \Delta v_{\rm FWHM} \leq 13\,{\rm km\,s}^{-1}$ leading to upper limits for the kinetic temperature of $70 \leq T_{\rm kin}^{\rm max} \leq 3700\,{\rm K}$. The temperatures are likely even lower, because effects like turbulences within the gas contribute to the observed line width. The small projected sizes and the relatively low temperatures of the observed clumps indicate that the small-scale structures are compact and cold rather than diffuse and extended.

The smallest spatial structures observed along the four sightlines are of similar size as the synthesised WSRT and VLA beam. Therefore, it is possible that the observed clumps are not resolved and contain structures on even smaller scales. This result raises the question whether IVCs and HVCs have fractal properties.

An important point is that not all components observed in the absorption data are also detected in H I emission with the interferometers. Furthermore there exist a slight velocity offset between the Ca II and Na I absorption components and the corresponding H I emission lines. This result not only shows that absorption spectroscopy is much more sensitive to low-column density gas but indicates that absorption and emission measurements trace somewhat different regions of the same overall structure. For our sample there

is not a single case where the QSO sightline passes through the center of the H I clumps. As a result, it was not possible to determine reliable metal abundances.

The directions and the velocities of the absorbing systems towards QSO J0003−2323 and QSO B1331+170 indicate a possible association with the Magellanic Stream and IV Spur, respectively. Assuming the known distances of the corresponding complexes physical parameters such as mass and pressure of the gas could be estimated. The calculated masses of all clumps are rather small with a few solar masses. The determined pressure limits for the absorbing systems towards the two QSOs were compared with the results of models performed by Wolfire et al. (1995) and are in good agreement with their results. Wolfire et al. (1995) obtained a pressure range of $P/k_\mathrm{B} \approx 20 \dots 180\,\mathrm{cm^{-3}K}$ for gas stripped from the Magellanic System due to tidal interactions with the Milky Way. Our derived upper pressure limits are consistent with the lower values of the pressure range. The other absorbing system towards QSO B1331+170 seems to be associated with the IV Spur. Therefore, we compared the derived pressure limits with the pressure ranges derived from a Galactic fountain model with two different dust-to-gas-ratios (D/G). Wolfire et al. (1995) found $P/k_\mathrm{B} \approx 150 \dots 650\,\mathrm{cm^{-3}K}$ ($D/G = 0.3$) and $P/k_\mathrm{B} \approx 650 \dots 3500\,\mathrm{cm^{-3}K}$ ($D/G = 1.0$). Since our determined pressure values are consistent with both ranges, we are not able to draw any conclusion which of the D/G ratio is preferred.

An independent method presented in Ben Bekhti et al. (2006) was applied to analyze the pressure variation as a function of distance or z-height, respectively. We computed the upper pressure limits as a function of the (unknown) distance to the cloud. The results were compared with the H I pressure expected in the vicinity of the Milky Way based on a model by Kalberla (2003) and Kalberla et al. (2007) and to models of Wolfire et al. (1995). The pressure limits determined for QSO J0003−2323 are consistent with both the Kalberla model and the Wolfire models. The pressure values of QSO B1331+170 are in agreement with the results of Wolfire et al. (1995) but are much lower than predicted by the Milky Way model. The comparison of the pressures of the remaining absorption systems in the direction of QSO B0450+1310B and J081331+254503 (with unknown distances) with the predicted P-values (from the Milky Way model) leads to upper (lower) distance limits of $z \leq 0.2 \dots 1\,\mathrm{kpc}$ ($z \geq 4 \dots 6\,\mathrm{kpc}$). Since all the derived P-values are afflicted with large uncertainties the results remain inconclusive.

8.3   Outlook

The presented results for the various data sets show us how important measurements at different wavelengths and with different resolutions are to get a complete view of the low-column density halo gas. Analysing several spectral regimes traces not only the variety of elements but also distinct gas phases and structure sizes. Furthermore, the achievable sensitivity differs substantially for the instruments used.

This work represents an important step on the way to systematically study the low-column density gaseous environment of the Milky Way and to characterise the role of the gas for the formation and evolution of our own galaxy. For the future we are planning to extend our study of extraplanar Ca II and Na I absorbers using additional high-resolution data from VLT/UVES, KECK and HST/STIS. This will allow us to enlarge our current absorption-selected data sample and to stabilise our statistical analysis of the distribution

and the physical properties of the halo gas. The analysis of absorption from various neutral and weakly ionised species such as O I and Si II will allow us to determine metallicities of the low-column density gas in the Milky Way halo (see Richter et al. 2008). The metallicity is an important parameter that will help to clarify whether the extraplanar gaseous structures are of Galactic or extragalactic origin and how they are related to Galactic structures (supernovae-ejections, winds, etc.). The hopefully available HST/COS data (near-uv) will be used for an extensive study of weak and strong Mg II systems in the halo of the Milky Way and to compare their characteristics with the properties of Mg II systems widely observed in the extraplanar environment of other low- and high-z galaxies.

The absorption-selected data will be supplemented with new deep H I 21-cm data. We will have access to the Effelsberg Bonn H I survey (EBHIS), a fully-sampled survey of the whole northern sky. For the southern sky we can use data from the Galactic All-Sky Survey (GASS, McClure-Griffiths et al. 2006). With these deep H I observations we can map the small gaseous structures in the halo of the Milky Way and determine their overall distribution. The moderate angular resolution data of EBHIS enable us to study the multi-phase structure of the absorbing gas. The high velocity resolution of $1.3\,\mathrm{km\,s^{-2}}$ provides a clear separation of the cold and the warm gas phase. The EBHIS data will allow us to investigate quantitatively the column density distribution of the halo gas down to the column density limit of $N_{\mathrm{HI}} = 10^{18}\,\mathrm{cm^{-2}}$.

The measurements with singe-dish telescopes are crucial to prepare follow-up observations with high-resolution synthesis telescopes to extend the search for small-scale structures. Observations with the VLA, the WSRT, and the Australia Telescope Compact Array (ATCA) are necessary to answer the question whether these structures are common in the extraplanar environment of the Milky Way. Studying the connection between the different gas phases in the halo of our own Galaxy is of special importance for the understanding of the formation and evolution processes of the Milky Way and other galaxies and to place their circumgalactic gaseous environment into a cosmological context.

In the near future new instruments will shed light on many unsolved questions and will open new windows to different astronomical fields. The Cosmic Origins Spectrograph (COS) is a new instrument for the Hubble Space Telescope that will be installed in 2009. This instrument will allow QSO absorption spectroscopy in the wavelength regime between 1150-3000 Å (ground based telescopes are limited to ~ 3000 Å due to the atmospheric cutoff). One of the main scientific drivers for this instrument is the study of the origins of large-scale structure in the universe. The Atacama Large Millimeter Array (ALMA) will open up the millimeter and submillimeter wavelength range. This instrument will reveal the earliest days of the universe and allow for the detailed observation of galaxy formation. The array is expected to resolve distant objects at least five to ten times better than the Hubble Space Telescope or the VLA. The Square Kilometer Array (SKA) will be the world's largest radio telescope with a receiving surface of a million square metres, one hundred times larger than the biggest receiving surface now in existence. The SKA as well as its pathfinder project, the Low Frequency Array (LOFAR) will shed light on the so-called Dark Ages, when the early universe was in a neutral gaseous form before the formation of stars and galaxies. It will also give information about the development of these first stars and galaxies.

Appendix

A.1 Determination of an upper temperature limit using the line width

Using the Maxwellian velocity distribution and taking into account the Doppler effect one gets an expression for the line-(Doppler-)broadening

$$\Delta\nu_{\mathrm{D}} = \frac{2}{\lambda_0}\sqrt{\frac{2\mathrm{k_B}T\ln 2}{m}}\,. \tag{A.1}$$

Solving for the temperature results in

$$T = \left(\frac{\Delta\nu_{\mathrm{D}}\lambda_0}{2}\right)^2 \frac{m}{2\mathrm{k_B}\ln 2} \tag{A.2}$$

with λ_0 the restfrequency, m the mass of an hydrogen Atom and $\mathrm{k_B}$ the Boltzmann constant. Using

$$\frac{\Delta\lambda}{\lambda_0} = \frac{\Delta v_{\mathrm{D}}}{c} \tag{A.3}$$

with $\lambda_0 = \frac{c}{\nu_0}$ and $\Delta\lambda = \frac{c}{\nu_0^2}\Delta\nu_{\mathrm{D}}$ leads to an expression for ν_{D}

$$\Delta\nu_{\mathrm{D}} = \frac{\Delta v_{\mathrm{D}}}{c}\nu_0\,. \tag{A.4}$$

Using Eq. (A.2) and (A.4) provides the temperature as a function of the velocity width Δv_{D}

$$T = \frac{m\Delta v_{\mathrm{D}}^2}{8\mathrm{k_B}\ln 2}\,. \tag{A.5}$$

A.2 Ca II, Na I, and H I spectra in the direction of 53 QSOs
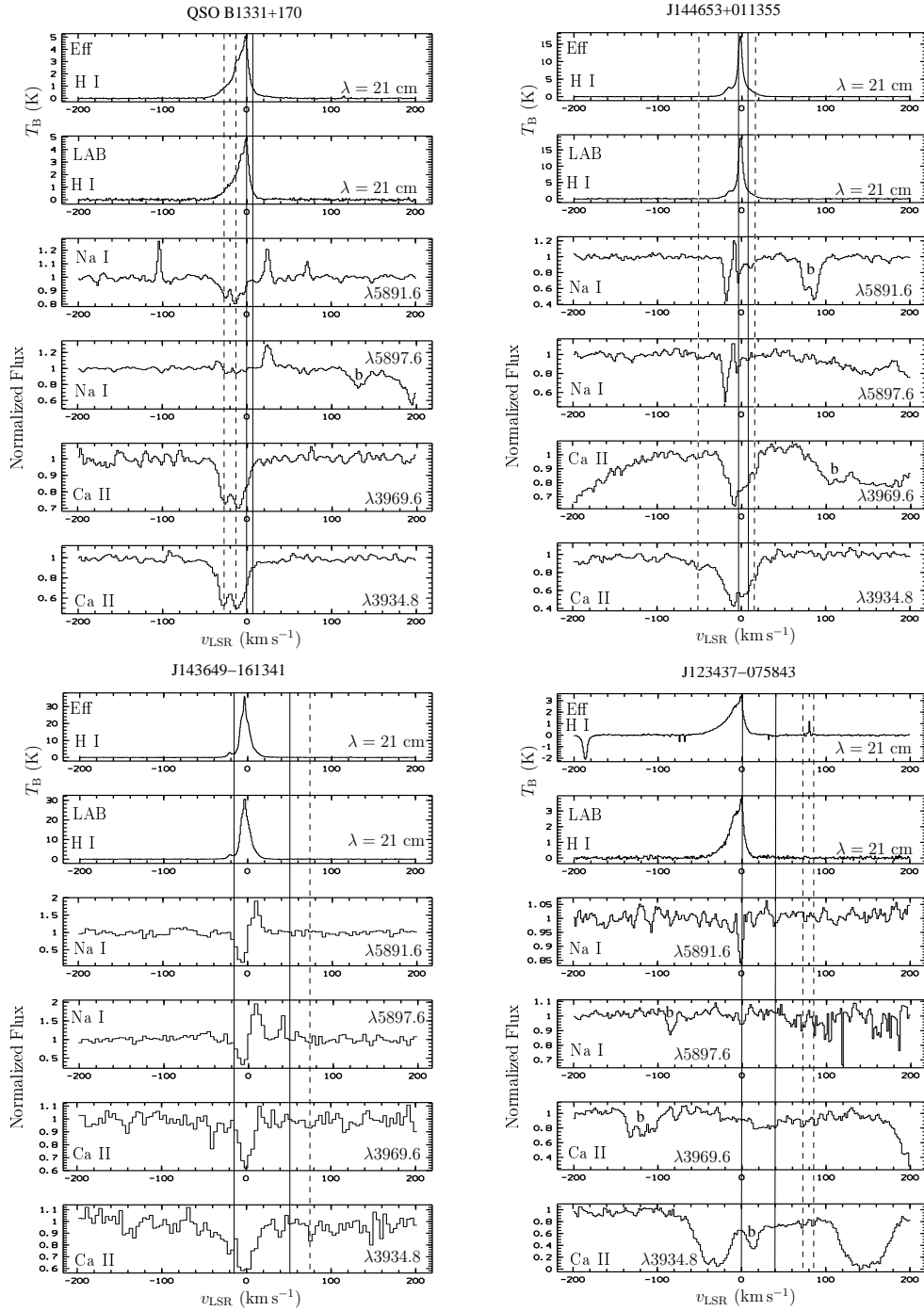
Fig. A.1: Ca II and Na I absorption and H I emission spectra in the direction of the QSOs QSO B1331+170, J144653+011355, J143649−161341, and J123437−075843 obtained with UVES and the 100-m telescope at Effelsberg. Additionally shown are the archival H I data from the Leiden-Argentine-Bonn (LAB) survey (Kalberla 2003). The absorption and corresponding emission lines are indicated by dashed lines. The solid lines mark the minimal and maximal LSR velocity which is expected for the galactic disc gas in this direction according to the Milky Way model developed by Kalberla (2003); Kalberla et al. (2007). b denotes blending lines from intervening absorption systems. The spikes in the Effelsberg spectra are radio frequency interferences (RFI).
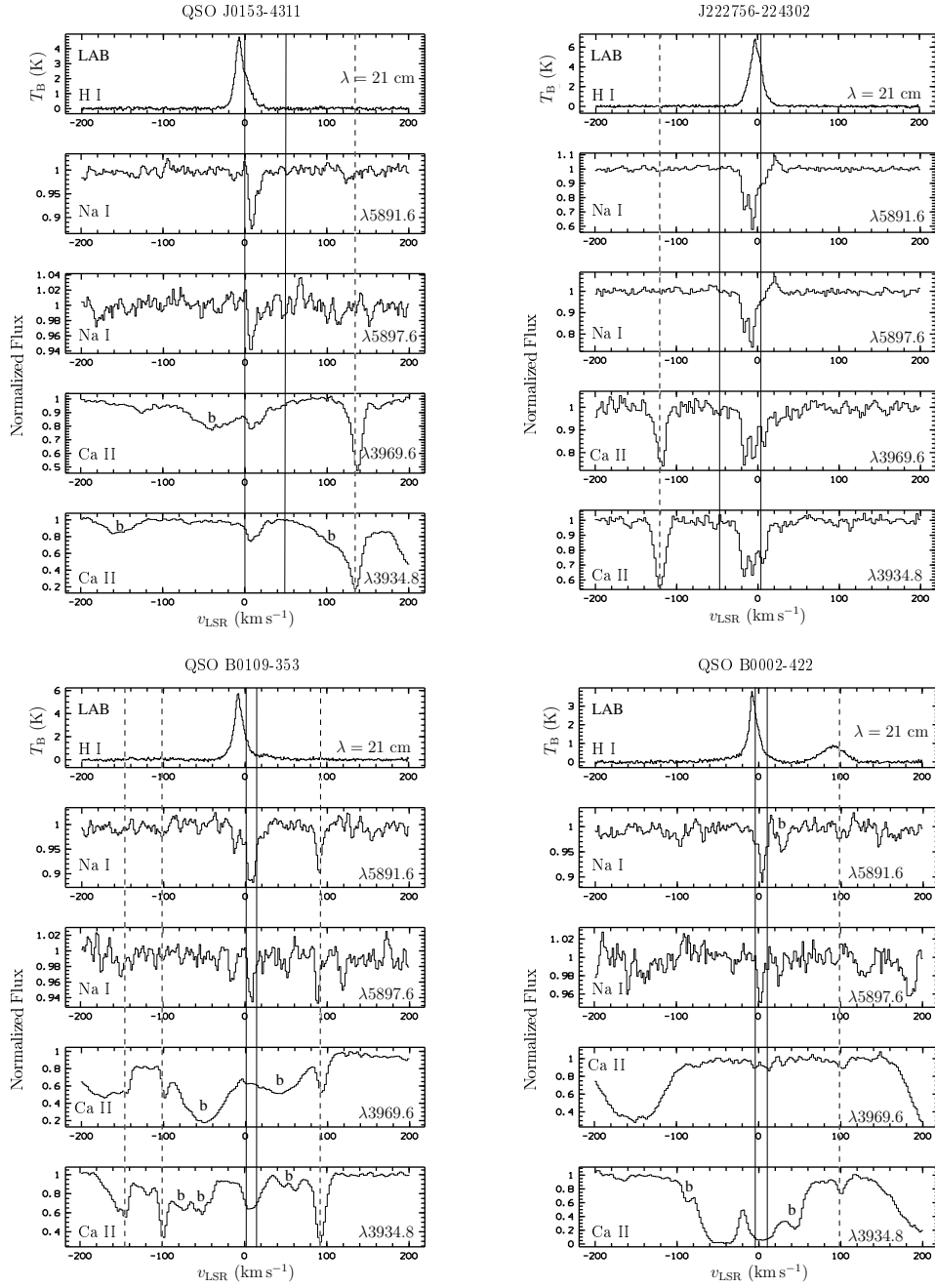
Fig. A.2: As Figure A.1 for the sight lines in the direction of QSO J0153−4311, J222756−224302, QSO B0109−353, and QSO B0002−422.
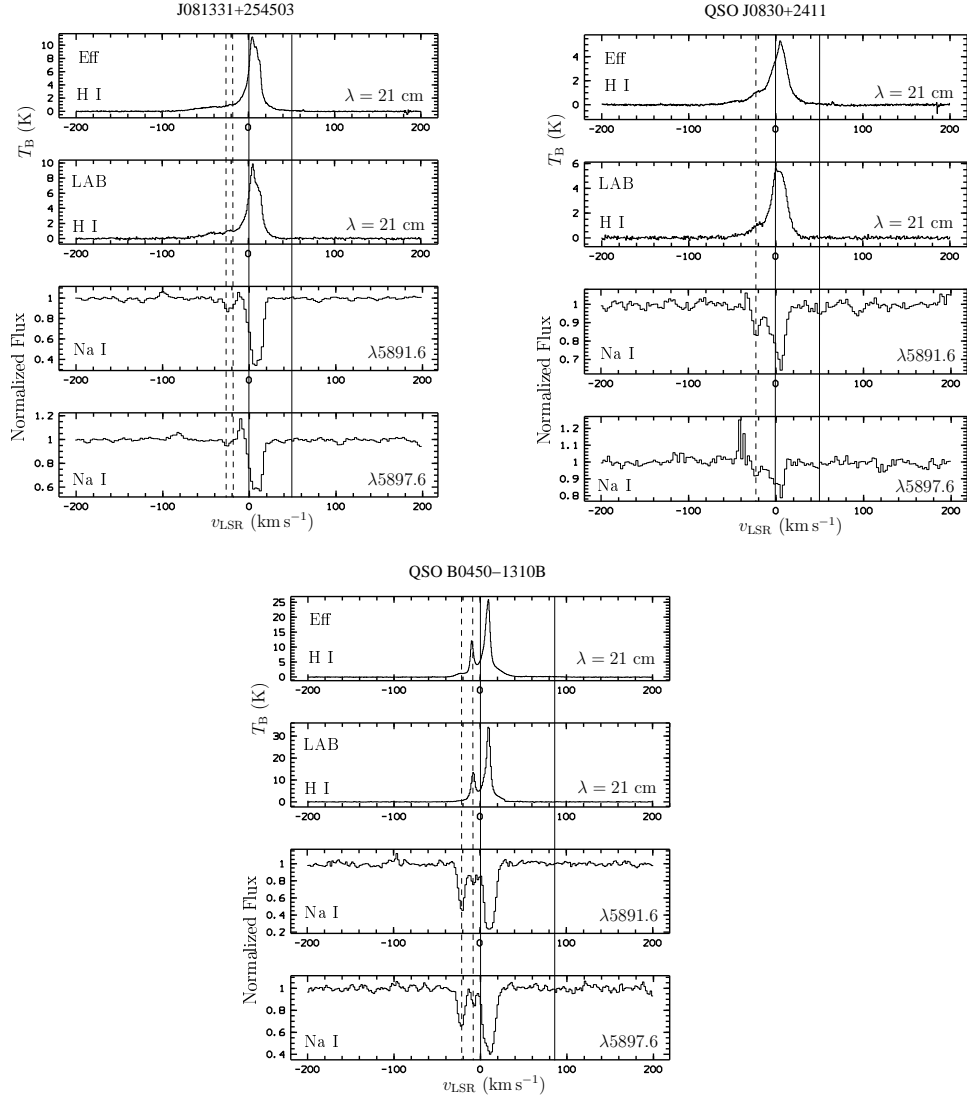
Fig. A.3: As Figure A.1 for the sight lines in the direction of J081331+254503, QSO J0830+2411, and QSO B0450−1310B.
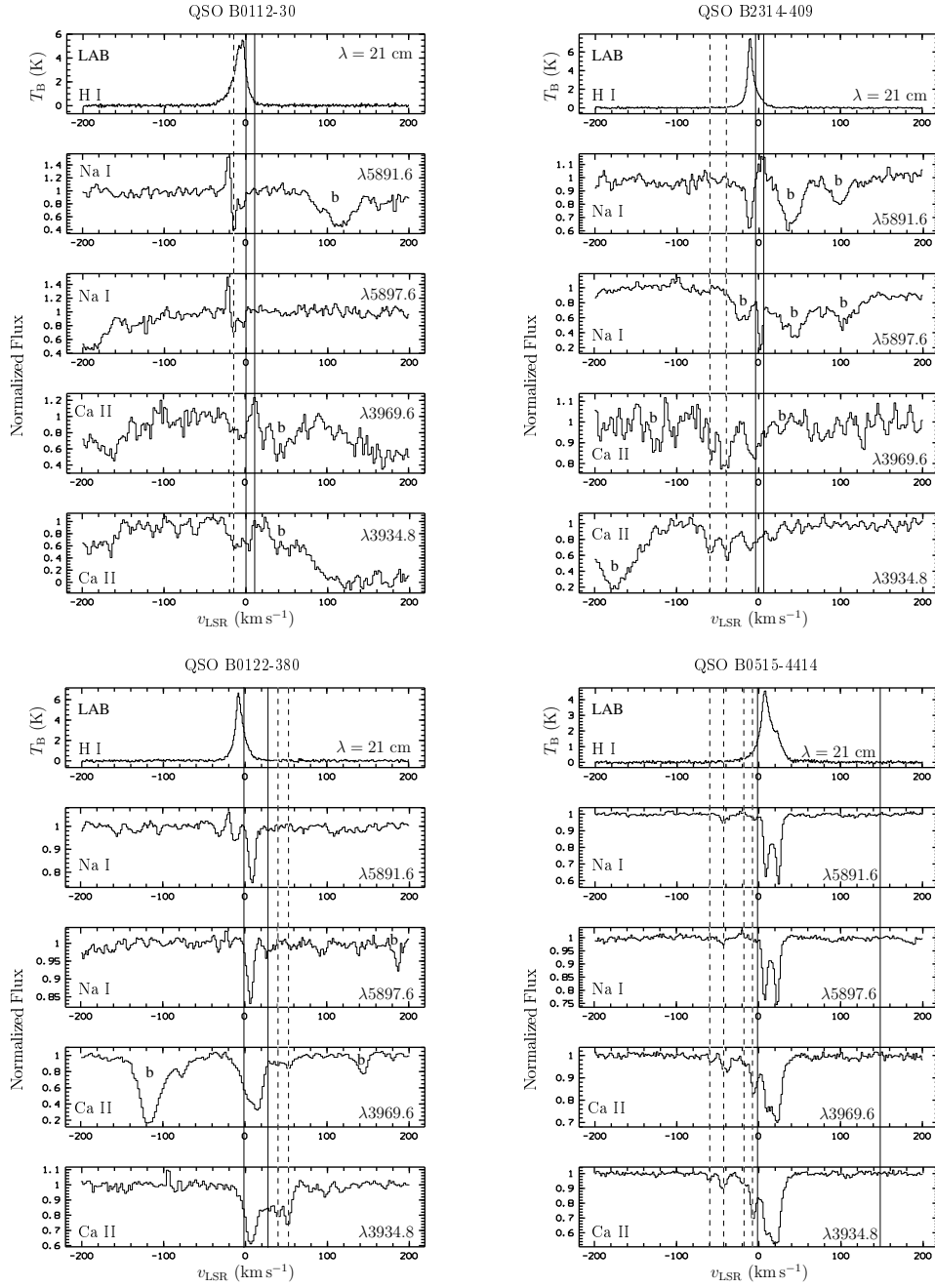
Fig. A.4: As Fig. A.1 but towards QSO B0112−30, QSO B2314−409, QSO B0122−379, and QSO B0515−4414.
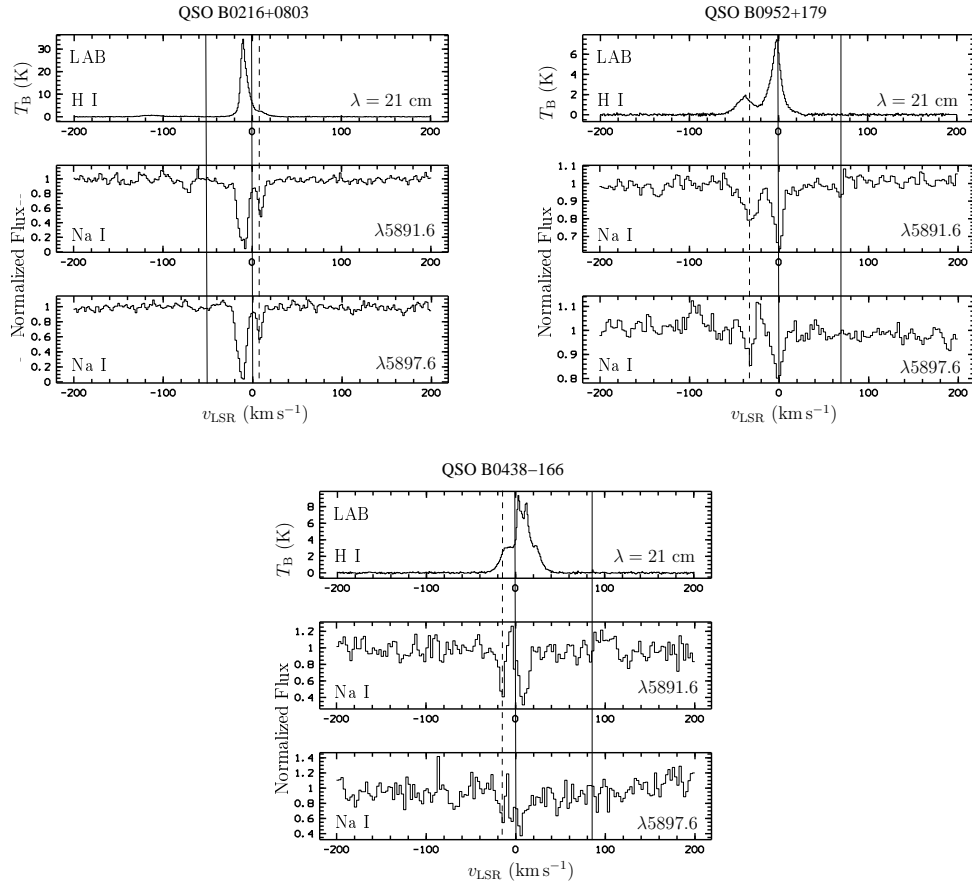
Fig. A.5: As Figure A.1 for the sight lines in the direction of QSO B0216+0803, QSO B0952+179, and QSO B0438−166.
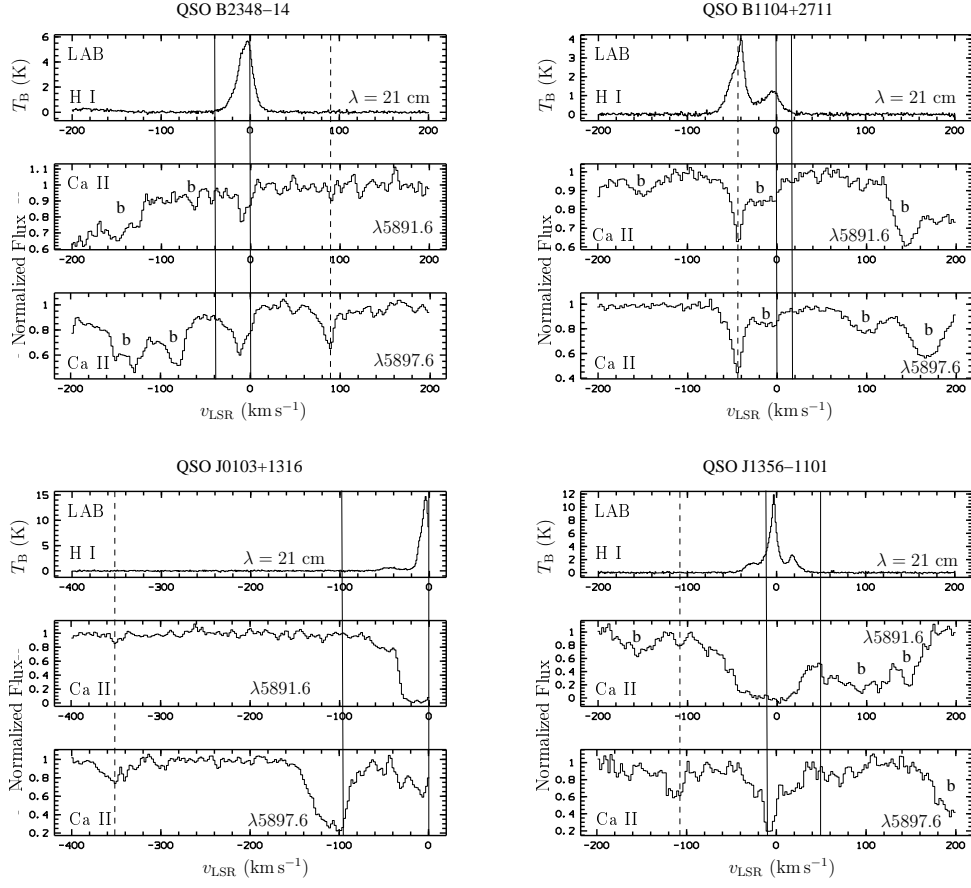
Fig. A.6: As Fig. A.1 but towards QSO B2348−147, QSO B1140+2711, QSO J0103+1316, and QSO J1356−1101.
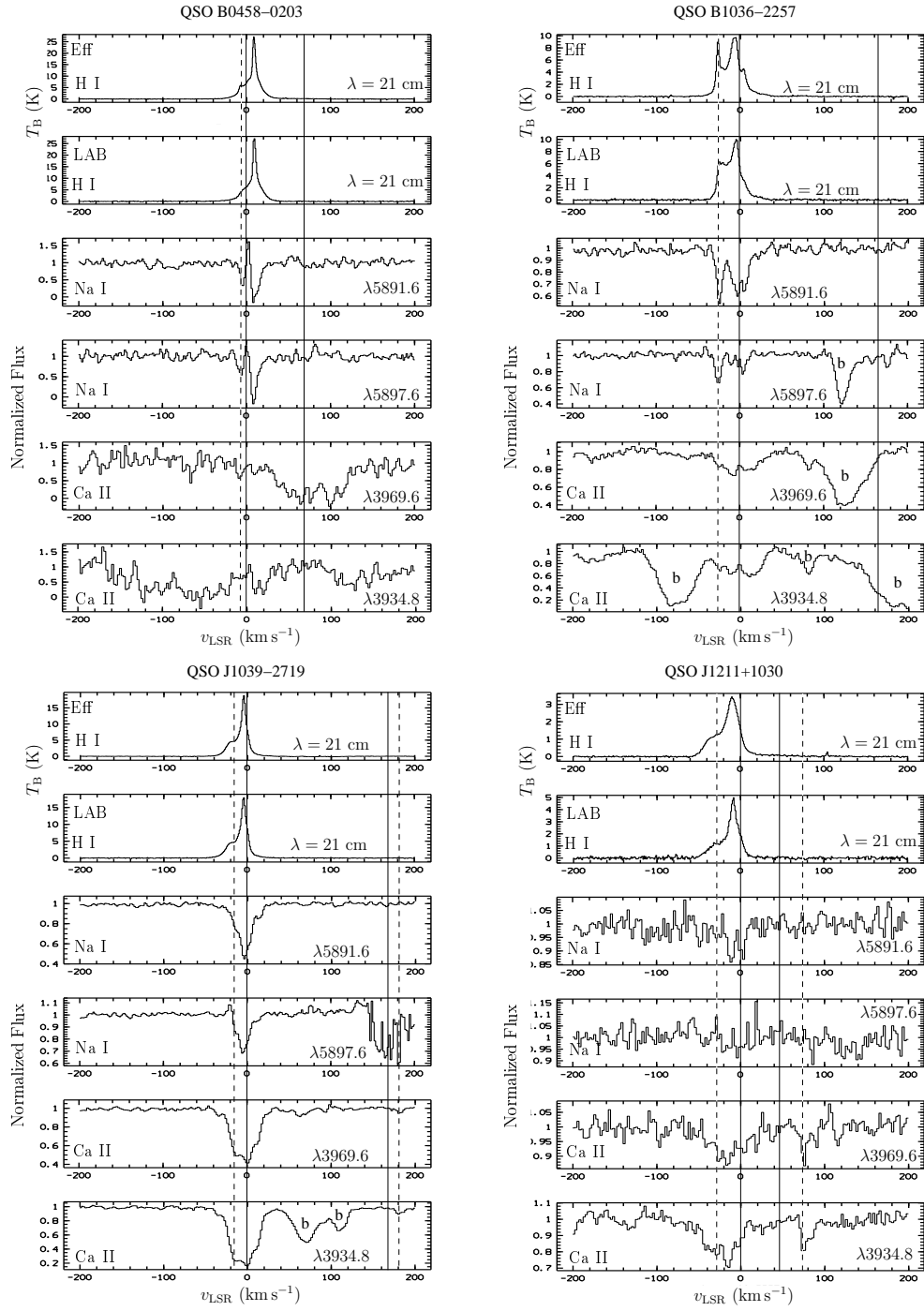
Fig. A.7: As Fig. A.1 but towards QSO B0458−0203, QSO B1036−2257, QSO J1039−2719, and QSO J1211+1030.
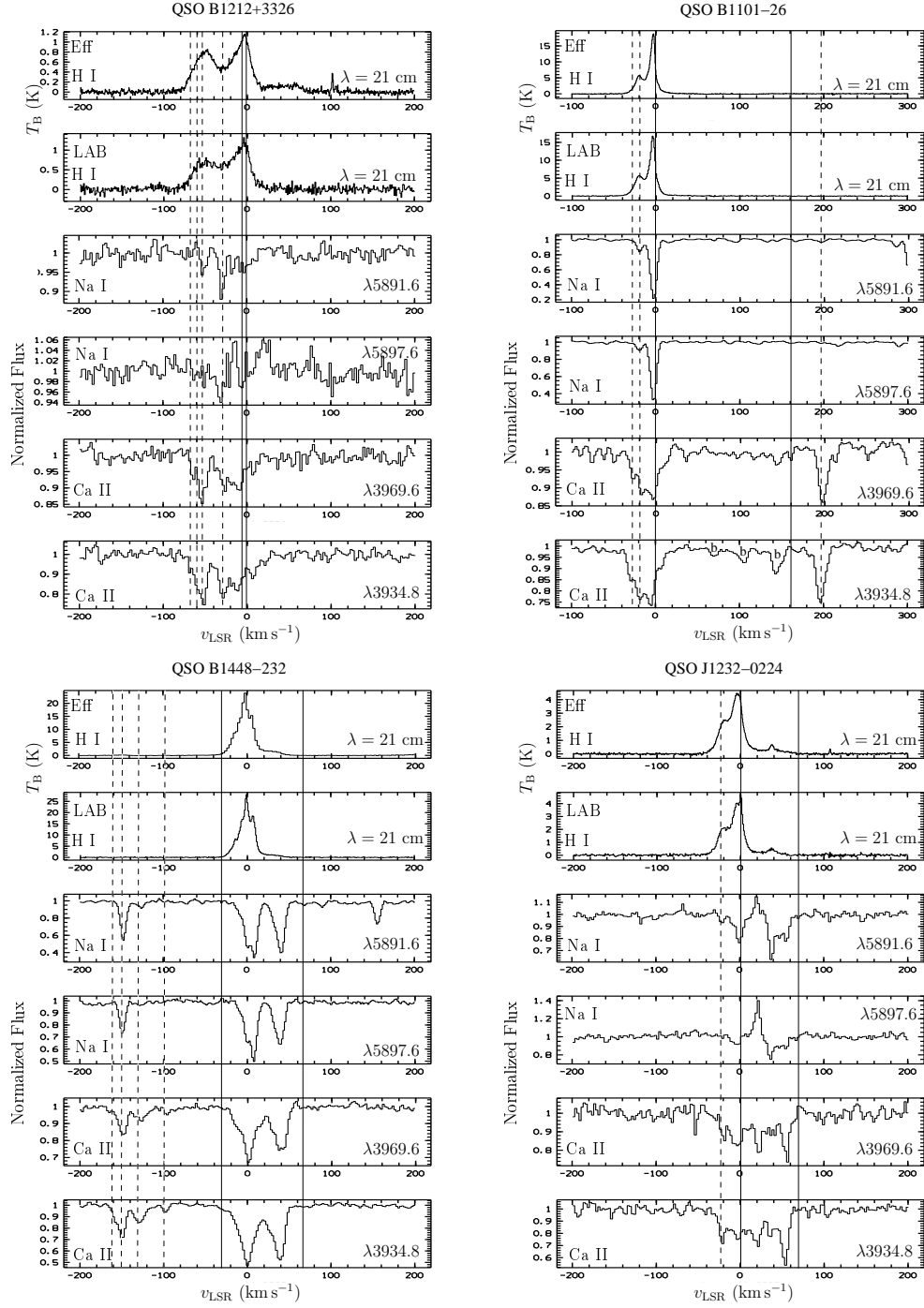
Fig. A.8: As Fig. A.1 but in the direction of QSO B1212−3326, QSO B1101−26, QSO B1448−232, and QSO J1232−0224.
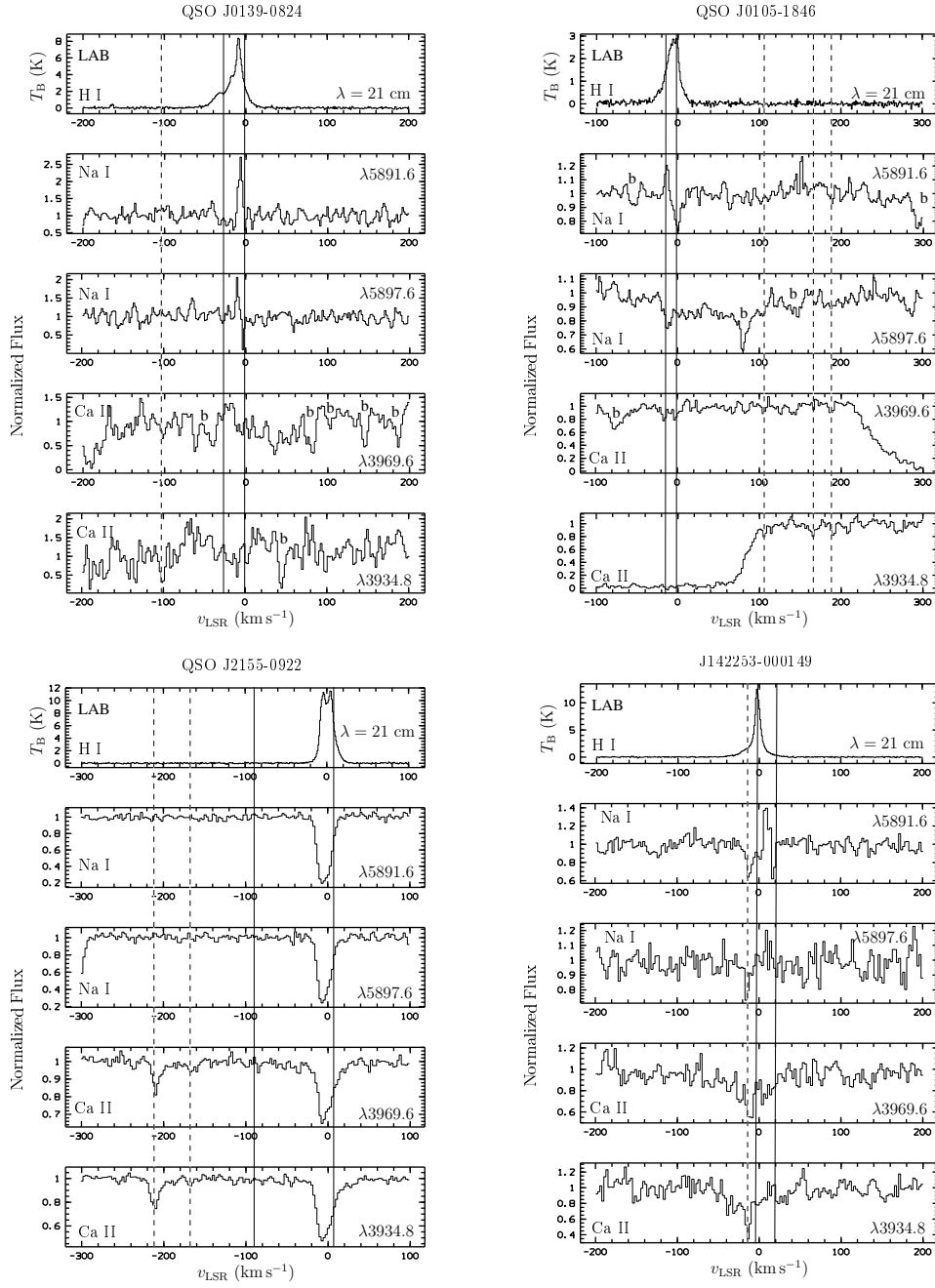
Fig. A.9: As Fig. A.1 but in the direction of QSO J0139−0824, QSO J0105−1846, QSO J2155−0922, and J142253−000149.
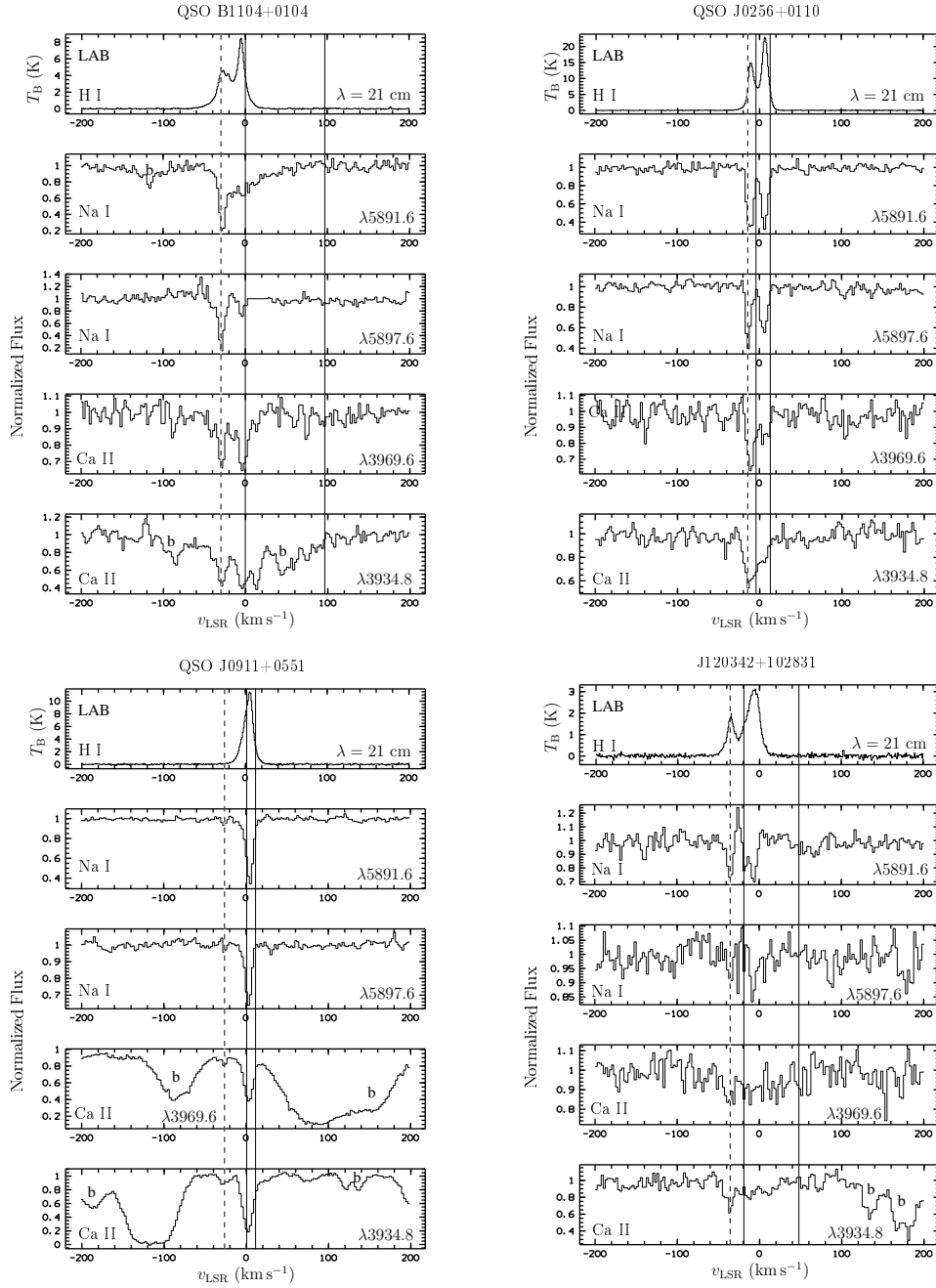
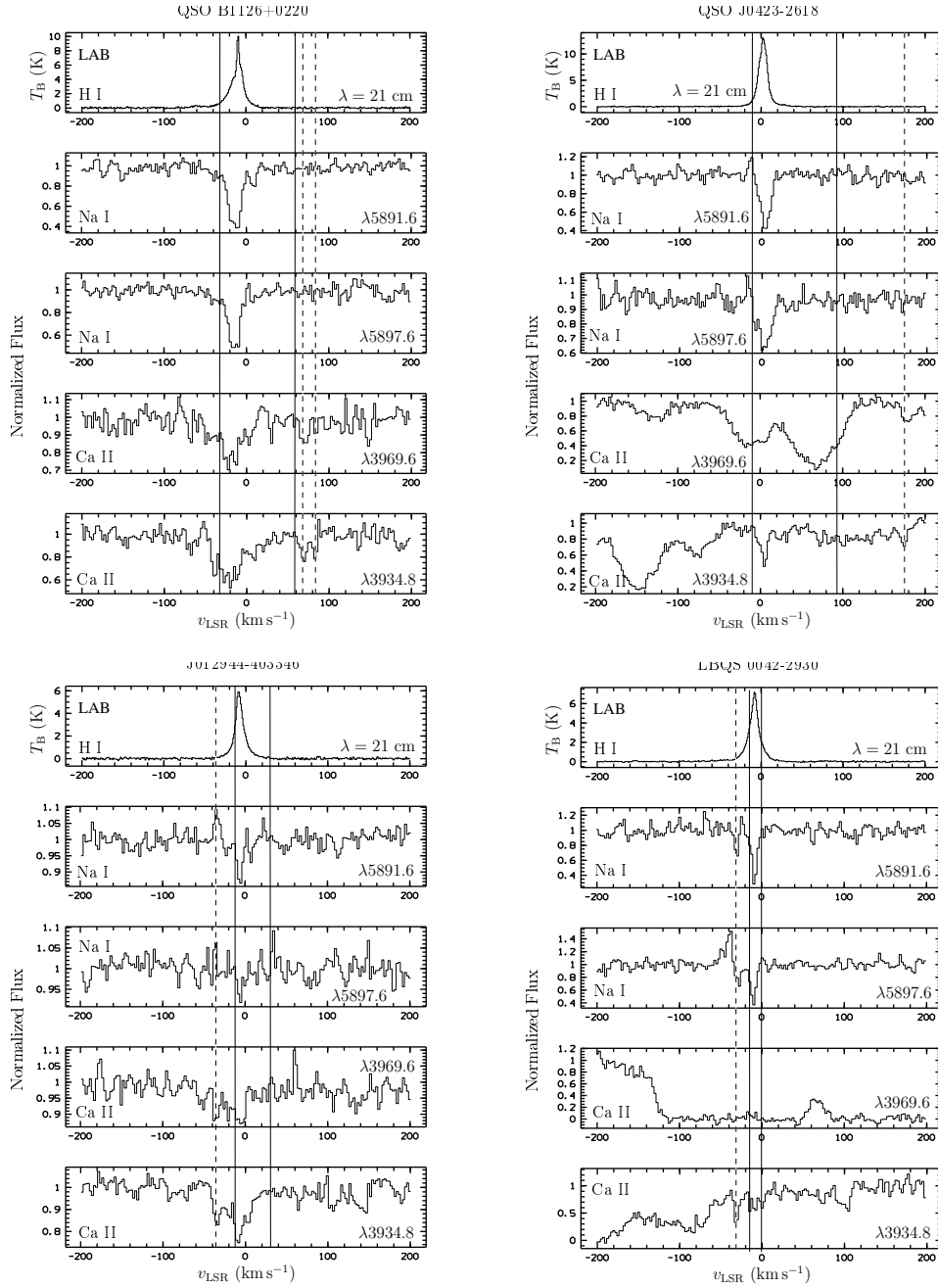**Fig.   A.10:**   As   Fig. A.1   but   towards   QSO B1104−0104,   QSO J0256+0110,   QSO J0911+0551, and J120342+102831.

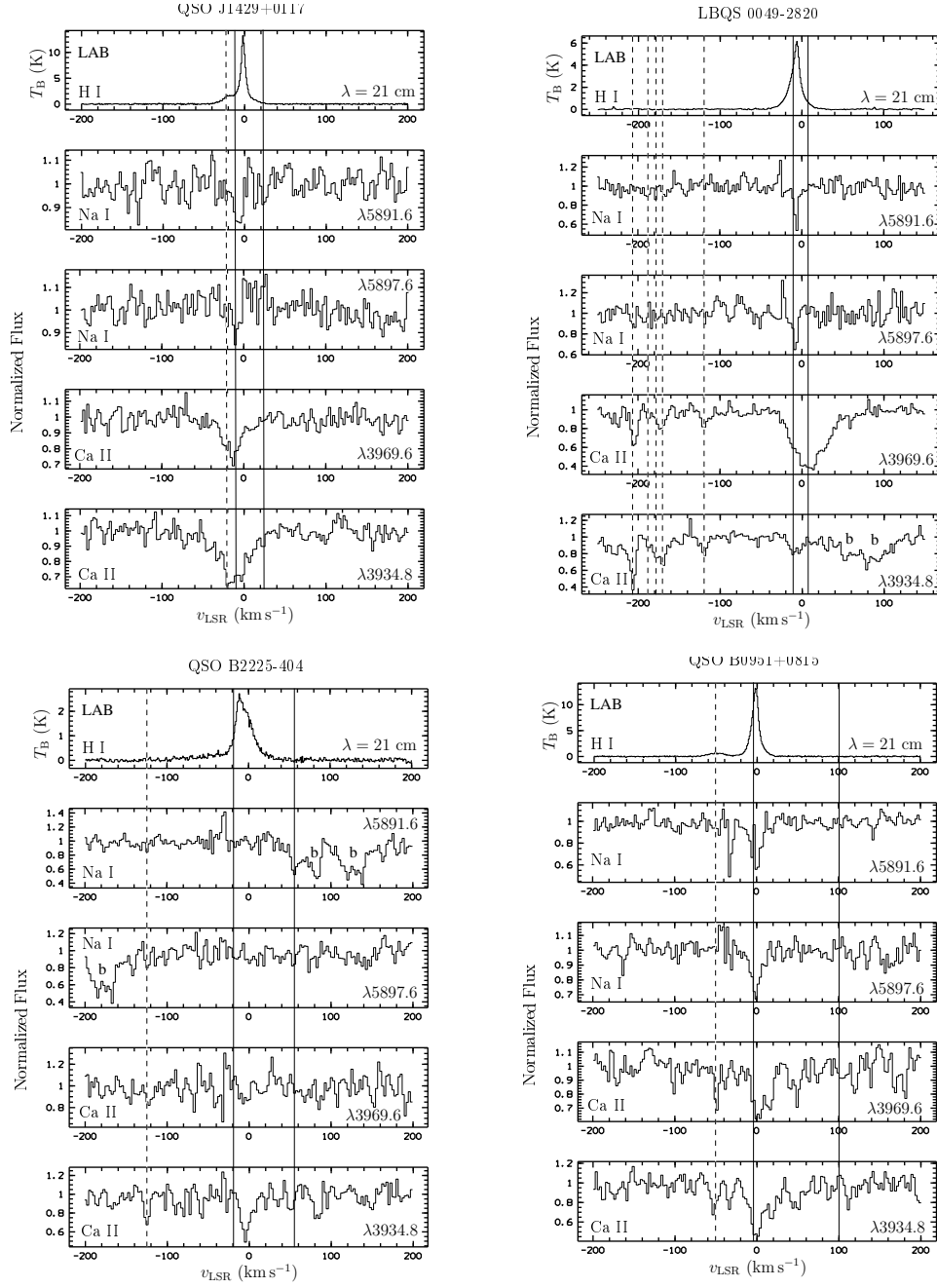**Fig. A.11:** As Fig. A.1 but towards QSO B1126−0220, QSO J0423+2618, J012944−403346, and LBQS 0042−2930.

Fig. A.12: As Fig. A.1 but towards QSO J1429+0117, LBQS 0049−2820, QSO B2225−404, and QSO B0951+0815.
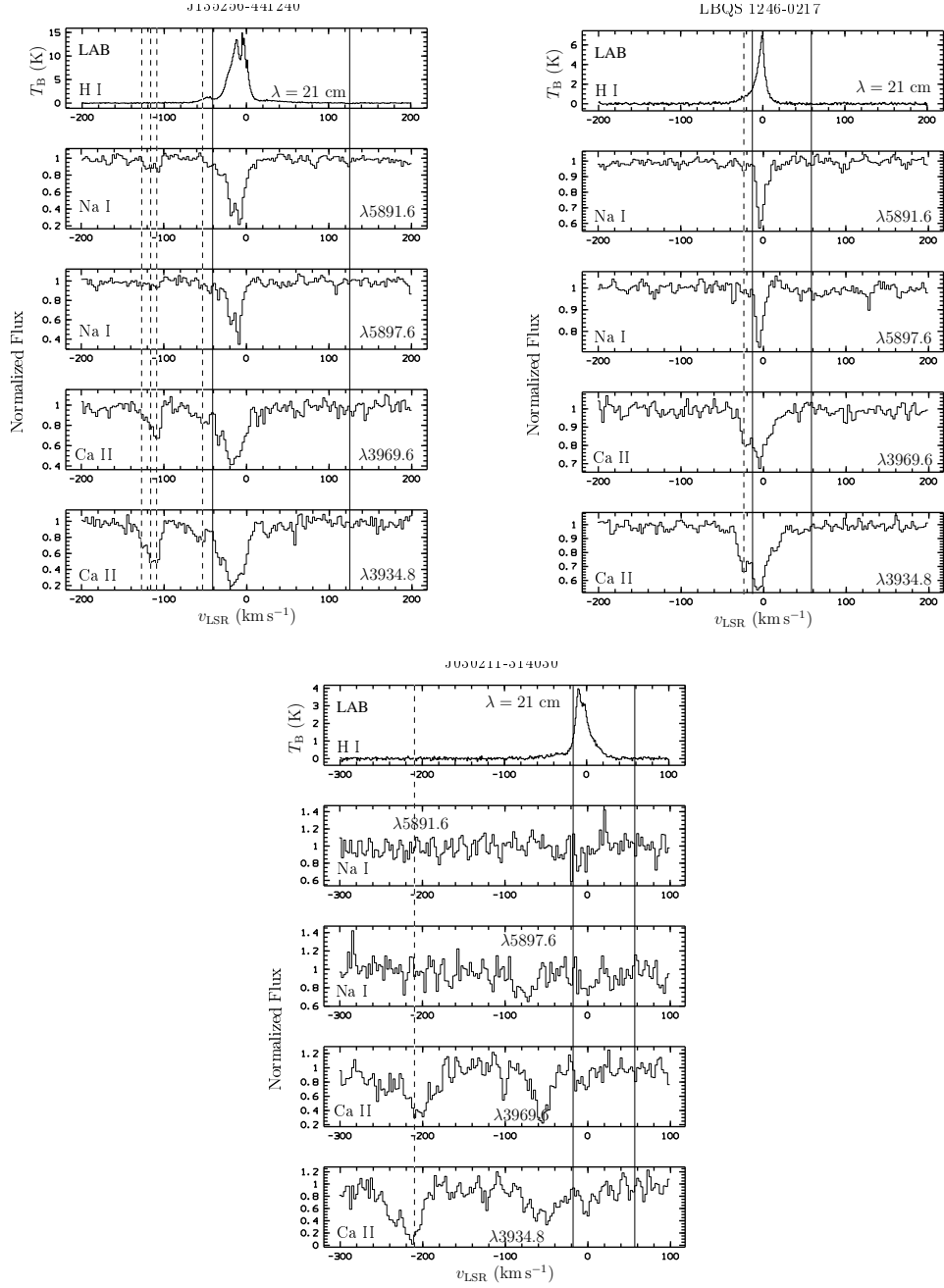
Fig. A.13: As Fig. A.1 for the sight lines in the direction of J135256−441240, LBQS 1246−0217, and J030211−314030.

Bibliography

Arnal, E. M., Bajaja, E., Larrarte, J. J., Morras, R., & Pöppel, W. G. L. 2000, A&AS, 142, 35

Bahcall, J. N. 1966, ApJ, 145, 684

Bahcall, J. N. & Salpeter, E. E. 1965, ApJ, 142, 1677

Bajaja, E., Arnal, E. M., Larrarte, J. J., et al. 2005, A&A, 440, 767

Ballester, P. 1992, in European Southern Observatory Astrophysics Symposia, Vol. 41, European Southern Observatory Astrophysics Symposia, ed. P. J. Grosbøl & R. C. E. de Ruijsscher, 177–+

Ballester, P., Modigliani, A., Boitquin, O., et al. 2000, The ESO Messenger, 101, 31

Bell, E. F., McIntosh, D. H., Katz, N., & Weinberg, M. D. 2003, ApJS, 149, 289

Ben Bekhti, N., Brüns, C., Kerp, J., & Westmeier, T. 2006, A&A, 457, 917

Ben Bekhti, N., Richter, P., Westmeier, T., & Murphy, M. T. 2008a, A&A, 487, 583

Ben Bekhti, N., Richter, P., Winkel, B., Kenn, F., & Westmeier, T. 2008b, A&A, submitted

Bergeron, J., Petitjean, P., Aracil, B., et al. 2004, The Messenger, 118, 40

Bertin, P., Lallement, R., Ferlet, R., & Vidal-Madjar, A. 1993, A&A, 278, 549

Bland-Hawthorn, J., Veilleux, S., Cecil, G. N., et al. 1998, MNRAS, 299, 611

Blitz, L., Spergel, D. N., Teuben, P. J., & Hartmann, D. 1999a, in Astronomical Society of the Pacific Conference Series, Vol. 166, Stromlo Workshop on High-Velocity Clouds, ed. B. K. Gibson & M. E. Putman, 125–+

Blitz, L., Spergel, D. N., Teuben, P. J., Hartmann, D., & Burton, W. B. 1999b, ApJ, 514, 818

Bond, J. R., Kofman, L., & Pogosyan, D. 1996, Nature, 380, 603

Bond, N. A., Churchill, C. W., Charlton, J. C., & Vogt, S. S. 2001, ApJ, 562, 641

Bouché, N., Murphy, M. T., Péroux, C., Csabai, I., & Wild, V. 2006, MNRAS, 813

Brüns, C. 1998, in Astronomische Gesellschaft Meeting Abstracts, 5

Brüns, C., Kerp, J., & Pagels, A. 2001, A&A, 370, L26

Braun, R. & Burton, W. B. 1999, A&A, 341, 437

Bregman, J. N. 1980, ApJ, 236, 577

Bregman, J. N. 2004, in ASSL Vol. 312: High Velocity Clouds, 341

Brüns, C. & Westmeier, T. 2004, A&A, 426, L9

Cen, R., Miralda-Escudé, J., Ostriker, J. P., & Rauch, M. 1994, ApJ, 437, L9

Cen, R. & Ostriker, J. P. 1999, ApJ, 514, 1

Charlton, J. C. & Churchill, C. W. 1998, ApJ, 499, 181

Charlton, J. C., Churchill, C. W., & Rigby, J. R. 2000, ApJ, 544, 702

Charlton, J. C., Ding, J., Zonak, S. G., et al. 2003, ApJ, 589, 111

Churchill, C. W., Rigby, J. R., Charlton, J. C., & Vogt, S. S. 1999, ApJS, 120, 51

Churchill, C. W., Vogt, S. S., & Charlton, J. C. 2003, AJ, 125, 98

Chynoweth, K. M., Langston, G. I., Yun, M. S., et al. 2008, ArXiv e-prints, astro-ph/0803.3631

Cornwell, T. J. & Evans, K. F. 1985, A&A, 143, 77

Crawford, I. A., Lallement, R., Price, R. J., et al. 2002, MNRAS, 337, 720

Davé, R. 2003, ArXiv e-prints, astro-ph/0311518

Davé, R., Cen, R., Ostriker, J. P., et al. 2001, ApJ, 552, 473

de Boer, K. S. 2004, A&A, 419, 527

de Boer, K. S. 2006, Physics and the interstellar medium (Argelander-Institut für Astronomie, Universität Bonn)

de Boer, K. S., Koppenaal, K., & Pottasch, S. R. 1973, A&A, 28, 145

de Heij, V., Braun, R., & Burton, W. B. 2002, A&A, 391, 159

Dekker, H., D'Odorico, S., Kaufer, A., Delabre, B., & Kotzlowski, H. 2000, in Proc. SPIE Vol. 4008, p. 534-545, Optical and IR Telescope Instrumentation and Detectors, Masanori Iye; Alan F. Moorwood; Eds., ed. M. Iye & A. F. Moorwood, 534–545

Ding, J., Charlton, J. C., Bond, N. A., Zonak, S. G., & Churchill, C. W. 2003a, ApJ, 587, 551

Ding, J., Charlton, J. C., & Churchill, C. W. 2005, ApJ, 621, 615

Ding, J., Charlton, J. C., Churchill, C. W., & Palma, C. 2003b, ApJ, 590, 746

Dunkley, J., Komatsu, E., Nolta, M. R., et al. 2008, ArXiv e-prints

Ellison, S. L., Mallén-Ornelas, G., & Sawicki, M. 2003, ApJ, 589, 709

Erni, P. 2007, PhD thesis, Argelander-Institut für Astronomie, Bonn University

Fraternali, F., Binney, J., Oosterloo, T., & Sancisi, R. 2007, New Astronomy Review, 51, 95

Fraternali, F. & Binney, J. J. 2006, MNRAS, 366, 449

Gardiner, L. T. & Noguchi, M. 1996, MNRAS, 278, 191

Gunn, J. E. & Peterson, B. A. 1965, ApJ, 142, 1633

Högbom, J. A. 1974, A&AS, 15, 417

Hartmann, D. & Burton, W. B. 1997, Atlas of Galactic Neutral Hydrogen (Atlas of Galactic Neutral Hydrogen, by Dap Hartmann and W. Butler Burton, pp. 243. ISBN 0521471117. Cambridge, UK: Cambridge University Press, February 1997.)

Hinshaw, G., Weiland, J. L., Hill, R. S., et al. 2008, ArXiv e-prints

Hoffman, G. L., Salpeter, E. E., & Hirani, A. 2004, AJ, 128, 2932

Józsa, G. I. G. 2002, Master's thesis, Universität Bonn

Kalberla, P. M. W. 2003, ApJ, 588, 805

Kalberla, P. M. W., Burton, W. B., Hartmann, D., et al. 2005a, A&A, 440, 775

Kalberla, P. M. W., Burton, W. B., Hartmann, D., et al. 2005b, A&A, 440, 775

Kalberla, P. M. W., Dedes, L., Kerp, J., & Haud, U. 2007, A&A, 469, 511

Kalberla, P. M. W. & Haud, U. 2006, A&A

Kalberla, P. M. W., Mebold, U., & Reich, W. 1980, A&A, 82, 275

Kim, T.-S., Carswell, R. F., Cristiani, S., D'Odorico, S., & Giallongo, E. 2002, MNRAS, 335, 555

Klein, K. 2006/2007, Radio Astronomy-Tools, applications and impacts (Argelander-Institut für Astronomie, Universität Bonn)

Klypin, A., Kravtsov, A. V., Valenzuela, O., & Prada, F. 1999, ApJ, 522, 82

Kondo, S., Kobayashi, N., Minowa, Y., et al. 2006, ApJ, 643, 667

Lehner, N., Savage, B. D., Richter, P., et al. 2007, ApJ, 658, 680

Lockman, F. J., Murphy, E. M., Petty-Powell, S., & Urick, V. J. 2002, ApJS, 140, 331

Majewski, S. 2004, in Astronomical Society of the Pacific Conference Series, Vol. 327, Satellites and Tidal Streams, ed. F. Prada, D. Martinez Delgado, & T. J. Mahoney, 63

Masiero, J. R., Charlton, J. C., Ding, J., Churchill, C. W., & Kacprzak, G. 2005, ApJ, 623, 57

Mathewson, D. S., Cleary, M. N., & Murray, J. D. 1974, ApJ, 190, 291

McClure-Griffiths, N. M., Ford, A., Pisano, D. J., et al. 2006, ApJ, 638, 196

Meiksin, A. A. 2007, ArXiv e-prints, astro-ph/0711.3358

Milutinović, N., Rigby, J. R., Masiero, J. R., et al. 2006, ApJ, 641, 190

Moore, B., Quinn, T., Governato, F., Stadel, J., & Lake, G. 1999, MNRAS, 310, 1147

Moos, W., Sembach, K., & Bianchi, L. 1998, in Astronomical Society of the Pacific Conference Series, Vol. 148, Origins, ed. C. E. Woodward, J. M. Shull, & H. A. Thronson, Jr., 304

Muller, C. A., Oort, J. H., & Raimond, E. 1963, C. R. Acad. Sc. Paris, 257, 1661

Oort, J. H. 1966, Bull. Astron. Inst. Netherlands, 18, 421

Oosterloo, T. 2004, in Astrophysics and Space Science Library, Vol. 312, High Velocity Clouds, ed. H. van Woerden, B. P. Wakker, U. J. Schwarz, & K. S. de Boer, 125

Peek, J. E. G., Putman, M. E., & Sommer-Larsen, J. 2008, ApJ, 674, 227

Petitjean, P. & Bergeron, J. 1990, A&A, 231, 309

Petitjean, P., Webb, J. K., Rauch, M., Carswell, R. F., & Lanzetta, K. 1993, MNRAS, 262, 499

Prause, N., Reimers, D., Fechner, C., & Janknecht, E. 2007, A&A, 470, 67

Prochter, G. E., Prochaska, J. X., & Burles, S. M. 2006, ApJ, 639, 766

Quilis, V. & Moore, B. 2001, ApJ, 555, L95

Rao, S. M., Turnshek, D. A., & Nestor, D. B. 2006, ApJ, 636, 610

Richter, P. 2005, Intergalactic medium, Lecture notes (Institut für Astrophysik und Extraterrestriche Forschung, Universität Bonn)

Richter, P. 2006, ArXiv e-prints, astro-ph/0602343

Richter, P., de Boer, K. S., Widmann, H., et al. 1999, Nature, 402, 386

Richter, P., Paerels, F. B. S., & Kaastra, J. S. 2008, Space Science Reviews, 134, 25

Richter, P., Savage, B. D., Sembach, K. R., Tripp, T. M., & Jenkins, E. B. 2003a, in Astrophysics and Space Science Library, Vol. 281, The IGM/Galaxy Connection. The Distribution of Baryons at z=0, ed. J. L. Rosenberg & M. E. Putman, 85

Richter, P., Savage, B. D., Tripp, T. M., & Sembach, K. R. 2004, in Baryons in Dark Matter Halos, ed. R. Dettmar, U. Klein, & P. Salucci

Richter, P., Sembach, K. R., Wakker, B. P., & Savage, B. D. 2001a, ApJ, 562, L181

Richter, P., Sembach, K. R., Wakker, B. P., et al. 2001b, ApJ, 559, 318

Richter, P., Wakker, B. P., Savage, B. D., & Sembach, K. R. 2003b, ApJ, 586, 230

Richter, P., Westmeier, T., & Brüns, C. 2005, A&A, 442, L49

Rigby, J. R., Charlton, J. C., & Churchill, C. W. 2002, ApJ, 565, 743

Rohlfs, K. & Wilson, T. L. 1996, Tools of Radio Astronomy (Tools of Radio Astronomy, XVI, 423 pp. 127 figs., 20 tabs.. Springer-Verlag Berlin Heidelberg New York. Also Astronomy and Astrophysics Library)

Rohlfs, K. & Wilson, T. L. 2004, Tools of Radio Astronomy (Springer)

Sault, B., Killeen, N. 2004, Miriad Users Guide

Savage, B. D. & de Boer, K. S. 1979, ApJ, 230, L77

Savage, B. D. & de Boer, K. S. 1981, ApJ, 243, 460

Savage, B. D. & Massa, D. 1987, ApJ, 314, 380

Savage, B. D. & Sembach, K. R. 1996, ARA&A, 34, 279

Savage, B. D., Wakker, B., Jannuzi, B. T., et al. 2000, ApJS, 129, 563

Savage, B. D., Wakker, B. P., Sembach, K. R., Richter, P., & Meade, M. 2005, in Astronomical Society of the Pacific Conference Series, Vol. 331, Extra-Planar Gas, ed. R. Braun, 3

Schmidt, M. 1963, Nature, 197, 1040

Sembach, K. R. & Danks, A. C. 1994, A&A, 289, 539

Sembach, K. R., Danks, A. C., & Savage, B. D. 1993, A&AS, 100, 107

Sembach, K. R. & Savage, B. D. 1996, ApJ, 457, 211

Sembach, K. R., Savage, B. D., & Massa, D. 1991, ApJ, 372, 81

Sembach, K. R., Tripp, T. M., Savage, B. D., & Richter, P. 2004, ApJS, 155, 351

Sembach, K. R., Wakker, B. P., Savage, B. D., et al. 2003, ApJS, 146, 165

Shapiro, P. R. & Field, G. B. 1976, ApJ, 205, 762

Spitzer, L. J. 1956, ApJ, 124, 20

Thilker, D. A., Braun, R., Walterbos, R. A. M., et al. 2004, ApJ, 601, L39

Thom, C., Putman, M. E., Gibson, B. K., et al. 2006, ApJ, 638, L97

Tripp, T. M., Wakker, B. P., Jenkins, E. B., et al. 2003, AJ, 125, 3122

Valageas, P., Schaeffer, R., & Silk, J. 2002, A&A, 388, 741

Vallerga, J. V., Vedder, P. W., Craig, N., & Welsh, B. Y. 1993, ApJ, 411, 729

van Woerden, H., Schwarz, U. J., Peletier, R. F., Wakker, B. P., & Kalberla, P. M. W.
    1999, Nature, 400, 138

Vladilo, G., Molaro, P., Monai, S., et al. 1993, A&A, 274, 37

Vogelaar, M. G. R. & Wakker, B. P. 1994, A&A, 291, 557

Wadsley, J. W. & Bond, J. R. 1997, in Astronomical Society of the Pacific Conference
    Series, Vol. 123, Computational Astrophysics; 12th Kingston Meeting on Theoretical
    Astrophysics, ed. D. A. Clarke & M. J. West, 332

Wakker, B. P. 1991, A&A, 250, 499

Wakker, B. P. 2001, ApJS, 136, 463

Wakker, B. P. 2004, in Astrophysics and Space Science Library, Vol. 312, High Velocity
    Clouds, ed. H. van Woerden, B. P. Wakker, U. J. Schwarz, & K. S. de Boer, 25

Wakker, B. P., Howk, J. C., Savage, B. D., et al. 1999, Nature, 402, 388

Wakker, B. P. & Mathis, J. S. 2000, ApJ, 544, L107

Wakker, B. P. & van Woerden, H. 1997, ARA&A, 35, 217

Wakker, B. P., York, D. G., Howk, J. C., et al. 2007, ApJ, 670, L113

Wakker, B. P., York, D. G., Wilhelm, R., et al. 2008, ApJ, 672, 298

Welsh, B. Y., Vedder, P. W., & Vallerga, J. V. 1990, ApJ, 358, 473

Westmeier, T. 2007, PhD thesis, Rheinische Friedrich-Wilhelms-Universität Bonn

Westmeier, T., Braun, R., Brüns, C., Kerp, J., & Thilker, D. A. 2007, New Astronomy
    Review, 51, 108

Westmeier, T., Brüns, C., & Kerp, J. 2005, A&A, 432, 937

Westmeier, T., Brüns, C., & Kerp, J. 2008, in Astronomical Society of the Pacific Confer-
    ence Series, Vol. 393, New Horizons in Astronomy, ed. A. Frebel, J. R. Maund, J. Shen,
    & M. H. Siegel, 283

Weymann, R. J., Carswell, R. F., & Smith, M. G. 1981, ARA&A, 19, 41

Winkel, B., Kerp, J., Kalberla, P. M. W., & Keller, R. 2008, in American Institute of Physics Conference Series, Vol. 1035, The Evolution of Galaxies Through the Neutral Hydrogen Window, ed. R. Minchin & E. Momjian, 259

Wolfire, M. G., McKee, C. F., Hollenbach, D., & Tielens, A. G. G. M. 1995, ApJ, 453, 673

Woodgate, B. E., Kimble, R. A., Bowers, C. W., et al. 1998, PASP, 110, 1183

Yoshizawa, A. M. & Noguchi, M. 2003, MNRAS, 339, 1135

Zhang, Y., Anninos, P., & Norman, M. L. 1995, ApJ, 453, L57

Epilogue

Writing a PhD thesis means to open the mind in many different directions. It is the first time one really works on an own project for three years and takes responsibility for the results. Beside reducing and analysing data, one has to write proposals, read papers to be up-to-date, give talks, learn and understand many different computer programs, visit countries all over the world to socialise with other scientists, and, last but not least, to be eventually able to contribute to the scientific progress.

In my project I had the luck that it was possible to do spectroscopy in two wavelength regimes, i.e., the radio and the ultraviolet. This enabled me to have an insight into many different aspects of astronomy. Nevertheless, one has to set limits and concentrate on a specific topic. In my case it was probing extraplanar low-column density gas around the Milky Way through quasar absorption and corresponding H$\,$I emission lines. This technique provides a bulk of information like the velocities of the gas from the Doppler shift, the chemical composition and the physical properties.

So many questions appeared and had to be discussed. What is the origin of the gas, how far it is away from the Milky Way, how does the gas influence the evolution of our home galaxy and what is its role in the cosmological context? I realised early that at every point in my work more questions arose than were answered and that a PhD thesis is a never-ending construction site. It was hard for me to admit the fact that one never gets definite answers in astronomy, just possible solutions. One should keep in mind that analysing an astronomical object regarding a certain aim with any kind of technique, means just to look at it from one specific point of view. A satisfying conclusion or interpretation requires the integration of many different astronomical directions. Therefore, an active communication between the multi-disciplinary fields is crucial.